

Three-Dimensional Microstructure
Characterization of Surface-Crystallized
Glass Ceramics

Von der Fakultät für Physik und Geowissenschaften

der Universität Leipzig

genehmigte

DISSERTATION

zur Erlangung des akademischen Grads

doctor rerum naturalium

Dr. rer. nat.,

vorgelegt

von M. Sc. Richard Busch

geboren am 18.09.1987 in Halle (Saale)

Gutachter: Prof. Dr. Marius Grundmann (Universität Leipzig)

Prof. Rik Drummond-Brydson (University of Leeds)

Tag der Verleihung: 23.10.2023

Bibliographische Beschreibung:

Busch, Richard

Three-Dimensional Microstructure Characterization of Surface-Crystallized Glass Ceramics

Universität Leipzig, Dissertation

119 S., 126 Lit., 47 Abb., 2 Tab.

Referat

Die dreidimensionale Mikrostruktur, welche bei der Oberflächenkristallisation von Glaskeramiken entsteht, wird mittels einer neuartigen Methode zur Präparation von abgesenkten Probenoberflächen untersucht. Diese *Initialkantensektionierungsmethode*, welche auf der Erzeugung von Scharten in der Probenoberfläche und anschließender Glanzwinkelionenstrahlerosion basiert, erlaubt das rapide Freilegen von großflächigen Schichten in wohldefinierten Tiefen unterhalb der ursprünglichen Probenoberfläche. In dieser Dissertation werden mehrere Variationen der Technik durch Kombination von Laserablation, Ionenbreit- sowie Ionenfeinstrahlerosion untersucht und miteinander verglichen. Die in Bezug auf Schnittgeometrie und Probengüte relevanten, experimentellen Parameter werden bestimmt und bewertet. Ein Modell zur Beschreibung der zeitlichen Evolution der Probengeometrie während des Erosionsvorgangs wird auf Grundlage von Simulationen und analytischen Näherungen aufgestellt und mit experimentellen Ergebnissen verglichen. Schließlich wird die Initialkantensektionierungsmethode mit Elektronenrückstreubeugung kombiniert um Wachstumseffekte bei der Oberflächenkristallisation von Diopsid- und $\text{Ba}_2\text{TiSi}_2\text{O}_8$ -Fresnoitglaskeramiken zu untersuchen.

Abstract

Three-dimensional microstructures resulting from surface crystallization of glass ceramics are studied using a novel sample sectioning method. Based on the creation of notches on the sample surface and subsequent glancing-angle ion beam erosion, *initial notch sectioning* enables the rapid excavation of large subsurface layers at well-defined depths. In this thesis, several variations of this technique using different combinations of laser ablation, broad and focused ion beam erosion are realized and compared to each other. Relevant parameters controlling the section geometry and quality are determined. A model of the surface evolution kinetics is developed using simulations and analytical estimates, which is compared to experimental results. Finally, initial notch sectioning in combination with electron backscatter diffraction is applied to elucidate growth phenomena in the surface crystallization of diopside and $\text{Ba}_2\text{TiSi}_2\text{O}_8$ fresnoite glass ceramics.

Contents

1	Introduction	1
1.1	Motivation	1
1.2	Aims and Objectives	3
2	Literature Review	5
2.1	Sample Preparation for Electron Backscatter Diffraction Studies	5
2.2	Serial Sectioning Methods	8
2.3	Microstructure Characterization of Glass Ceramics using EBSD	11
2.4	Interim Conclusion	13
3	Theory	15
3.1	Erosion of a Surface Under Ion Bombardment	15
3.1.1	Sputtering	15
3.1.2	Kinetic Theory of Surface Evolution	18
3.1.3	Numerical Simulation of Surface Erosion	20
3.1.4	Erosion of a Surface With Initial Notches	21
3.2	Electron Backscatter Diffraction	23
3.2.1	Measurement Principle	23
3.2.2	Representation of Orientations and Texture	25
4	Methods and Materials	29
4.1	Sample Preparation and Processing	29
4.2	Surface Metrology	30
4.3	Microstructure Analysis	32
4.4	Materials	32

Contents

5	Erosion of Surfaces With Initial Notches	35
5.1	Evaluation of Surface Processing Methods	35
5.1.1	Notch Creation	36
5.1.2	Terrace Formation by Glancing-Angle Ion Beam Erosion	38
5.2	Surface Properties in the Terrace Region	40
5.2.1	Terrace Roughness	40
5.2.2	Ion Beam Induced Amorphization	44
5.3	Evolution of Surface Geometry	47
5.3.1	Linear Model	47
5.3.2	Simulations	49
5.3.3	Experimental Results	51
5.4	Discussion	53
5.4.1	Sample Processing	53
5.4.2	Sample Quality	56
5.4.3	Kinetic Model of Surface Evolution	62
6	Depth-Resolved Microstructure Characterization Using Initial Notches	65
6.1	Diopside	65
6.2	Ba ₂ TiSi ₂ O ₈ fresnoite (BTS)	72
6.3	Discussion	82
6.3.1	Methodological Aspects of Initial Notch Sectioning	82
6.3.2	Microstructure Analysis on Surface-Crystallized Glass Ceramics . .	85
7	Summary and Outlook	91
	Bibliography	94
	Acknowledgements	107

List of Figures

1.1	Erosion of a surface with an initial notch - schematic.	3
2.1	Serial sectioning techniques.	10
2.2	Textured glass ceramics	12
3.1	Sputtering yield - energy and angle dependence	16
3.2	Geometric model used for surface erosion simulations.	20
3.3	Quantities describing a notched surface after erosion	22
3.4	Setup of an EBSD measurement	23
3.5	Euler angles	26
3.6	Construction of a pole figure	27
5.1	Creation of initial notches using PFIB	37
5.2	Creation of initial notches using fs-laser ablation	37
5.3	Terrace formation by glancing angle BIB and PFIB erosion	39
5.4	Glancing-angle FIB erosion of glass	39
5.5	Sketch of different surface groove patterns	40
5.6	Notched surface with grooves before and after terrace formation	41
5.7	SEM micrograph of terrace unaffected by grooves	42
5.8	SEM micrograph of terrace affected by grooves on the initial surface	43
5.9	SEM micrograph of terrace affected by grooves on the notch	44
5.10	Preparation of TEM lamella with FIB	45
5.11	TEM micrograph of the edge	45
5.12	High resolution TEM micrographs along the terrace	46
5.13	Model of two intersecting surface segments under ion beam erosion	48
5.14	Terrace growth speed as function of surface inclination angle θ_{inc}	49
5.15	Terrace growth speed, aspect ratio and induction depth - simulation	50
5.16	Erosion depth data - experiment	52

5.17	Aspect ratio and induction depth - experiment	52
5.18	Usage of glancing angle FIB erosion for TEM preparation	55
5.19	Geometry of mask projection model	57
5.20	Mask projection of a surface ripple	58
5.21	Scattering of ions at edges	60
5.22	Amorphization layer thickness	61
6.1	Surface crystallization in diopside: annealing conditions	66
6.2	SEM micrographs of notched diopside surface	67
6.3	Topography and inverse pole figure maps of sectioned diopside sample	68
6.4	Crystallographic texture of sectioned diopside sample	69
6.5	Depth-dependent IPF data of several diopside crystals	69
6.6	SEM micrograph of sectioned diopside crystal	70
6.7	Grain boundary misorientations of sectioned diopside crystals	71
6.8	Growth of fresnoite in different ambient conditions	73
6.9	Initial surface of fresnoite sample	73
6.10	EBSD data of the pristine fresnoite surface	74
6.11	Initial notch sectioning of a fresnoite sample	75
6.12	Micrographs of BTS crystal beneath the pristine surface	77
6.13	EBSD data acquisition strategies	78
6.14	EBSD measurement of fresnoite after initial notch sectioning	79
6.15	Micrographs of spherical fresnoite crystals	81
6.16	Advanced initial notch sectioning approaches - schematic	83

List of Tables

5.1	Combinations of processing methods and materials analyzed in this work.	36
5.2	Amorphization layer thickness and local inclination	46

Acronyms and Symbols

Acronyms

BIB broad ion beam

BTS $\text{Ba}_2\text{TiSi}_2\text{O}_8$ fresnoite

EBS electron backscatter diffraction

EBSP electron backscatter patterns

EDXS energy dispersive x-ray spectroscopy

FIB focused ion beam

GCIB gas cluster ion beam

HIM helium ion microscopy

LIPSS laser-induced periodic surface structures

MRD multiples of random distribution

ODF orientation distribution function

PFIB plasma focused ion beam

ROI region of interest

SEM scanning electron microscopy

STEM scanning transmission electron microscopy

Symbols

TEM transmission electron microscopy

WLI white light interferometry

XRD X-ray diffraction

Symbols

$SO(3)$ group of proper rotations in three dimensions

AR aspect ratio of terrace length to mean erosion depth

CI confidence index

IQ image quality

PSD power spectral density function

Y sputtering yield

θ_{ion} ion incidence angle relative to the surface plane

d_0 mean erosion depth of the surface, excluding the terrace region

d_{ind} induction depth, i.e. the mean erosion depth during initial terrace formation

w_{N} notch width

1 Introduction

1.1 Motivation

Glass ceramics are a remarkable class of materials that can be tailored to exhibit unique combinations of properties. They are obtained by controlled crystallization of a glass and are composed of a mixture of glassy and one or several crystalline phases (Deubener *et al.*, 2018). Today, glass ceramics are present in almost every household in the form of oven stoves and cookware, but also in high-tech applications such as telescope mirrors and mask blanks for lithography, dental materials, hard disc substrates and more (Zanotto, 2010; Davis & Zanotto, 2017). A key prerequisite for designing high-performance glass ceramics is a deep understanding and control of the microstructure formed during the crystallization process.

Today, technical glass-ceramic products are most commonly produced via heterogeneous volume nucleation, that is by addition and dispersion of additives (nucleation agents) in the glass which enable the formation of nuclei. This mode was already crucial in the accidental discovery of this new type of material by Stookey in 1959 (Stookey, 1959). In contrast, surface nucleation, although being the kinetically dominant mode in many cases, is utilized less widely due to the considerable difficulties in controlling the conditions at the surface in a reproducible way (Höland *et al.*, 2003). In recent decades however, surface nucleation and surface-induced microstructure formation have gained increased attention, following coordinated research efforts initiated by the Technical Committee TC-7 of the International Commission on Glass in 1990 (Müller *et al.*, 2000). While the main emphasis of this effort was first on the kinetics of surface nucleation and the role of surface defects and active sites, the microstructure obtained as a result of surface crystallization has become a major focus particularly in the last decade. One major finding was that surface nucleation can lead to the formation of preferentially oriented crystals at the surface of many glass systems, for example diopside (Wisniewski *et al.*, 2012) or $\text{Sr}_2\text{TiSi}_2\text{O}_8$ (STS) and $\text{Ba}_2\text{TiSi}_2\text{O}_8$ (BTS) fresnoite (Wisniewski *et al.*,

1 Introduction

2018c, 2018b). By contrast, no texture formation was found on cordierite glass ceramics (Wisniewski *et al.*, 2011b). Considerable progress has been made since, but the understanding of surface crystallization is still incomplete owing to the complexity of the issue and the large parameter space involved. Theoretical models linking the observed crystallization behaviour to the crystal structure are only starting to emerge at the time of writing (Wisniewski & Rüssel, 2021; Tielemann *et al.*, 2022).

The recent progress made in the study of surface crystallization can be attributed to a significant extent to the application of highly-resolved, surface-sensitive orientation measurement techniques, in particular electron backscatter diffraction (EBSD) in the scanning electron microscopy (SEM). The application of EBSD to glass ceramic materials can be a demanding endeavour. Challenges can be posed by sample charging, limited stability of some materials to the electron beam (causing degradation of the electron backscatter patterns (EBSP), Wisniewski *et al.* (2011a)), the potential presence of both residual glass *and* crystalline phase within the diffraction volume (Wisniewski & Rüssel, 2016), or strain in the lattice due to stresses caused by a misfit of thermal expansion coefficient between glass and crystal phase. Nevertheless, deep insights have been obtained by surface analysis of glass ceramics with EBSD.

A key limitation in literature so far has been the lack of three-dimensional data. All data available have been generated either on the immediate surface itself or on some mechanically prepared cross section. In contrast, three-dimensional (analytical) measurements using serial-sectioning focused ion beam (FIB) tomography have become firmly established in other disciplines such as metallography (Konrad *et al.*, 2006) or mineralogy (Dillon & Rohrer, 2008). This gap can be explained by the considerable effort involved in serial sectioning tomography and the limited volume accessible on top of the already mentioned general difficulties encountered in microstructure analysis of glass ceramics using EBSD. At the same time, having access to the microstructure of glass ceramics in a depth-resolved way would provide deeper insights into phenomena such surface-near crystallization and the formation of a glassy skin (Avramov & Voelksch, 2002) or orientation selection effects upon growth into the bulk. Hence, there is a serious demand for alternatives to FIB serial sectioning tomography which provide depth-resolved data in a reliable way which is more suitable to the study of glass ceramic materials.

In this context, the application of so called initial notches (Busch *et al.*, 2018) could provide a novel and advantageous approach to sample preparation for depth-resolved

1 Introduction

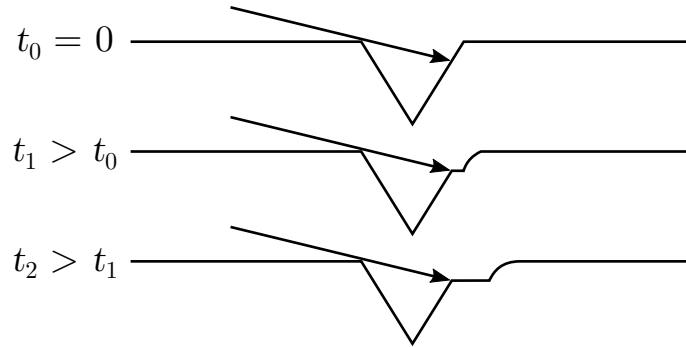


Figure 1.1: Sketch of the erosion of a surface with initial notches. A cross section of the surface through the notch for three different erosion durations is shown.

electron backscatter studies. The concept is based on the observation that increased erosion rates occur at inclined surface features during established broad ion beam milling procedures (Barna, 1991). By creating notches on a surface adjacent to the region of interest and then exposing the sample to a broad ion beam at grazing incidence, formation of terraces can be facilitated at a well-defined depth (c.f. Fig. 1.1). The premise of this work is to exploit the formation of these locally receded terraces for a broad ion beam, quasi-serial sectioning approach to depth-resolved EBSD studies of surface crystallized glass ceramics. Utilizing this method of *initial notch sectioning*, depth-resolved EBSD measurements of surface crystallized glass ceramics are performed for the first time and in a way which is both highly efficient and suitable for larger areas than could be reasonably accessed by a FIB serial sectioning approach.

1.2 Aims and Objectives

This work builds upon previous research accomplished in Busch *et al.* (2018), where erosion of a surface with initial notches was first studied on silicon and applied to the preparation of electron transparent lamella for transmission electron microscopy (TEM). For this thesis, the following aims and extensions of the method were pursued:

- Initial notch sectioning is implemented using different combinations of material processing methods: fs-pulsed laser ablation and focused ion beam milling for the creation of notches, and glancing-angle focused or broad ion beam milling for terrace formation. The methods are compared and their applicability for initial

1 Introduction

notch sectioning evaluated on selected model material systems.

- Surface erosion using initial notches is adapted to insulating glasses and glass ceramic materials. The influence of sample charging on the ion beam milling processes is investigated.
- The sample quality achievable using initial notch sectioning is analyzed, in particular with respect to surface roughness and ion beam induced damage in the terrace region. Experimental conditions leading to the preparation of high quality samples are derived.
- Models for the terrace growth kinetics and the sample geometry obtained by initial notch erosion are established, which are required in order to enable sufficient practical control over erosion depth and region-of-interest size.
- The applicability of initial notches to sample sectioning and depth-resolved EBSD is demonstrated on surface-crystallized glass ceramics. For this purpose, studies are performed on two selected model systems: a stoichiometric diopside glass ceramic and near-stoichiometric $\text{Ba}_2\text{TiSi}_2\text{O}_8$ (BTS) fresnoite glass ceramic. Both basic and advanced sample designs using initial notches are demonstrated.

As a result, a novel, high-performance sample preparation technique for depth-resolved microstructure analysis of surface-crystallized glass ceramics and beyond is established.

2 Literature Review

In this chapter, the literature relevant to depth-resolved electron backscatter diffraction analysis of surface crystallized glass ceramics is surveyed. First, requirements for EBSD samples and available preparation methods are reviewed. Next, serial-sectioning approaches for three-dimensional microstructure characterization are discussed. Finally, the available literature concerning microstructure characterization of glass ceramics using EBSD is critically scrutinized.

2.1 Sample Preparation for Electron Backscatter Diffraction Studies

High-quality samples are a key prerequisite for successful microstructure analysis with EBSD. Since electron backscatter patterns are dominated by electrons originating from a thin layer 50 nm to 100 nm¹ thick, it is crucial to avoid any introduction of superficial damage and surface amorphization during sample preparation. Similarly, any alterations to the strain state of the crystals should be avoided (Voort, 2011a). The surface also needs to be sufficiently flat to avoid topography-related artefacts such as shadowing of the EBSD detector. In the case of insulating samples, additional care must be taken in order to avoid sample charging. Deposition of a thin carbon film was used in all experiments on glasses and glass ceramics for this dissertation, which provided satisfactory results. For an extensive discussion of coating techniques and further potential coating materials such as Pt or Ir, see Echlin (2011). Alternative approaches include the use of low-vacuum conditions (El-Dasher & Torres, 2009) or the application of ionic liquids to the surface (Brodusch *et al.*, 2014). The following survey will summarize available methods for the preparation of flat and defect-free surfaces suitable for EBSD analysis. Application to serial section tomography are discussed in the next section.

¹See Wisniewski and Rüssel (2016) and Wisniewski *et al.* (2017) for a discussion of different concepts of information depth of EBSD.

2 Literature Review

Mechanical preparation techniques are most widely used for sample preparation, in particular in metallography and mineralogy. Tutorial discussions are given in Katrakova and Mücklich (2001) and Voort (2011a), among others. A typical preparation process starts by extracting a suitably sized sample from a larger bulk material by sawing. Use of precision sawing is recommended by (Voort, 2011a) in order to limit the damage introduced to the material. Then, grinding with successively smaller abrasive grain sizes is performed, for example with SiC paper. Remaining superficial damage is reduced during subsequent polishing steps using, e.g., diamond polishing slurries. Final polishing steps often make use of colloidal silica or alumina suspensions. Optionally, a final wet etching or ion beam etching step is sometimes applied. The proper selection of grinding and polishing steps, abrasives, polishing cloths and suspensions and possible etchants depends on the material under investigation. Preparation 'recipes' for commonly studied materials are available (Voort, 2011a, 2011b).

Ultramicrotomy is a possible alternative to grinding and polishing. While the technique is most commonly applied to soft materials, such as biological samples in the life sciences or for polymer materials, successful preparation of Al alloy surfaces suitable for EBSD analysis was demonstrated (Sandu *et al.*, 2010; Hashimoto *et al.*, 2016). The control of preparation artefacts such as knife marks, compression, and plastic deformation is reported as a major challenge, nonetheless. For a commercial Al alloy, Hashimoto *et al.* (2016) estimates a deformation depth of 60 nm using a diamond knife and a process without knife oscillation. This size is on the order of the information depth of the technique and leads to significant loss data quality. Using a cutting process with oscillating blade, sample quality was shown to be improved and indexing rates (see Section 3.2.1) between 83 % and 92 % were obtained.

Ion beam sputter erosion with broad or focused ion beams is also widely used for EBSD sample preparation. Common applications of broad ion beam erosion include the preparation of cross section samples using a shielding plate (also called ion beam slope cutting, Hübner and Hauffe (1995) and Takahashi *et al.* (2006)) or the removal of damaged material layers caused by preceding preparation steps. In particular, broad ion beam erosion with noble gas ions at glancing incidence is very well suited to produce surfaces with minimal damage or roughening. A number of studies performed in the context of TEM sample preparation investigated ion beam induced surface amorphization and roughening (Schuhrke *et al.*, 1992; Barna *et al.*, 1999; McCaffrey *et al.*, 2001). It was

2 Literature Review

shown that by using low acceleration voltages of only a few hundred volt, amorphization layer thickness can be reduced to the single digit nm range on materials such as GaAs or Si (Barna *et al.*, 1998). These properties make glancing-angle broad ion beam polishing also highly effective for EBSD sample preparation (Nogita & Dahle, 2001). Focused ion beam milling on the other hand is commonly used for targeted preparation of particular sample features. With respect to sample quality, low voltage performance of FIB devices has long been a limiting factor for creating surfaces with minimal amorphization. Implantation of ions is a further error source, in particular when using Ga^+ ion beams. Finally, curtaining effects can lead to surface roughening and reduce pattern quality. However, newer generations of focused ion beam instruments have made polishing conditions sufficient for EBSD analysis (Matteson *et al.*, 2002) and dual beam FIB-SEM instruments equipped with EBSD systems have become firmly established research tools in material science.

Application of **ultra-short pulsed laser ablation** to sample preparation has gathered increased interest in the past decade. Rapid creation of non-trivially shaped samples is possible with removal rates exceeding those of focused ion beam devices by several orders of magnitude (Höche *et al.*, 2015). EBSD data collection directly on laser-machined Ni-alloy surfaces was demonstrated by Echlin *et al.* (2012), with some limitations due to roughening upon continued milling from the initial surface. As an extension, combination of laser ablation with glancing-angle plasma focused ion beam (PFIB) polishing is reported in Echlin *et al.* (2021), allowing preparation of a wider range of materials.

Other techniques are available which are more specialized and limited to certain material systems or have not yet found widespread use. Electropolishing is capable of creating high quality surfaces but is limited to metals and alloys. Additionally, surface roughening can occur if phases with significant differences in removal rates are present (Nogita & Dahle, 2001; Wynick & Boehlert, 2005). Material removal based on atomic force microscopy (AFM) nanomilling was used by Kutes *et al.* (2017) to create planarized surface sections of CdTe thin film solar cells which are suitable for EBSD analysis. While this approach allows for very high spatial resolution and surface flatness as well as combination with probing microscopy modalities, it faces severe restrictions in terms of accessible surface size and preparation speed. In contrast, extremely rapid sample preparation was reported by Brackmann *et al.* (2014) using a glow discharge plasma for material removal, at the cost of requiring sputtering parameter optimization for each individual sample type. The possibility of applying helium ion microscopy (HIM) to

2 Literature Review

EBSD sample preparation has been raised (Wolff, 2021) as a way to remove damage introduced during Ga FIB polishing.

2.2 Serial Sectioning Methods

Computational advances over the past two decades have made processing and analysis of large three-dimensional datasets possible and gave rise to a wide range of three-dimensional microscopy and tomography techniques². Extensive literature using a range of different imaging modalities and signal types is available, among those tomography techniques based on X-ray microscopy (Kaulich *et al.*, 2011), scanning electron microscopy and transmission electron microscopy (Möbus & Inkson, 2007). Of particular relevance for this thesis are SEM-based tomography methods, where 3D microstructures have been reconstructed from data as diverse as backscattered electron micrographs to energy dispersive x-ray spectroscopy (EDXS) spectra (Kotula *et al.*, 2006) and EBSD data (Groeber *et al.*, 2006). The typical approach to obtain a series of views for 3D reconstruction in SEM-based tomography is described as serial sectioning: a surface suitable for the desired imaging mode is prepared and data are recorded. Then, a layer of material with defined thickness is removed and a subsequent measurement is performed, and so on. An overview of preparation techniques used to facilitate serial sectioning is given hereafter. For a more focused review on techniques specifically suitable for in-situ serial-sectioning experiments in the SEM, a recent review by Echlin *et al.* (2020) is available.

Mechanical serial section methods include grinding and polishing, cutting and ultramicrotomy. Both manual and automatic procedures have been developed. The usage of grinding for generating serial sections in fact predates the availability of digital data reconstruction (Rhines *et al.*, 1976). Serial sectioning using digital reconstruction became established in the late 1990s. For example, polishing of a sample with a 0.06 μm silica slurry was used by (Kral & Spanos, 1999) to create serial sections of a hypereutectoid steel with 0.17 μm spacing in z-direction. Alkemper and Voorhees (2001) reported an automated sectioning device based on cutting with a diamond blade, capable of reproducible creating spacing between 1 μm to 20 μm . Light microscopy was mostly used

²Here, the term tomography is meant to encompass all measurement methods which employ reconstruction of a three-dimensional volume from a series of two-dimensional measurements or views, in contrast to narrower definitions additionally requiring these views to be obtained by projection (c.f. Möbus and Inkson (2007)).

2 Literature Review

then, since in-situ mechanical preparation in an SEM was not yet available. In contrast, grinding and subsequent lapping with an Al_2O_3 slurry was used by Wall *et al.* (2001) in an early 3D EBSD study to create serial section data of a polycrystalline Ta sample with a spacing of $4.8\ \mu\text{m}$. Notably, the lapping time alone for each section was reported to be three hours, highlighting the considerable experimental effort involved in this approach. Ultramicrotomy provides a more efficient alternative, which is also applicable to in-situ setups. Slice spacing of some tens nm can be readily prepared (Zankel *et al.*, 2009; Hashimoto *et al.*, 2010). Even smaller spacings down to the single digit nm range are achievable. However, friction forces and damage to the sample increase in that regime due to the finite knife thickness (Hashimoto *et al.*, 2016). Restrictions also apply with respect to sample hardness as sample damage and artefacts such as knife marks increase for harder materials.

The introduction of FIB serial sectioning techniques in the 1990s contributed significantly in popularizing SEM based tomography. Reviews can be found for example in Möbus and Inkson (2007), Holzer and Cantoni (2012), and Bassim *et al.* (2014). FIB serial sectioning experiments have been performed both in single beam and dual-beam instruments and can be differentiated by the milling geometry employed. For example, serial sectioning can be performed by milling at (near) normal incidence, with milling depth being controlled via ion beam dwell time (Dunn & Hull, 1999). This approach is commonly used for secondary ion mass spectroscopy depth-profiling. A variation of this "top-down" approach using a gas cluster ion beam (GCIB) for sputter erosion has been recently demonstrated as a serial sectioning method suitable for large volumes of biological samples (Hayworth *et al.*, 2020). In order to avoid preferential erosion and surface roughening in inhomogeneous materials, milling parallel to the surface was found advantageous in most cases and is generally performed in dedicated dual-beam instruments (Sakamoto *et al.*, 1998). Using Ga^+ liquid metal ion sources, excellent spatial and depth resolution can be realized. However, sample regions are limited to some ten μm linear dimensions. Focused ion beam devices using an inductively coupled plasma ion source (plasma FIB or PFIB) are an alternative, providing higher ion currents at some loss of resolution (Smith *et al.*, 2006). Preparation speed gains of $\times 60$ are claimed by Burnett *et al.* (2016), translating into larger accessible volumes up to some $100\ \mu\text{m}$ linear dimensions. Reduced ion implantation and surface amorphization are further reported advantages of using Xe^+ over Ga^+ as projectile species.

Noble gas broad ion beam erosion for serial sectioning has been proposed by Winiarski

2 Literature Review

et al. (2017) as an option for even larger areas up to mm linear dimensions. The ion milling step is performed ex-situ, requiring transfer of the sample to the ion milling device. A coupled BIB-SEM where the ion milling work station is connected to the SEM via an interlock and sample transfer is facilitated via a robotic arm was recently reported by Hosman *et al.* (2016) and Gholinia *et al.* (2020). Besides higher milling rates compared with FIB serial sectioning methods, the method is capable of preparing surfaces with very low damage. Due to the profile of the ion beam, some surface cupping can occur over larger length scales, leading to non-parallel sectioning, which might be needed to correct for.

Laser machining in novel tri-beam (Laser, PFIB and SEM) devices is another recent alternative (Echlin *et al.*, 2021). Removal rates about two orders of magnitude higher than Xe^+ plasma FIB are achievable, at the cost of reduced milling resolution. Useable slice thickness on the order of one micron are reported. While surface quality is sufficient on some materials for further analysis, an ion beam polishing step is generally needed. Care has to be taken when selecting the milling parameters in order to avoid surface roughening via formation of laser-induced periodic surface structures (LIPSS) (Huang *et al.*, 2009). An overview of the different sectioning methods and the corresponding volume sizes accessible is shown in Fig. 2.1.

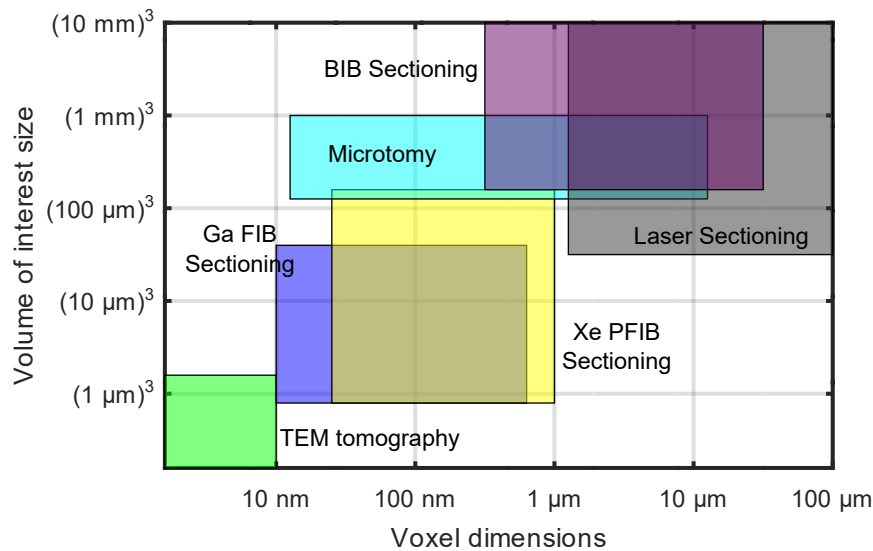


Figure 2.1: Overview of serial sectioning techniques (after Holzer and Cantoni (2012) and Burnett *et al.* (2016)).

2.3 Microstructure Characterization of Glass Ceramics using EBSD

Adoption of EBSD to the study of glass ceramics was lagging behind other disciplines. While automated EBSD systems were introduced in the early 1990s (Wright & Adams, 1992), the first application to a glass ceramic was reported in 2004 (Völksch *et al.*, 2004). A pronounced upswing in popularity was related to growing interest in textured glass ceramics and surface crystallized glass ceramics. In particular following the discovery of oriented top surface layers on surface crystallized fresnoite glass glass ceramics (Wisniewski *et al.*, 2010), a number of studies were conducted on glasses ceramics spanning all seven crystal systems. A comprehensive review of surface crystallization studies using EBSD for microstructure analysis has been compiled by Wisniewski and Rüssel (2021). Crucially, using EBSD, preferential crystal orientation at the surface can be demonstrated on samples where detection of such a texture with common alternatives such as X-ray diffraction (XRD) and texture goniometry fails due to subsurface orientation changes. In this case, the increased surface sensitivity of EBSD is a key advantage (< 100 nm for EBSD compared to some $10\ \mu\text{m}$ to $100\ \mu\text{m}$ for XRD, Wisniewski *et al.* (2018a)).

Textured glass ceramics can be the result of growth selection effects, can occur during crystallization in external fields (Höche *et al.*, 1999), or be stress-induced (Wisniewski *et al.*, 2013a). EBSD studies on surface crystallized glass ceramics revealed that preferential orientation can also be the result of oriented surface or surface-near nucleation (Wisniewski *et al.*, 2012, 2016; Tielemann *et al.*, 2021). According to Wisniewski and Rüssel (2021), oriented surface nucleation most commonly leads to textures where a single, low-index crystal plane shows a defined relation to the sample surface, although more complicated textures with up to three texture components or preferential orientation of higher-index planes have been reported. In diopside for example, both textures with a single component and textures with two components have been found (Wisniewski *et al.*, 2012; Otto *et al.*, 2013; Tielemann *et al.*, 2021). In contrast, no evidence of non-random surface textures has been found in systems such as cordierite, suggesting absence of oriented nucleation. Examples are shown in Fig. 2.2. Experimental parameters governing the orientation preference have been shown to include annealing temperature (Wisniewski *et al.*, 2013b) and network former content of the glass (Wisniewski *et al.*, 2018c, 2018b). Upon growth into the bulk, preferential orientation is typically lost over

2 Literature Review

length scales of 10 μm to 100 μm due to growth selection for most glass ceramic systems studied so far (Wisniewski & Rüssel, 2021).

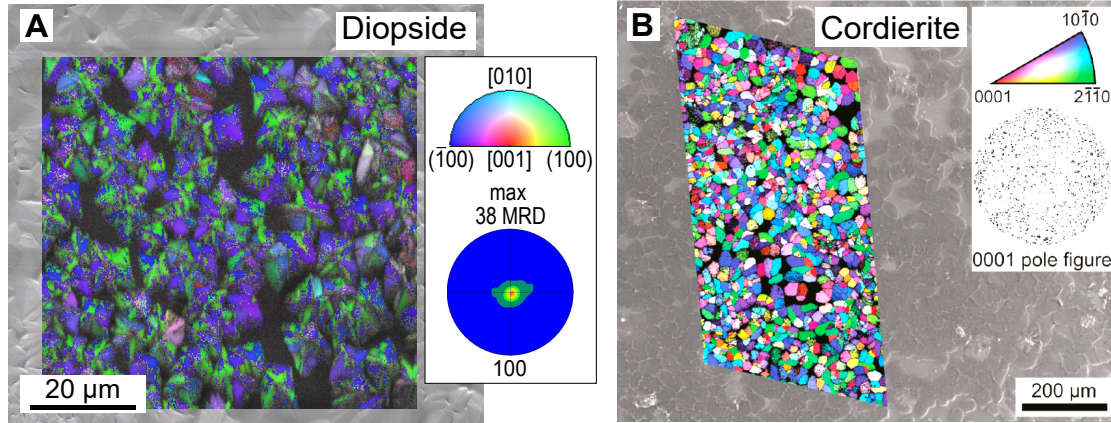


Figure 2.2: (A) Surface crystallized glass ceramics can exhibit a pronounced orientation preference in the normal direction of the surface, which is for example observed in Diopside glass ceramics (texture strength is given in multiples of random distribution, MRD). (B) In contrast, no orientation preference is observed in cordierite glass ceramic. Figures adapted from Tielemann *et al.* (2021) and Wisniewski *et al.* (2011b), respectively.

Some peculiarities apply to the EBSD study of glass ceramics. The necessity of coating the sample to prevent sample charging is reported in most studies. Incomplete crystallization can lead to microstructures with remaining residual glass. Suppression of residual glass in EBSD data is necessary for visualizing and analysis (Wisniewski *et al.*, 2010). However, if residual glass is formed in nano-inclusions (e.g. as reported in (Höche *et al.*, 1999)), pattern formation might be severely hindered or suppressed. In some systems, the thermal load introduced by the high-current electron beam used for EBSD measurements can cause damage to the surface and degradation of EBSP (Wisniewski *et al.*, 2011a). The occurrence of a glassy skin atop surface crystals has been reported in some systems such as cordierite (Avramov & Voelksch, 2002). A method for detection of such a glassy skin was proposed by Wisniewski *et al.* (2011a) based on the intentional, beam-induced degradation of EBSP during collection of EBSD data of the untreated surface and a polished reference surface.

A fundamental deficit in current literature is the lack of three-dimensional EBSD data acquisition approaches applied to glass ceramics. Measurements are generally performed on polished plane-view samples, polished cross sections, or on the untreated (except

2 Literature Review

for carbon coating) surface. More generally, no reports featuring serial sectioning of glass ceramics were found. Reports on tomography methods applied to glass ceramics are available only for X-ray computed tomography (XCT, Hojamberdiev *et al.* (2009)) and for X-ray microscopy (XRM, (Thieme, 2022)). Also, electron tomography in the TEM was used by Xu *et al.* (2008) to investigate precipitation of nano-dendrites in glass. Noteworthy, even when widening the focus to include non-crystallized glasses, serial sectioning is rarely reported, mostly in the context of FIB-SEM tomography of cracks and indents on glass surfaces (Cuadrado *et al.*, 2015; Elfallagh & Inkson, 2009) and investigation of particle-containing glass fibres (Cabié *et al.*, 2021), as well as radiotracer serial section experiments for determination of ion mobility (Schoo *et al.*, 2000).

2.4 Interim Conclusion

A wide range of sample preparation methods for high-quality (i.e. smooth and damage-free) surfaces suitable for EBSD studies is available. The most widely applicable methods are mechanical polishing and ion beam polishing, in particular glancing-angle, low-voltage broad ion beam erosion. Other methods are either limited to certain materials or do not always achieve the highest sample quality. Considering methods for serial sectioning experiments, the technique of choice is mainly determined by the size of the volume-of-interest, as depicted in Fig. 2.1. Mechanical polishing is applicable even to largest volumes, but hasn't found widespread adoption due to the exceedingly high effort involved and the incompatibility with automated in-situ experiments. For this reason, FIB-SEM serial sectioning is the most common serial sectioning method, providing flexibility, highest resolution, sample quality sufficient for microstructure investigation, integration of analytic instrumentation and automation - at the cost of a severely limited accessible sample volumes. BIB serial sectioning and fs-laser serial sectioning, combined with PFIB polishing in a tri-beam device, are emerging technologies with promising properties. They both significantly extend the accessible volume, but each comes with its own drawbacks. While BIB serial sectioning allows for the largest sample of all ion milling-based serial sectioning techniques, it does not allow for site specific preparation. In contrast, laser serial sectioning provides the most rapid and site-specific preparation method, but also requires the most complex experimental setup. Furthermore, it remains to be demonstrated that sufficiently smooth samples can be prepared and thermal effects are sufficiently small for transparent samples with low thermal conductivity. As such, glass ceramics with a

2 *Literature Review*

high fraction of residual glass could prove particularly challenging. Finally, a review of the available literature containing EBSD studies of glass ceramics reveals a lack of three-dimensional measurement approaches. Considering the intricacies of oriented nucleation and reorientation due to crystal growth reported for surface-crystallized glass ceramics, efficient access to the three-dimensional microstructure would certainly be appreciated. In this context, efficient sample preparation based on initial notches can help to get deeper insights into the laws governing surface-induced microstructure formation.

3 Theory

In this chapter, fundamental aspects relevant to sample preparation by sputter erosion and to surface analysis using electron backscatter diffraction are presented. The first section is dedicated to the erosion of a surface under ion beam bombardment. For this purpose, a discussion of sputtering is given, followed by an outline of the theory of surface evolution resulting from ion bombardment. Next, the simulation approach used in this thesis is introduced. Finally, selected aspects concerning the erosion of a notched surface are discussed, which were established in preceding work and will be expanded upon in this thesis. The second section gives a brief introduction to orientation measurements with electron backscatter diffraction as well as to representations of orientations and textures.

3.1 Erosion of a Surface Under Ion Bombardment

3.1.1 Sputtering

When the surface of a specimen is bombarded with energetic ions, ejection of secondary ions or clusters from the target can occur. This phenomenon is denoted as sputtering and does lead to the erosion of the surface. In order for particle ejection to occur, energy transfer to the target is necessary, which can take place in two different ways: energy transfer to the electrons (electronic energy loss) and energy transfer to the atoms (nuclear energy loss). The corresponding cross-section of each process is energy dependent. At low incident ion energies up to the 10 keV range, nuclear energy loss is the dominant process, whereas electronic energy loss becomes more relevant at ion energies in the range of 0.1 MeV to 1 MeV (Smentkowski, 2000).

Different sputtering regimes can be differentiated by the number of secondary species involved in the process. At lowest energies, only target atoms which received energy in a direct scattering event with the incident ion contribute to the sputtering process (single

3 Theory

knock-on collisions). On the other hand, if these primary knock-on atoms undergo further scattering events with target atoms (higher order scattering events), collision cascades are formed. These collision cascades can be further classified into linear collision cascades and non-linear collision cascades or spikes, depending on whether only a small number of atoms or most atoms within a given volume are involved in the cascade (Sigmund, 1987). Linear collision cascades provide a good model for sputtering in typical ion beam erosion applications with broad or focused ion beams. Theoretical work on linear collision cascades has made extensive use of Boltzmann transport theory (Sigmund, 2012).

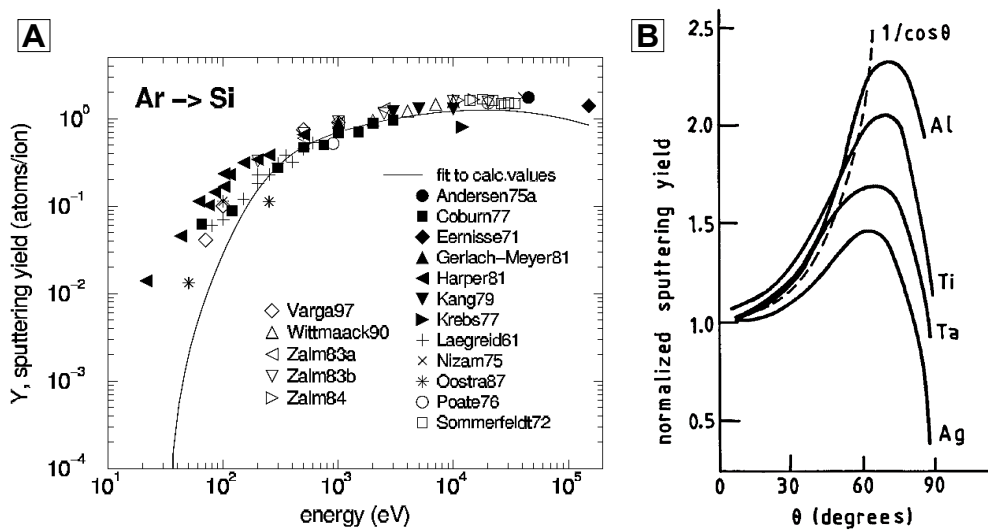


Figure 3.1: Energy dependence of the sputtering yield for Ar^+ ions on Si target (A) and angle dependence of the sputtering yield for Ar^+ ions on several elemental targets (B). Graphs are taken from Eckstein (2007) (left) and Carter (2001) (right).

The magnitude of sputtering is characterized by the sputtering yield Y , defined as the amount of ejected atoms and clusters per incident ion. The sputtering yield depends on both projectile species and target composition. Furthermore, for any given target and projectile, the sputtering yield is sensitive to projectile energy, incidence angle, and target topography. In Fig. 3.1, literature data for the yield dependence on ion energy and incidence angle for sputtering with Ar^+ ions are depicted. The following paragraphs illuminate different aspects of these functional dependences.

The energy dependence of the sputtering yield shows a maximum at intermediate energies of some 10 keV to 100 keV. Below a certain threshold energy of the incident

3 Theory

particle, no sputtering occurs and the sputtering yield vanishes. The sputtering threshold is related to the surface binding energy of the target species. A minimum estimate can be obtained by requiring the maximum energy transferred in a single, binary collision to exceed the surface binding energy of the target,

$$E_{\text{th,min}} \geq E_{b,t}/\gamma - E_{b,p}, \quad (3.1)$$

where $E_{b,t}$ is the surface binding energy of the target, $E_{b,p}$ is the binding energy of a projectile particle to the surface and $\gamma = 4M_1M_2/(M_p + M_t)^2$ is the energy transfer factor in a single collision (Eckstein, 2007). Typical values for the sputtering threshold are in the range of a few 10 eV (Smentkowski, 2000).

The number of sputtered particles (and consequently Y) is governed by the differential energy loss near the surface and the range of recoil atoms, which determines the thickness of the layer from which sputtered atoms originate. Both quantities can be expressed in terms of respective stopping cross sections $S_i = dE_i/Ndx$. Consequently, the sputtering yield takes the form (Sigmund, 2012)

$$Y \propto \frac{S_p(E)}{S_t(U)} f(M_t/M_p). \quad (3.2)$$

Here, f is an increasing function of the mass ratio, S_p and S_t are the stopping cross sections of the projectile and recoil atoms, respectively, and U is the energy of the recoil atom. Since the distribution of sputtered atoms is heavily skewed to low energies, low energy recoils $U \ll E$ are of particular relevance here. For low ion energies ≤ 5 keV, an approximation including only nuclear energy loss can be given (Smentkowski, 2000) by

$$Y = 0.3 * M_p M_t \alpha E E_{b,t}^{-1} (M_p + M_t)^{-2}. \quad (3.3)$$

Here, a screened Thomas-Fermi potential is assumed for ion-atom interaction, and α is the corresponding screening radius. Thus, the sputtering yield shows a linear energy dependence at intermediate energies. The decrease of the sputtering yields at high energies (c.f. Fig. 3.1A) is explained by the vanishing of both nuclear and electronic scattering cross sections. Hence, only a small number of scattering events occur near the surface and $S_p(E)$ decreases within the range of low energy recoil atoms.

The angle dependence of the sputtering also shows a maximum at intermediate an-

3 Theory

gles of some 60° to 70°. Using a semi-infinite, isotropic medium but allowing for non-perpendicular ion incidence, Sigmund (1969) derived a dependence on ion incidence angle for the rising branch up to the maximum of

$$Y(\theta)/Y(0) = \cos^{-f} \theta \text{ for } \theta < \theta_{\max}. \quad (3.4)$$

Values for f generally lie in the range between 0.7 and 2.5 (Smentkowski, 2000). For all simulations and calculations performed in this thesis, an empirical formula for the angle dependence of sputtering with Ar^+ on Si was used based on Dieterle *et al.* (2011),

$$Y(\theta)/Y(0) = (1 + a \sin^b(\theta)) \exp\left(-c \left(\frac{1}{\cos(\theta)} - 1\right)\right), \quad (3.5)$$

with $a=4.92$, $b=3.30$ and $c=0.068$. This way, the angle dependence over the complete angle range can be described with a single analytical function.

3.1.2 Kinetic Theory of Surface Evolution

Continued removal of material from a surface by sputtering leads to surface erosion. Since the amount of material removed - and consequently the sputtering yield - depends on the geometric relations between incident ion beam and the local sample surface, changes in topography can occur. A number of reviews on the evolution of surface topography under ion beam bombardment are available (Katardjiev *et al.*, 1990; Carter, 2001; Makeev *et al.*, 2002; Frost *et al.*, 2009).

In the most general setting, surface evolution is not only governed by removal of target atoms due to sputtering, but can also contain contributions from different kind of atom transport phenomena. These transport phenomena can be collision induced, but also of thermal origin. For example, ballistic drift of recoil atoms which do not leave the surface, diffusion of surface atoms, or viscous flow can all affect surface evolution, as can redeposition of sputtered atoms. Furthermore, the random nature of the collision cascades as well as the random distribution of ion impacts onto the surface can lead to roughening effects, which occur on a sub- μm scale. Therefore, surface evolution is governed by a non-linear, stochastic equation, which can be given in the form (Carter,

3 Theory

2001)

$$\frac{\partial h}{\partial t} = \underbrace{-g}_{\text{Angle-dependent sputtering}} - \underbrace{\sum_{i=1,2} \left[\beta_i \left| \frac{\partial h}{\partial x_i} \right| + \delta_i \frac{\partial^2 h}{\partial x_i^2} + \kappa_i \frac{\partial^4 h}{\partial x_i^4} \right]}_{\text{terms for transport and higher-order sputtering}} + \frac{\nabla j_s}{N} + \underbrace{\eta(x_1, x_2, t)}_{\text{noise term}}, \quad (3.6)$$

where $h(x_1, x_2)$ is the local surface height. Here, g is the erosion velocity related to angle-dependent sputtering. The constants β_i , δ_i and κ_i are derived from the different transport mechanisms discussed above as well as curvature-dependent sputtering and j_s represents a possible directed flux of matter present in some anisotropic materials. Finally, η is a noise term reflecting the stochastic behaviour of sputtering. The term for angle-dependent sputtering g is given by

$$g = -\frac{JY(\alpha_S - \alpha_{\text{ion}}) \cos(\alpha_S - \alpha_{\text{ion}})}{N \cos \alpha_S}, \quad (3.7)$$

where α_S is the angle between z-axis and local surface normal and α_{ion} is the angle between ion beam incidence direction and z-axis (for simplicity, z-axis, surface normal and ion beam incidence direction lying in a single plane is assumed).

General solutions for the full evolution equation are not available. However, the asymptotic behaviour can be determined from power spectral density (PSD) analysis (for details, see Frost *et al.* (2009)). In particular, in the absence of directed flux effects ($j_s = 0$) and assuming uncorrelated, Gaussian noise $\langle \eta(q, t)\eta(q', t') \rangle = 2A\delta(q - q')\delta(t - t')$, the PSD function scales as¹

$$\text{PSD}(q, t \rightarrow \infty) = \frac{A}{R(q)} \text{ with } R = \sum_{i=1,2,4} C_i q^i. \quad (3.8)$$

The coefficients C_i are given by β_i , γ_i and κ_i from Eq. (3.6) up to a Fourier normalization factor. From the PSD, the rms roughness σ is obtained via

$$\sigma^2 = \frac{1}{2\pi} \int_0^\infty q \text{PSD}(q, t) dq. \quad (3.9)$$

Hence, roughening or smoothing of the surface for long erosion durations is controlled by

¹Note that for simplicity purposes, radial symmetry is also assumed here and the analysis is restricted to situations where the PSD converges for $t \rightarrow \infty$, i.e. no sputter instability is present.

the strength of the sputtering noise A and the strength of the different transport-related relaxation mechanisms.

3.1.3 Numerical Simulation of Surface Erosion

A two-dimensional algorithm described in Busch *et al.* (2018) was used to simulate the evolution of a notched surface under ion bombardment. The algorithm is a simplified version of the one used by Dieterle *et al.* (2011) using the same basic geometry but replacing the stochastic Monte Carlo method for sputter erosion by a deterministic model. The following assumptions are made:

- The sputter yield Y solely depends on the local ion-impact angle according to Eq. (3.5),
- ion flux is spatially and temporally uniform,
- the sample medium is homogeneous and isotropic as well as semi-infinite (the edges of the sample are treated as infinitely far away from the notches) and
- shadowing is incorporated, but no redeposition or diffusion process.

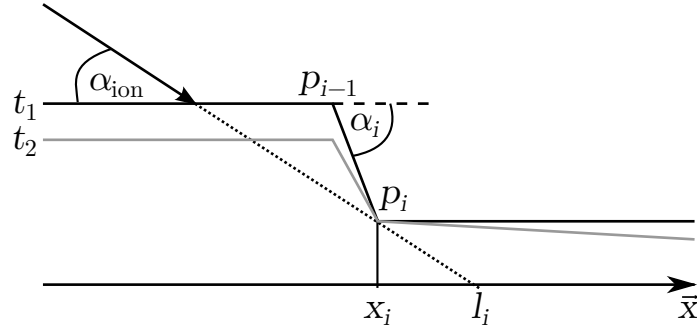


Figure 3.2: Geometric model used for surface erosion simulations.

A two-dimensional, cross-sectional geometry of the surface perpendicular through a notch was used (c.f. Fig. 3.2). At each point of time, the surface is modelled as a string of points (x_i, h_i) with related local surface inclination angles α_i . Furthermore, in order to determine if shadowing occurs, an effective length l_i is calculated at each surface point by projection along the ion beam onto the x-axis. The shadowing condition then reads: a point i is shadowed if there exists a point $j < i$ with $l_j \geq l_i$. All points which are not

3 Theory

shadowed are subject to erosion according to Eq. (3.7). A time scale factor $K = 0.0004$ is used to control the amount of material removed within one simulation cycle. This time was chosen such that satisfactory results were obtained in terms of numerical stability and computation speed.

The chosen model and the set of assumptions are well suited in order to capture the major aspects of surface evolution for notched surfaces subject to ion bombardment. The experimental results discussed in Section 5.2.1 indicate that the primary roughening mechanisms are related to the quality of the notch cut rather. Thus, neglect of processes which act on a nm-scale, such as sputter noise or diffusion, do not contribute to the surface topography in a significant way. Moreover, curtaining effects on the notch and similar artefacts primarily lead to the formation of ripples with a wave vector parallel to the notch. As such, they fundamentally cannot be replicated in a two-dimensional, cross-sectional model.

3.1.4 Erosion of a Surface With Initial Notches

Erosion of a surface with initial notches was first described by Busch (2016) and Busch *et al.* (2018), where the technique has been proposed for TEM sample preparation. In the following paragraphs, a short review of the basic aspects is given following the presentation in Busch *et al.* (2021a).

Upon ion beam erosion of a notched surface at grazing incidence, ions impinge on the face of the notch at an locally increased angle. As a consequence of the angle dependence of sputtering (c.f. Section 3.1.1), the local removal rate is increased and preferential removal of material occurs. However, ions are only able to hit the upper part of the notch face due to shadowing of the lower part by the surface in front of the notch (Fig. 3.3A). As a result, formation of a terrace is facilitated at a particular, well-defined depth below the initial surface. For a spatially homogeneous and parallel beam on a flat substrate, this depth is defined by the width of the notch w_N and the ion incidence angle θ_{ion} according to the geometric relation

$$\Delta h = \tan \theta_{\text{ion}} \cdot w_N \quad (3.10)$$

if the ion beam is perpendicular to the notch. If the incidence direction is slanted by an angle φ relative to the notch, w_N has to be replaced by $w_N / \cos \varphi$.

The terrace geometry does depend on the notch geometry, as revealed by simulations.

3 Theory

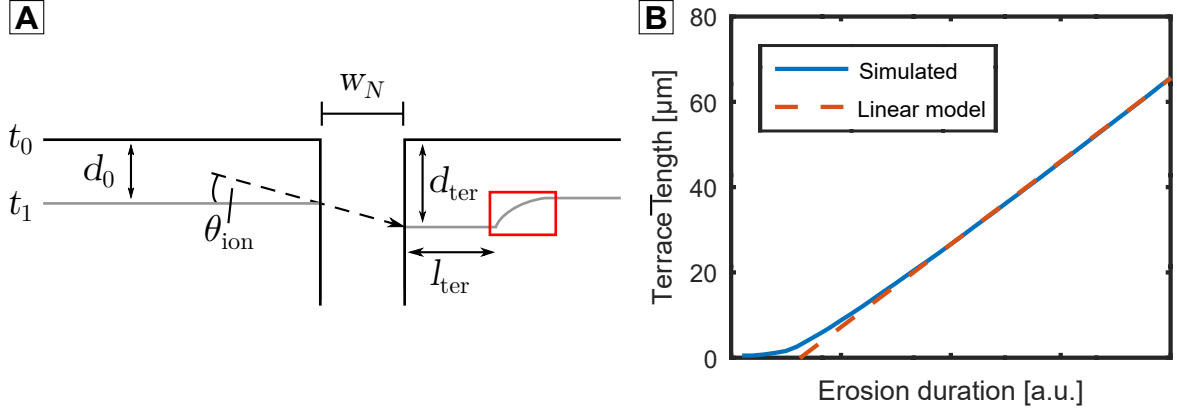


Figure 3.3: Geometric quantities describing the final geometry of the sample surface (A) and qualitative growth kinetics of the terrace (B).

In the case of perfectly perpendicular notches and a homogeneous ion beam, the terrace is flat and parallel to the initial surface. However, if the notches are rather V-shaped, a terrace with an inclination of a few degree relative to the initial surface is formed. It was found that this inclination is caused by the 'shrinking' - i.e. a reduction in notch width - of a V-shaped notch upon continued erosion, (details can be found in Busch *et al.*, 2018). Furthermore, the notch width and the depth difference between terrace region and regular surface also decrease with erosion duration. In experimental settings, these effects can additionally be superseded by beam divergence and shape effects.

The kinetics of the erosion process were found to exhibit two phases. Following a transient first phase, a steady-state evolution is eventually reached. The first phase comprises the initial formation of the terrace. In the process, a curved, sloped region at the end of the terrace (red inlay in Fig. 3.3A) is also formed and it's shape does exhibit a similar transient evolution. During this first phase, the terrace area shows little growth (c.f. Fig. 3.3B). Finally, the second phase is characterized by terrace growth at a constant speed, which depends on the initial notch geometry and beam properties, in particular ion current and on incidence angle. It is important to note that the two processes of terrace formation and terrace growth occur in parallel to the erosion of the mean surface according to Eq. (3.6) and Eq. (3.7). Precise relations between mean erosion depth of the surface, terrace depth and terrace length have yet to be derived. This problem is treated in Section 5.3.

3.2 Electron Backscatter Diffraction

3.2.1 Measurement Principle

Orientation determination with EBSD is based on the detection and subsequent analysis of EBSPs, which contain a particular set of bands depending on crystal structure and orientation. There are several good reviews available describing the technique and its application (Wilkinson & Hirsch, 1997; Humphreys, 2001) as well as an extensive edited volume by Schwartz *et al.* (2009).

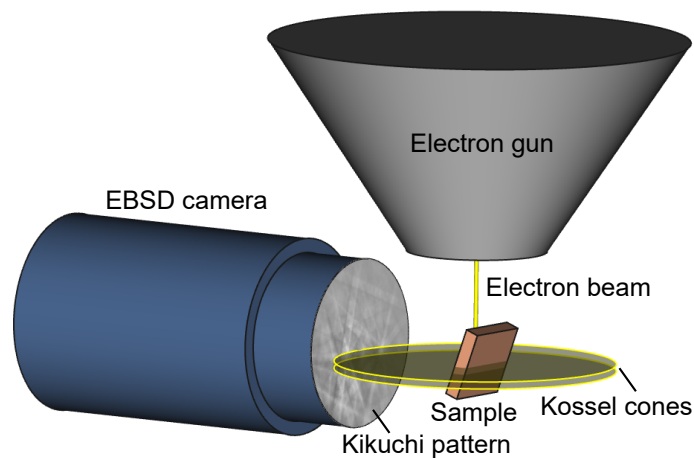


Figure 3.4: Experimental setup for an EBSD measurement.

The basic measurement principle can be described as follows: an incident electron beam undergoes a series of collisions inside the sample, which is held at a high inclination angle of typically 60° to 70° from the horizontal position (Fig. 3.4). The electrons which are scattered back towards the surface and subsequently leave the sample are detected using a luminescent phosphor screen and a light-sensitive camera². The recorded EBSP are subsequently processed using background correction (Dingley *et al.*, 2005) and noise-reducing or contrast-enhancing filters. An automatic band detection algorithm based on the Hough transform (Duda & Hart, 1972) is used to determine the position of high-intensity bands in the EBSP. Finally, potentially fitting orientations are deduced from the EBSP by comparing the measured angles between bands to inter-planar angles from a material-specific look-up table (also called material file). By applying a voting

²Direct electron detection (Wilkinson *et al.*, 2013) is increasingly used as alternative to luminescence based cameras.

3 Theory

procedure to the sets of all possible solutions which are consistent with the detected bands (Wright & Adams, 1992), the most probable solution is determined. The crystal structure information contained in the material files usually stems from high resolution X-ray diffraction measurements, which is compiled and available in several commercial databases. In this thesis, the Inorganic Crystal Structure Database (ICSD) by FIZ Karlsruhe (Rühl, 2019) was used.

The formation of bands in the EBSP can be qualitatively understood by assuming a virtual point source in the interaction volume of the electron beam. Tracing the Bragg condition from this source leads to the construction of scattering cones (Kossel cones). When Kossel cones are projected onto the detector screen, hyperbolic bands are formed. However, a more accurate and quantitative understanding of EBSP requires the incorporation of dynamic scattering theory. Following Winkelmann (2010), the formation of EBSP can be considered in terms of a two-stage model: electrons are scattered inelastically, leading to the presence of incoherent, independent sources inside the interaction volume, which are subsequently elastically scattered at the lattice planes. Simulations based on a Bloch-wave approach have shown good agreement with experiments (Winkelmann *et al.*, 2007).

In order to obtain spatially resolved orientation data, the electron beam is scanned over the surface, a pattern is recorded at each point and the analysis outlined above is applied. Additionally, two further quantities are calculated for each point in the scan which are very useful for visualizing and analysis purposes: image quality (IQ) and confidence index (CI). The image quality value is defined as the mean intensity of the detected bands in Hough space

$$\text{IQ} = \frac{1}{N} \sum_{i=1}^N H_i, \quad (3.11)$$

where $H_i = H(r_{\max,i}, \theta_{\max,i})$ is the value of the Hough transform at the detected peak positions $(r_{\max,i}, \theta_{\max,i})$ and N is the maximum number of bands which are considered for indexing. The IQ value exhibits pronounced contrasts for strained crystals and grain boundaries (Wright & Nowell, 2006)³. Using IQ to control pixel brightness is very useful for visually suppressing residual glass in partly crystallized glass ceramics as well as making grain boundaries more easily discernable. The confidence index $0 \leq \text{CI} \leq 1$ is a measure for the uniqueness of the orientation solution determined by triplet voting

³There are alternative metrics available for the pattern quality with different contrast characteristics. A comparison of these metrics is also given by Wright and Nowell (2006).

3 Theory

(Field, 1997). It is defined as

$$\text{CI} = \frac{N_{\text{votes},1} - N_{\text{votes},2}}{N_{\text{votes},\text{max}}}, \quad (3.12)$$

where $N_{\text{votes},i}$ is the number of votes of the orientation solutions which received the most (1) and second-most (2) votes, respectively, and $N_{\text{votes},\text{max}}$ is the maximum number of possible votes (which depends on the number of detected bands N included into the voting procedure). Thus, a low CI value either stems from the presence of at least two solutions with similar number of votes - indicating ambiguous, unreliable indexing - or from the complete absence of a solution with a significant number of votes. The first case can arise if pseudo-symmetry is present in the crystal structure or in the presence of several similar phases. The second case can arise for deformed, damaged or amorphous material. For any texture calculation performed in this thesis, only data points with $\text{CI} > 0.1$ have been included, thereby effectively filtering out data points stemming from residual glass.

3.2.2 Representation of Orientations and Texture

The orientation of a crystal is defined as the spatial relation of the crystal lattice to a chosen reference frame⁴, disregarding translations. More precisely, orientations are identified with transformations between the two frames that leave the origin and handedness of both frames invariant. These transformation are the proper rotations in three dimensions. In the absence of symmetries, the orientation space is thus given by the group of proper rotations $SO(3)$. In-depth treatments of orientations and orientation spaces can be found in monographs by Bunge (1993) and Morawiec (2004).

According to active convention (following the treatment of Mason and Schuh (2009)), each orientation is identified with a mapping $R \in SO(3)$ that transforms vectors \vec{x} initially aligned with the reference frame into the vector $O\vec{x}$ aligned with the crystal. If the crystal exhibits any point symmetries P_i , then all orientations RP_i equivalent to R are obtained by right multiplication. On the other hand, statistical symmetries S_j in the distributions of orientations (so called sample symmetries caused by the processing history of the material) imply a set of statistically equivalent orientations S_jR .

⁴Typically in EBSD, a reference frame tied to the sample surface is chosen such that the z-axis is equal to the surface normal. The x- and y-axis are often chosen based on sample processing history, e.g. using rolling direction and transverse direction in rolled metals.

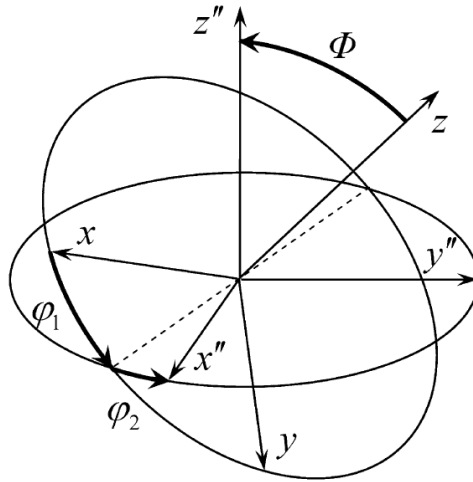


Figure 3.5: Effect of three successive rotations by Euler angles $(\varphi_1, \Phi, \varphi_2)$ (from Mason and Schuh (2009)).

Euler angles are the most commonly used parametrization of orientation space⁵. In Euler angle representation (following conventions introduced by Bunge (1993)), an orientation is defined by three successive rotations of the coordinate frame (Fig. 3.5). First, a rotation by $\varphi_1 \in [0, 2\pi)$ around the initial z -axis is performed, then a rotation by $\Phi \in [0, \pi)$ around the new x' -axis (dashed line in Fig. 3.5) and finally, a rotation by $\varphi_2 \in [0, 2\pi)$ around the new z'' -axis is performed.

The statistical distribution of crystal orientations in a polycrystalline material (crystallographic texture) is often relevant in determining macroscopic properties of a material. It can be described quantitatively in terms of the orientation distribution function (ODF), which is a normalized probability density f in orientation space. Thus, for any region in orientation space $O \subset SO(3)$, the probability of finding orientations within O at a given point in the data set is then $p(O) = \int_O f dV$. Furthermore, the normalization condition $\int_{SO(3)} f dV = 1$ is satisfied. The ODF is commonly expressed as a series expansion in terms of a suitable set of basis functions, such as generalized spherical harmonics (Euler angle representation of $SO(3)$) or hyperspherical harmonics (quaternion representation of $SO(3)$, see Mason and Schuh (2009)). The expansion of the ODF in terms of generalized

⁵For a succinct discussion of other parametrizations, such as quaternions, axis-angle parametrization and Rodriguez parametrization, see Mason and Schuh (2009).

3 Theory

spherical harmonics $T_l^{mn}(\varphi_1, \Phi, \varphi_2)$ with complex coefficients D_l^{mn} is given by

$$f(\varphi_1, \Phi, \varphi_2) = \sum_{l=0}^{\infty} \sum_{m=-l}^l \sum_{n=-l}^l D_l^{mn} T_l^{mn} \quad (3.13)$$

$$D_l^{mn} = \frac{2l+1}{8\pi^2} \int_0^{2\pi} \int_0^{2\pi} \int_0^{\pi} f T_l^{*mn} d\Phi d\varphi_1 d\varphi_2 \quad (3.14)$$

Definitions and in-depth discussions of the generalized spherical harmonics can be found in Bunge (1993). Computation of the series to high orders of l can be computationally expensive and in practice, only a finite number of coefficients is calculated and the series terminated at a maximum order of l_{\max} . Artefacts or regions of negative density can arise if an insufficient amount of terms is included in the expansion, particularly if the texture exhibits very sharp features as in the case of a fibre texture. An alternative approach is discrete binning. Consider a finite partition of $SO(3)$ into subsets $V_i \subset SO(3)$, then

$$f(V_i) = \frac{N_i}{V_i N} \quad (3.15)$$

provides a discrete approximation of the ODF (N_i is the numbers of data points with orientation in V_i and N the total number of data points). In this thesis, a partition in terms of Euler angles with constant bin sizes of $5^\circ \times 5^\circ \times 5^\circ$ has been used for texture calculations. Furthermore, the binned texture was smoothed using a Gaussian filter. It should be noted that, given the volume element is $dV = \sin \Phi d\varphi_1 d\varphi_2 d\Phi$ in Euler angles, this partition leads to bins of unequal size. As a consequence, the ODF is smeared over larger volumes at values close to $\Phi = \pi/2$ compared to Φ close to 0 or π .

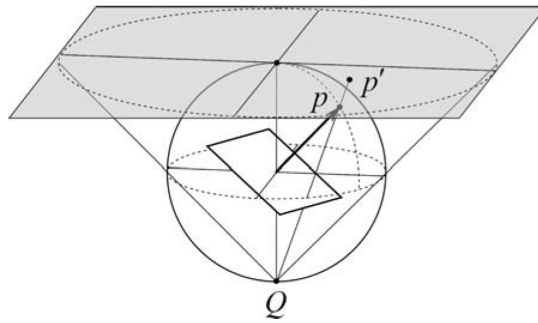


Figure 3.6: Construction of a pole figure by projection of the unit sphere onto the plane (from Mason and Schuh (2009)).

3 Theory

For visualization purposes, reduced descriptions in terms of crystal directions rather than fully three-dimensional orientations are often useful. Of particular interest in this thesis are the normal directions to certain low-index lattice planes. Let \vec{x} be such a plane normal, then the orientation of \vec{x} in the sample frame is given by a point on the unit sphere S^2 in three dimensions. Projection of the unit sphere - or more precisely a chosen hemisphere - onto the plane provides a pole figure representation of the orientation (Fig. 3.6). Either stereographic projection or equal-area projection can be used. The first one is advantageous for visualizing angle relations, the second one for representing distribution functions. By inverting the role of crystal direction and sample frame, an inverse pole figure is obtained. Here, the orientation of a fixed sample direction relative to the crystal frame at given data point is represented.

4 Methods and Materials

4.1 Sample Preparation and Processing

Notch creation

Notches were created on the sample surface using a VION PFIB (FEI Company, Hillsboro, OR, USA) with Xe^+ ions at 30 keV. A rectangular pattern which is repeatedly scanned by the ion beam was used with ion currents up to 0.5 μA . Further polishing steps were performed using rectangular scan patterns which are scanned line by line, i.e. where each successive line is only started once the full ion dose was applied to the preceding scan line. The final polishing steps were performed at ion currents as low as 2 nA. According to existing characterization data of the ion source in Smith *et al.*, 2006, these settings correspond to beam spot sizes of 1.5 μm and 150 nm, respectively. For dielectric samples (glass, glass ceramics), irradiation of the sample with low energy electrons from a flood gun was performed for charge compensation.

Ablation with an ultra-short pulsed laser was used as an alternative method for notch creation. For this purpose, a microTMS device (3D-Micromac, Chemnitz, Germany) equipped with a laser at a wavelength of 1028 nm was used. Milling was performed at 514 nm wave length using second harmonic generation. The laser pulse length was 211 fs and the pulse repetition rate was 60 kHz. Notch cutting was performed at 20 mW on Si and 50 mW on all glass and glass ceramic samples. Layerwise scanning was used as a milling strategy and the scan direction was rotated by 53° after each layer to reduce artefacts linked to directional redeposition of ablated material. A carbon dioxide snow-jet incorporated into the microTMS device was used in order to clean the sample and remove redeposited material from the surface.

Glancing angle ion beam erosion

Glancing angle ion beam erosion was applied to notched surfaces for the purpose of terrace formation. Two broad ion beam polishing devices were applied, PIPS II and Illion II (both Gatan, Inc., Pleasanton, CA, USA). Both devices feature similar pairs of penning ion guns, providing low energy Ar^+ ions at gracing incidence. Ion incidence angles between 2° and 10° from the surface and ion energies of 1 keV (final polishing) and 4 keV were used in this work. Unless otherwise noted, all experiments were performed with a stationary ion incidence direction. An oscillating erosion scheme with milling sectors up to $\pm 30^\circ$ was used in one series of experiments. Samples were mounted using conductive silver adhesive (PLANO, Wetzlar, Germany).

As an alternative approach, glancing angle ion beam erosion was also performed with PFIB instead of broad ion beam (BIB) using a milling pattern covering an extended area around the notch. For this purpose, the sample was mounted on a pre-tilted sample holder. An angle of 10° to the sample surface was used and milling was performed using a box scan pattern. A range of ion irradiation conditions have been employed, varying pixel dwell time (40 ns to 1 μs) and ion current (6.7 nA to 1.3 μA). Furthermore, an offset in focus of up to 2 mm was used in order to increase the beam diameter and create quasi-broad ion irradiation conditions. Experiments have been performed both with and without electron flood gun.

TEM lamella preparation

Preparation of electron transparent lamella for transmission electron microscopy (TEM) was performed using a Auriga 40 cross beam FIB (Zeiss, Oberkochen, Germany) with Ga^+ liquid metal ion source. After deposition of a protective Pt bar, milling and thinning of the lamella was performed at 30 keV. After lift-out, the lamella was thinned to electron transparency, with the final polishing step being performed at 2 keV ion energy.

4.2 Surface Metrology

Scanning electron microscopy

Scanning electron microscopy was performed for qualitative surface inspection as well as microstructure analysis. For non-analytic surface investigation, an environmental

4 *Methods and Materials*

SEM Quanta 650 FEG (FEI Company, Hillsboro, OR, USA) was used. Micrographs of dielectric samples (glass, glass ceramic) were taken at low vacuum conditions between 60 Pa and 100 Pa without applying additional sample coating. A dedicated large field detector (LFD) for low vacuum conditions was used in these cases, whereas an Everhart-Thornley secondary electron detector was used in case of conductive samples suitable for high vacuum measurement conditions. Samples were mounted using adhesive carbon pads.

For investigation of conducting specimen, scanning electron microscopes of type SU70 (Hitachi, Hitachinaka, Japan), Supra 55 VP and Sigma 300 (both Zeiss, Oberkochen, Germany) equipped with Schottky field emission guns were used. All microscopes are equipped with Everhart-Thornley secondary electron detectors and in-lens detectors. In the case of the SU70 microscope, an additional E×B-filter was used positioned before the in-lens detector to influence the signal composition. Backscattered electron micrographs have been recorded with a four-quadrant backscattered electron detector (point electronic, Halle, Germany) on the Sigma 300 microscope.

In order to avoid sample charging, insulating samples were coated with a thin carbon layer using a Leica EM SCD500 high-vacuum sputter coater. Additionally, samples were mounted on the stub using silver paint, which was also applied to the side faces of the samples in order to improve electric contact.

Optical profilometry

Topography measurements were performed using a MS-500 white light interferometer and the measurement software TMS 3.7 (both Polytec, Waldbronn, Germany). For illumination, a diode with mean wave length of 766 nm and coherence length of 12 μm was used in conjunction with a 5×Michelson objective and a 50×Mirau objective. For erosion depth measurements, samples were partly covered with carbon tape during broad ion beam erosion in order to determine an unmodified reference surface. Topography measurements were performed prior to and after ion beam erosion and the data aligned on the protected part of the surface. Erosion depth was calculated by subtraction of both topography datasets. Image processing and alignment was performed using ImageJ.

4.3 Microstructure Analysis

Most of the EBSD measurements in this thesis were performed on the SU70 microscope. However, due to equipment failure, the measurements on fresnoite after initial notch sectioning were performed on the Supra 55 VP microscope. Both microscopes are equipped with EBSD systems by EDAX, Inc. (Pleasanton, CA, USA). In the case of the SU70, a phosphor screen-based Hikari camera with a maximum pattern resolution of 640×480 pixel was used, whereas a Digiview Camera with maximum resolution of 1392×1040 was used in the Supra 55 VP. Data collection was performed using the software OIM DC v7.31 and data analysis was performed using OIM Analysis v7.31.

Individual patterns were collected without camera binning, whereas binning of 4×4 and 2×2 was applied for large area scans of diopside and (BTS) fresnoite, respectively. Both static and dynamic background correction (c.f. Dingley *et al.* (2005)) were applied to the patterns as well as histogram normalization. For EBSD analysis of BTS crystals after initial notch sectioning, additional pattern processing was performed using local pattern averaging (NPAR, see Wright *et al.*, 2015). This additional processing step was necessitated by deteriorating crystal homogeneity at increasing depth from the surface. At least 5 and at most 8 bands were used for indexing. The material file used for indexing diopside was based on the Inorganic Crystal Structure Database (ICSD) entry 30522 (Sasaki *et al.*, 1980) and the material for $\text{Ba}_2\text{TiSi}_2\text{O}_8$ fresnoite (BTS) was based on ICSD entry 4451 (Moore & Louisnathan, 1969). Scans were performed with an electron current of 10 nA.

TEM analysis of ion beam-induced amorphization was performed in a Tecnai G2 TF20 microscope (FEI Company, Hillsboro, OR, USA) at 200 kV acceleration voltage. Scanning transmission electron microscopy (STEM) analysis of a fresnoite sample was performed in Titan³ G2 80-300 (FEI Company, Hillsboro, OR, USA) aberration corrected microscope.

4.4 Materials

Erosion experiments were performed on smooth, chemically-mechanically polished and textured monocrystalline (100) silicon, and uncoated float glass microscope slides (article number 631-1522, VWR International bv, Leuven, Belgium). Two surface crystallized glass ceramic samples were investigated in this study, which are described in the subsequent sections.

MgO · CaO · 2 SiO₂ glass ceramic (diopside)

The first model system in this thesis was a diopside glass ceramics. Batches of diopside composition (MgO · CaO · 2 SiO₂) were melted using CaCO₃, MgO and SiO₂ raw materials by Carl Roth. An addition of 1wt% Al₂O₃ (Pengda, Munich, Germany) was used in order to inhibit volume crystallization. Melting was performed in a Pt-crucible at 1480° for 1 h. The melt was stirred for a further hour at 1500°C. Then, the melt was poured onto a steel mold pre-heated to 740°C and held in an electric chamber furnace while cooling to room temperature.

From the glass, blocks of 5 × 5 × 5 mm³ were separated by sawing with a diamond saw (Brilliant 265, ATM GmbH, Blieskastel, Germany). The top-side was ground and polished with SiC-papers (Struers, Willich, Germany, 2017: #P200, #P600, #P1200) and diamond lapping foils (Bierther Submicron, Bretzenheim, Germany; diamond grain sizes 16 μm, 9 μm, 5 μm, 3 μm and 1 μm) using a FS 640 Z CC grinding machine (Geibel und Hotz GmbH, Homberg, Germany) and a MetaServ 250 polishing machine (Buehler, Germany, Esslingen am Neckar). Annealing was performed at 850°C for 85 min. For this purpose, the sample was placed inside a fused silica glass tube within an electric chamber furnace (Linn High Therm GmbH, FRH-20/150/1100, Eschenfelden, Germany). The furnace itself was stationed inside a glovebox (Weidener KG, GB 90 100/2) which was continuously flushed with filtered air in order to prevent contamination with particles which could influence surface nucleation. Furthermore, zeolite and silica-gel were used to decrease the humidity inside the glove box to a dew point of −30°C.

2 BaO · TiO₂ · 2.75 SiO₂ glass ceramic (BTS fresnoite)

The second material analyzed in this thesis was a fresnoite glass ceramic surface-crystallized in dry air from a glass with excess SiO₂. For this purpose, a glass with nominal composition of 2 BaO · TiO₂ · 2.75 SiO₂ was melted from BaCO₃, TiO₂ and SiO₂ (raw materials from Merck, VEB Jenapharm Laborchemie Apolda and Carl Roth, respectively). Compared to the composition of the BTS fresnoite crystal phase 2 BaO · TiO₂ · 2 SiO₂, this constitutes an excess of approximately 8 mol%, which serves to inhibit volume crystallization. Melting was performed in a Pt-crucible at 1530°C for 30 min, followed by stirring at 60 rpm for an additional hour. The melt was then poured into a pre-heated steel mould, held at a temperature of 740°C for one hour in a laboratory furnace and finally cooled to room temperature.

4 *Methods and Materials*

From the glass, cubes of $5 \times 5 \times 5 \text{ mm}^3$ were created by fracturing with a plier tool and then immediately transferred into a vacuum tubular furnace (F-VS 70-200/13, GERO Hochtemperaturöfen GmbH). Annealing was performed at 825°C in a dry air atmosphere with $48 \pm 5 \text{ ppmv}$ water (controlled with a humidity sensor TF-2R-TOE-1, PANAMETRICS, Germany). The heating rate was 24 K min^{-1} and the holding time at the target temperature was 75 min. X-ray diffraction analysis of the sample performed with a Rigaku MiniFlex 300 in $\theta - 2\theta$ arrangement using $\text{Cu } K_\alpha$ radiation did not provide evidence of other crystal phases than fresnoite.

STEM analysis results from a second fresnoite sample are presented in this thesis and compared with the sample sectioned using initial notches. This sample was prepared in the same way outlined above, but annealed for 225 min in an Ar atmosphere at an humidity of $\leq 3 \text{ ppmv}$.

5 Erosion of Surfaces With Initial Notches

Fundamental aspects concerning the erosion of a surface with initial notches are the focus of this chapter. Expanding upon previously established results (Section 3.1.4), extensions are made both to the sample preparation process as well as understanding and modelling of the resultant surface, particularly in the terrace region. First, different technological realizations of the initial notch approach are evaluated on selected model systems in order to determine applicability and limits of each variant. Then, the properties of the resultant surface in the terrace region are investigated in detail, putting particular emphasis on aspects relevant to sample quality (surface roughness, ion-induced amorphization). Next, the evolution of the surface as well as the final surface geometry is investigated using both theoretical approaches and experiments. Crucially, a linearized framework for the evolution of the terrace is proposed which is well suited to support process design and correct choice of milling parameters. Finally, implications of the findings for applications of initial notches to sample preparation tasks are discussed.

5.1 Evaluation of Surface Processing Methods

Two different processing steps can be distinguished, which are treated separately here: creation of the notch and glancing-angle erosion of the notched surface. Notch creation requires targeted removal of material with spatial dimensions on the order of $10\ \mu\text{m}$. Past attempts have utilized ablation with short pulsed (490 ps) laser ablation for this purpose (Busch *et al.*, 2018). However, this resulted in low-quality notches due to redeposition of material from the directed plasma plume onto the side faces of the notch, leading to roughening upon subsequent glancing-angle erosion of the notched surface. Here, two alternative techniques for notch creation are evaluated: focused ion beam milling and laser ablation using an ultra-short pulsed laser (fs pulse duration). The second process, glancing-angle erosion, is performed with both a broad ion beam polisher as well as with focused ion beam erosion at high sample tilt. All processes are evaluated on two

5 Erosion of Surfaces With Initial Notches

model systems. As a widely used conducting material, monocrystalline (100) Si is used, whereas uncoated float glass microscope slides were used as a model for a non-conducting, amorphous target. The combinations of materials and processing techniques described in this section are visualized in Table 5.1.

Notch creation	Terrace formation	Material
FIB fs-laser	BIB FIB	(100)-Si float glass

Table 5.1: Combinations of processing methods and materials analyzed in this work.

5.1.1 Notch Creation

Notch milling with high current PFIB erosion was evaluated both on smooth, chemically-mechanically polished and textured Si wafers with significant roughness. Smooth notch faces can often be created in a single box milling step at high currents (0.2 μA to 0.5 μA) without further polishing steps (Fig. 5.1A). On textured wafers, some degree of topography-induced curtaining was often observed, which could then be smoothed with a single polishing step. In some milling settings, topography formation was also observed on smooth wafers (Fig. 5.1B) upon single-step box milling. This could be either a result of insufficient beam alignment or of redeposition during milling, which can be expected to depend on the notch geometry (in particular aspect ratio).

On glass, pronounced notch face roughening was observed after box milling (Fig. 5.1C), even when applying flood gun charge compensation. Close to the surface, the topography is characterized by plateaus which are aligned parallel to the surface. After the first few microns, the topography starts to change towards a more columnar, basalt-like topography. Polishing steps at intermediate currents in the 10 nA range did not significantly reduce this topography. Only after extended polishing at low currents (70 min at 2 nA), a smooth notch face could be prepared. Notably, no similar topography formation was observed on the bottom of the notch.

Boxes milled using fs-pulsed laser ablation are shown in Fig. 5.2. On polished Si (Fig. 5.2A), isotropic roughening of the notch faces was observed, but no ripple formation or other directional topographic features. The notch faces on glass exhibit a formation of facets with a typical diameter on the order of 500 nm. Significant amount of debris are deposited around the notch during laser cutting on Si and to a lesser degree on glass.

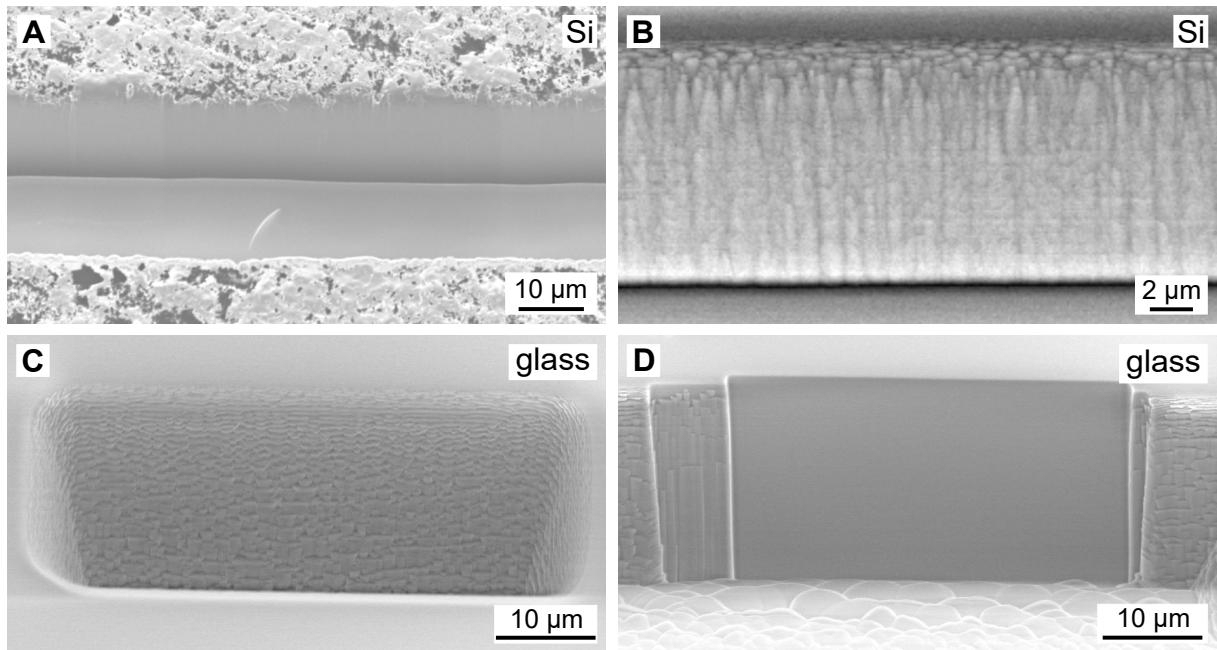


Figure 5.1: PFIB milling of initial notches on Si without notch face roughening (A) and with limited notch face roughening (B). Notch milling on glass without final polishing (C) and (D) with extended final polishing.

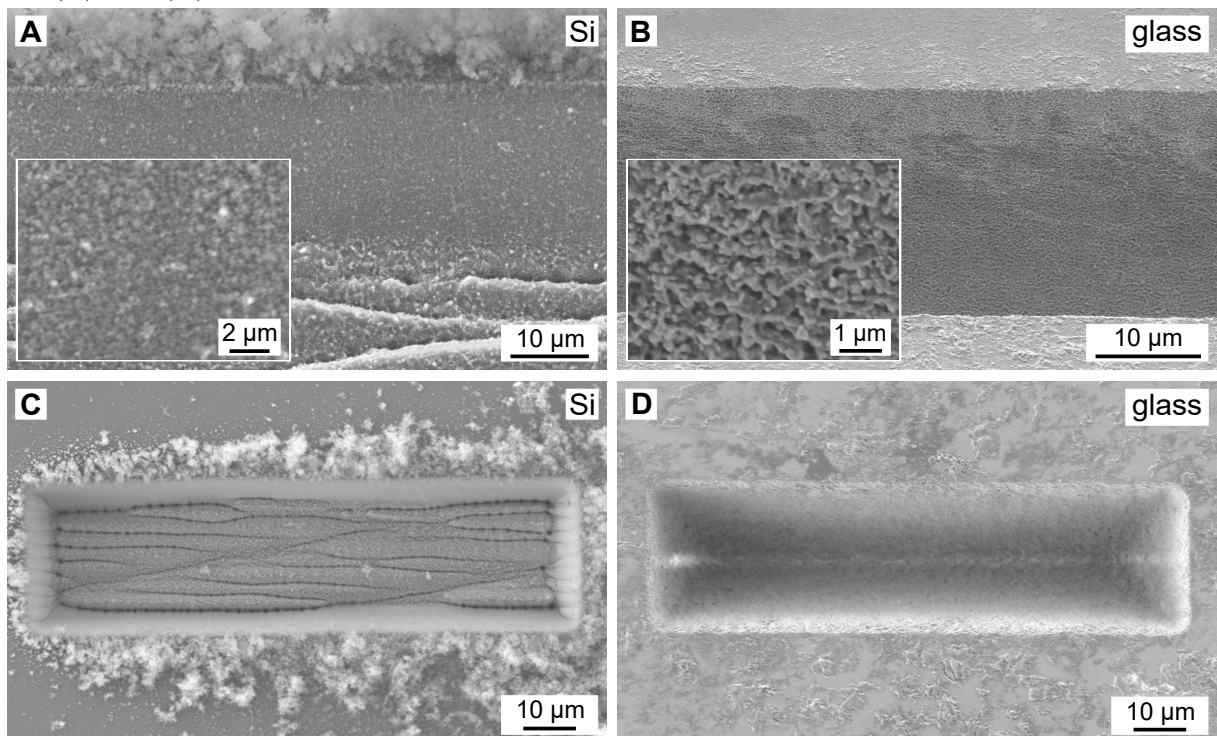


Figure 5.2: SEM micrographs of notches created by fs-pulsed laser ablation in Si ((A) and (C)) and glass ((B) and (D)). Micrographs taken at 40° and 0° stage inclination, respectively. Inlays in (A) and (B) show the notch face at higher magnification.

Sample cleaning with the CO₂ snow-jet was able to reduce, but not fully remove debris. Notches milled on glass showed a wedge form without a discernable base area (Fig. 5.2D), in contrast to Si, which showed a more rectangular box shape (Fig. 5.2C). Only on very large notches of linear dimensions larger than 50 μm could a more rectangular box shape be achieved on glass. Increasing the laser power exerted only limited influence on notch shape. A larger ablation threshold and lower ablation rate was observed on glass compared to Si, necessitating a higher laser power level for machining the former (laser machining was performed at 50 mW and 20 mW, respectively).

5.1.2 Terrace Formation by Glancing-Angle Ion Beam Erosion

Terrace formation by glancing-angle erosion was evaluated for focused and broad ion beam milling. On polished Si, very smooth terraces can be created using broad ion beam erosion (Fig. 5.3A). However, roughening caused by artefacts on the notch faces was occasionally observed, as was some influence of the initial roughness on textured Si. These aspects are dealt with more thoroughly in Section 5.2.1. On glass, terraces with very limited roughness could be created even when using notches without further polishing (Fig. 5.3B).

Terrace formation could be successfully realized with glancing-angle focused ion beam erosion on Si. In Fig. 5.3C, a sample is shown where the scan pattern did not cover the notch completely. Here, terrace formation only occurred in the limited region subjected to the ion beam. Terrace roughening was observed in some experiments. In particular, formation of ripples parallel (wave vector perpendicular) to the ion beam was observed. These ripples are reflecting the lateral pixel offset of the ion beam, indicating deviation from a quasi-broad beam setting.

For the glass sample, terrace formation could also be realized with focused ion beam erosion at currents of 59 nA (Fig. 5.3D). However, significant roughening of the surface occurs which exhibits similar features observed for the PFIB-milled notch faces in Fig. 5.1C. At higher currents up to 1.3 μA , the terrace becomes distorted and less distinct in form, but without noticeable change to the pattern of the surface roughness. Neither changes to the pixel dwell time of the ion beam (50 ns to 1 μs) nor to the flood gun led to appreciable improvements. However, variation of the ion incidence angle led to pronounced changes in topography. In Fig. 5.4, results of milling on glass surface without notch at different incidence angles are shown, indicating a transition from longitudinal, basalt-like patterns to transversal ripples.

5 Erosion of Surfaces With Initial Notches

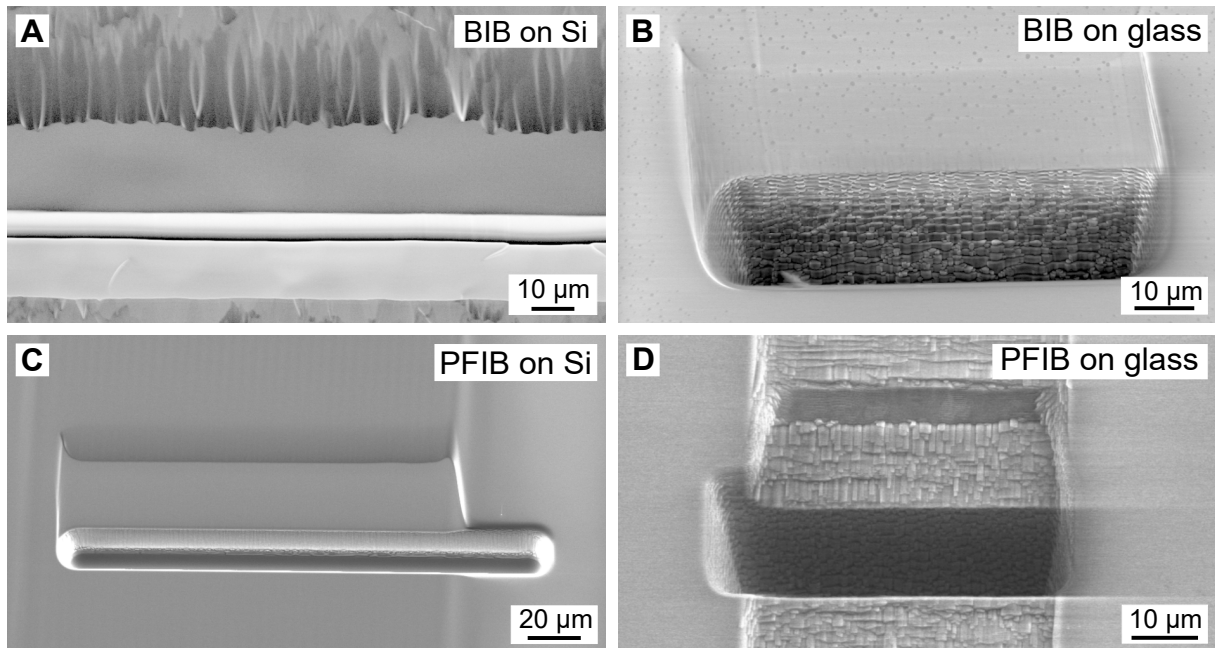


Figure 5.3: Glancing angle erosion of a notched surface performed at 10° incidence angle with broad and focused ion beams. (A) Mono-Si eroded with BIB, (B) glass eroded with BIB, (C) Si eroded with PFIB and (D) glass eroded with PFIB at 59 nA ion current. Notches were created with PFIB milling as in Fig. 5.1.

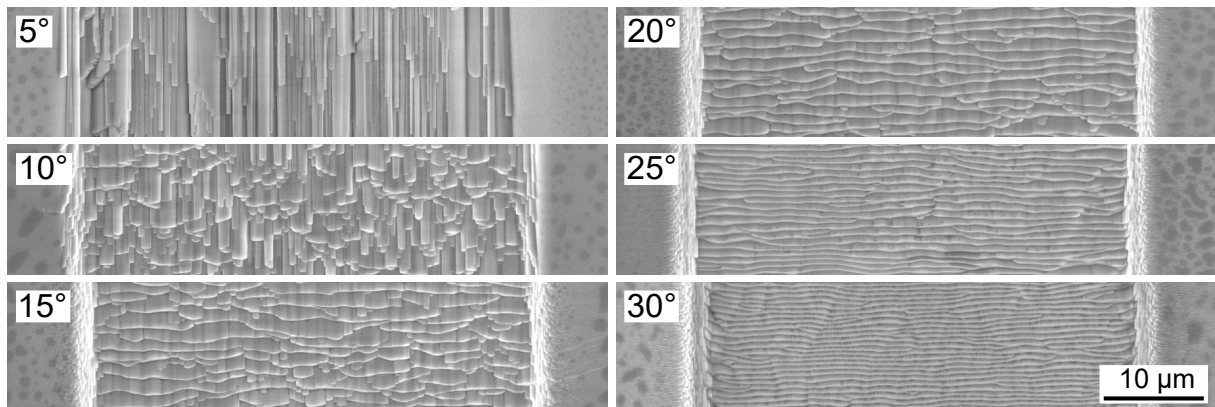


Figure 5.4: PFIB erosion of a float glass substrates at ion incidence angles between 5° and 30° to the surface. Milling was performed at 59 nA using an electron flood gun for mitigation of sample charging. All micrographs are taken at the same magnification.

5.2 Surface Properties in the Terrace Region

5.2.1 Terrace Roughness

Surfaces with well-defined groove patterns were used to study the influence of initial surface topography on the terrace roughness. For this purpose, initially smooth, chemically-mechanically polished Si wafers have been processed with focused ion beam erosion. After cutting the notches, grooves were milled both onto the surface adjacent to the notch as well as onto the notch faces. Surface configurations with different groove orientation relative to the notch were studied, using both parallel orientation, perpendicular orientation and as well as grooves slanted at an angle of 45° . A sketch of the different geometric configurations is shown in Fig. 5.5. Glancing angle erosion was performed with broad ion beam milling at 5° incidence angle to the surface. Three different erosion strategies were studied: (i) erosion with stationary sample stage as well as erosion with a rotating sample stage where milling was performed within a sector of (ii) $\pm 15^\circ$ and (iii) $\pm 30^\circ$ around the direction perpendicular to the notch.

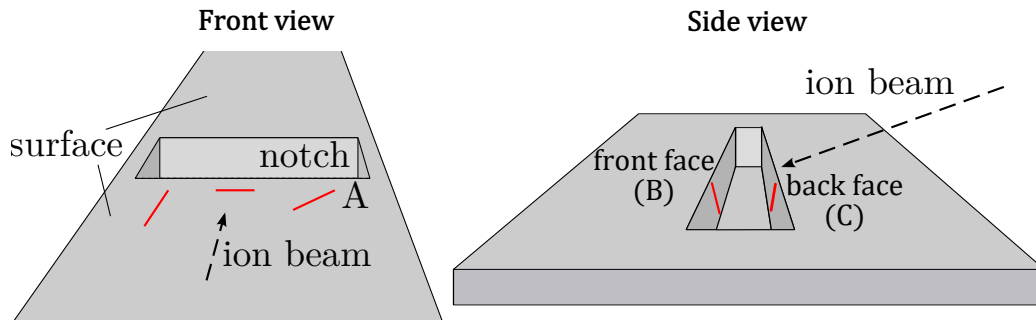


Figure 5.5: Illustration of the surface configurations used in this study. Grooves can be present on the initial surface (A) and the faces of the notch and be oriented either parallel, perpendicular or slanted relative to the incident broad ion beam. The notch face which is irradiated by the ion beam is denoted as front face (B), the opposing face as back face (C).

Groove milling was performed using line scan patterns at 7 nA ion current. SEM micrographs of the surface configuration prior to broad ion beam erosion are shown in Fig. 5.6A. The topography of the grooves was determined using white light interferometry (Fig. 5.6B), which exhibit a wedge shape of $1.3 \mu\text{m}$ width and $1.4 \mu\text{m}$ depth. Glancing-

5 Erosion of Surfaces With Initial Notches

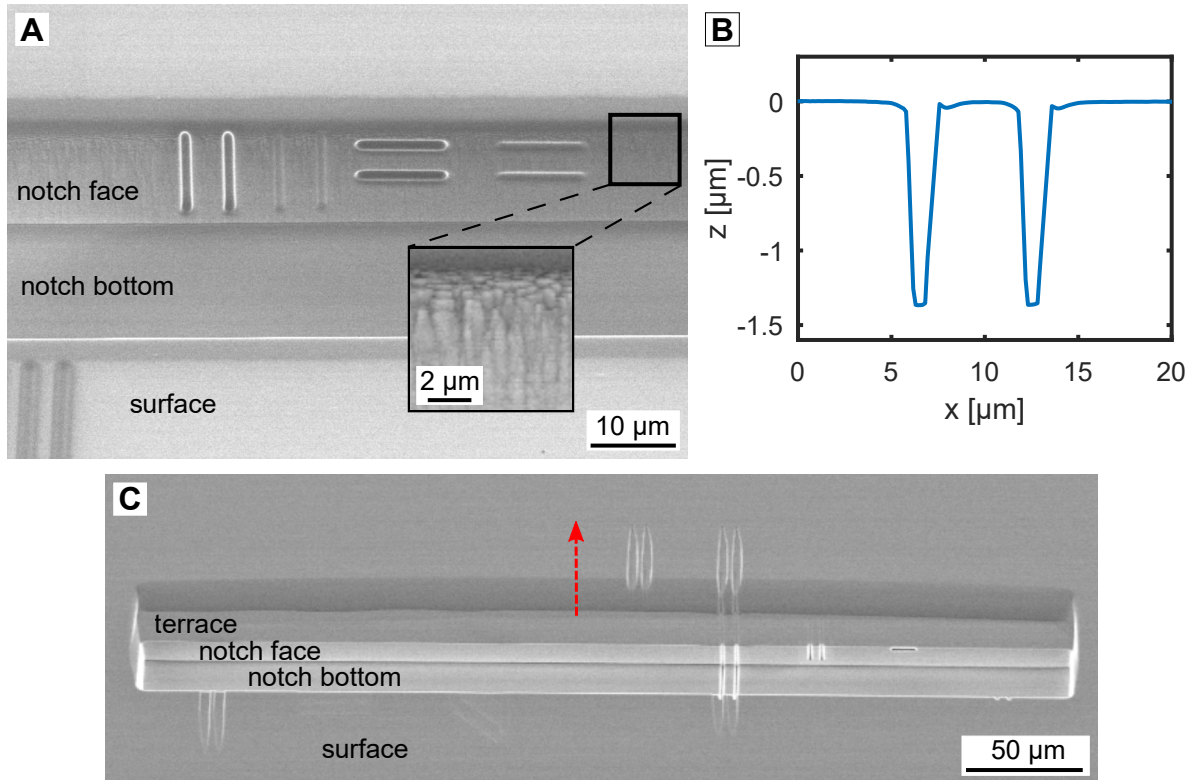


Figure 5.6: (A) SEM micrographs of a sample with a notch and additional FIB-milled grooves before broad ion beam erosion at 45° stage tilt, (B) surface profile across two grooves, measured with white light interferometry, and (C) SEM micrographs of a sample with a notch and additional FIB-milled grooves before broad ion beam erosion at 45° stage tilt. The projected ion beam incidence direction is indicated by the arrow.

angle broad ion beam erosion was performed at 5° with 4 keV Ar^+ -ions. Milling was stopped when the terrace reached a pre-defined length of ≈ 20 μm. An overview micrograph of a sample after broad ion beam erosion is shown in Fig. 5.6C.

Terrace regions unaffected by any grooves, i.e. sufficiently far away from them, show limited topography (Fig. 5.7) after broad ion beam erosion. In the case of stationary erosion, weak ripples with a wavefront perpendicular to the notch are present, stemming from slight curtaining artefacts on the notch. For oscillating erosion with 30° milling sector, the terrace exhibits some roughness in the form of faceted to wavy patterns, depending on the distance from the notch. For 15° milling sector, no topography formation is apparent.

5 Erosion of Surfaces With Initial Notches

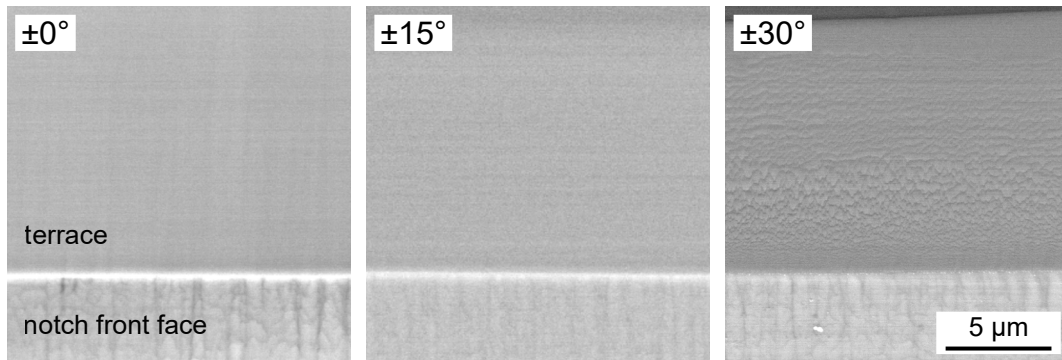


Figure 5.7: SEM micrographs of a sample with a notch after broad ion beam erosion (left: stationary milling, middle: $\pm 15^\circ$ milling sector, right: $\pm 30^\circ$ milling sector).

Grooves present on the initial surface affect stationary and oscillating erosion processes very differently (Fig. 5.8). Longitudinal ripples (Fig. 5.8A) are directly propagated along the ion beam incidence direction onto the terrace for stationary erosion, whereas no influence on the terrace topography was found for 30° sector milling. For 15° sector milling, no influence of the terrace roughness was found, however, the edge of the notch shows a slight bend. Notably, the grooves on the initial surface are widened for sector milling strategies and the width increases with sector size. Transversal grooves (Fig. 5.8B) lead to the formation of a further, receded surface level upon stationary erosion, which is then propagated onto the terrace. In this sense, they act like a miniature notch. In case of sector milling, the receded surface level caused by the grooves prior to the notch are less pronounced and cannot be traced anymore on the terrace. Slanted grooves (Fig. 5.8B) exhibit the same general behaviour as transversal grooves, leading to the formation of a receded surface level prior to the notch and propagating onto the terrace only in case of stationary erosion. There, two steps inclined at the same angle as the initial grooves are formed bounding the right side of the receded region.

SEM micrographs of the terrace regions affected by grooves on the notch faces are shown in Fig. 5.9. Longitudinal ripples on the front face are propagated onto the terrace for all erosion strategies (Fig. 5.9A). In contrast, no influence of the transversal grooves was found except temporarily when the edge of the terrace just hit the grooves. This is confirmed by noting that two transversal grooves were milled into the notch flank (c.f. Fig. 5.6A), of which the first is not present after erosion. Grooves on the notch back face on the other hand behave similar to notches on the initial surface, that is, they do

5 Erosion of Surfaces With Initial Notches

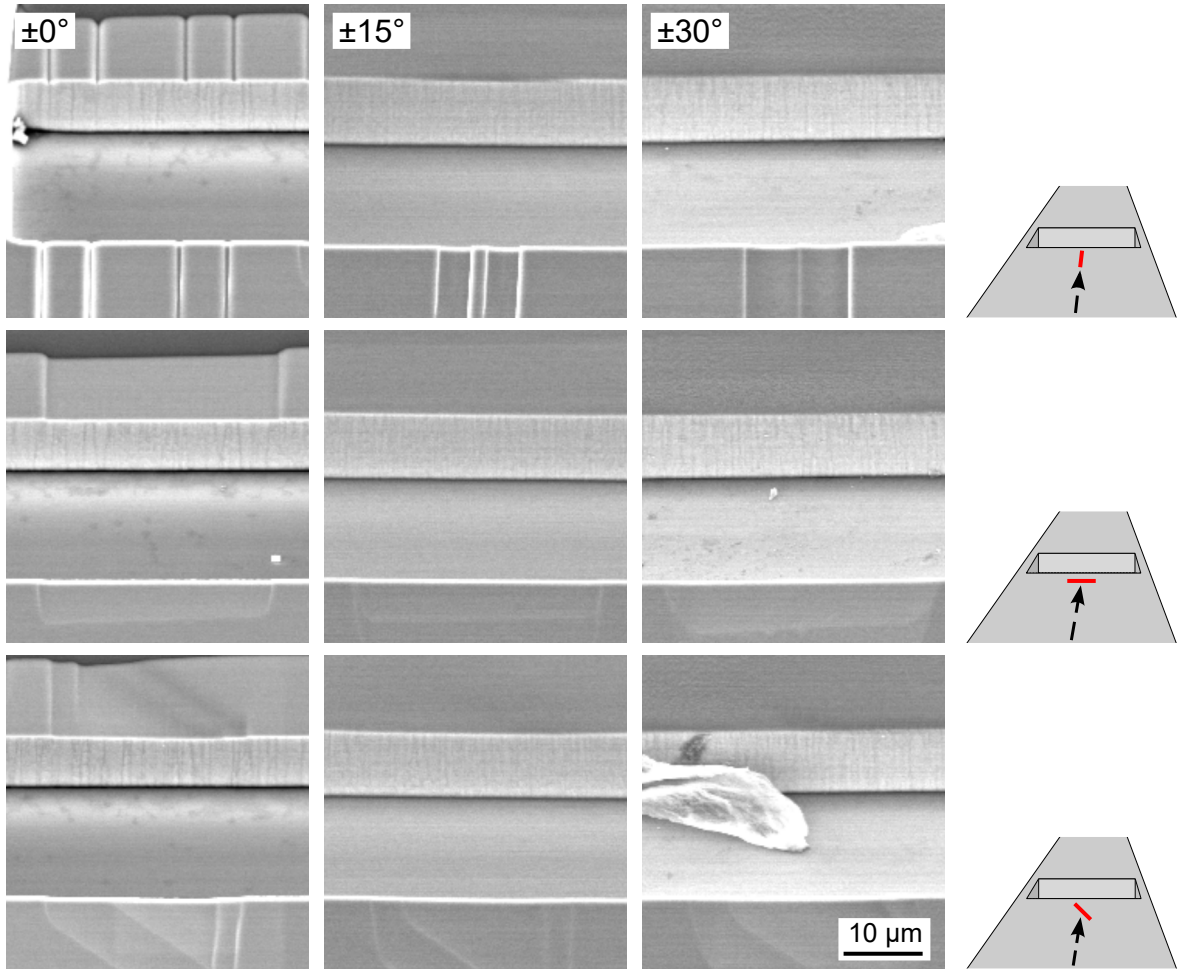


Figure 5.8: SEM micrographs of a sample with a notch and artificially created grooves on the surface after broad ion beam erosion. Columns from left to right: stationary milling, $\pm 15^\circ$ milling sector, $\pm 30^\circ$ milling sector; rows from top to bottom: parallel, perpendicular and slanted groove orientation w.r.t. the incident broad ion beam. The particle visible in the last panel stems from silver paint flushed onto the sample after removal from the broad ion beam device.

propagate onto the terrace in case of stationary erosion but are efficiently smoothed out for oscillating erosion.

5 Erosion of Surfaces With Initial Notches

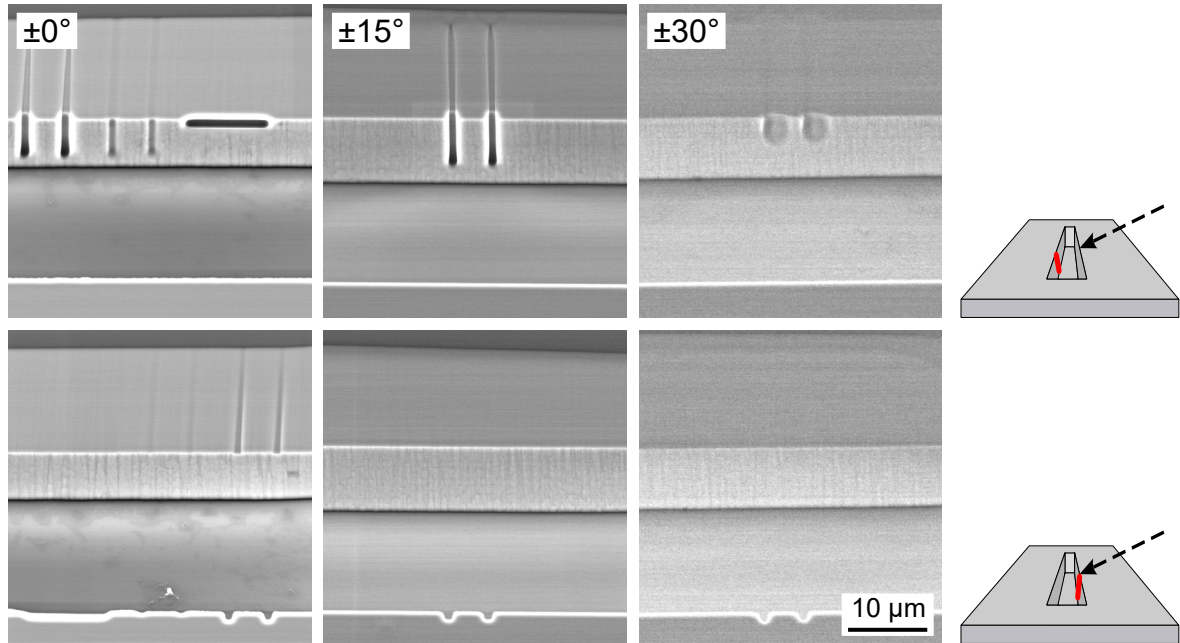


Figure 5.9: SEM micrographs of a sample with a notch and artificially created grooves on the notch faces after broad ion beam erosion. Columns from left to right: stationary milling, $\pm 15^\circ$ milling sector, $\pm 30^\circ$ milling sector; rows from top to bottom: grooves on notch front face and back face.

5.2.2 Ion Beam Induced Amorphization

The ion beam induced amorphization was studied using high resolution transmission electron microscopy. For this purpose, a notched Si surface was processed with broad ion beam erosion at 5° ion incidence angle and 4kV acceleration voltage for 45 min (Fig. 5.10A). After deposition of a protective Pt layer, a cross-sectional lamella has been prepared using Ga^+ focused ion beam milling, including in-situ sample lift-out (Fig. 5.10B, see also Giannuzzi *et al.* (2005)).

A high resolution TEM micrograph of the edge region at the end of the terrace is shown in Fig. 5.11. The micrograph exhibits four different regions: the crystalline Si bulk (1) is followed by an layer amorphized by the ion beam (2). The bright region in the micrograph (3) is caused by delamination of the Pt layer (4) due to the strong local topography. Delamination is not observed uniformly along the sample but only at some isolated positions. Furthermore, the amorphous layer (2) exhibits some contamination

5 Erosion of Surfaces With Initial Notches

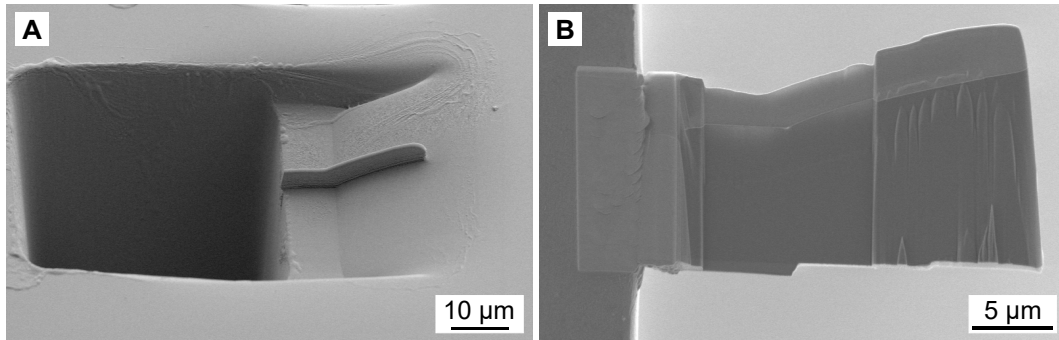


Figure 5.10: FIB preparation of a TEM lamella: sample after deposition of a protective Pt bar (A) and thinned lamella mounted on a sample holder (B).

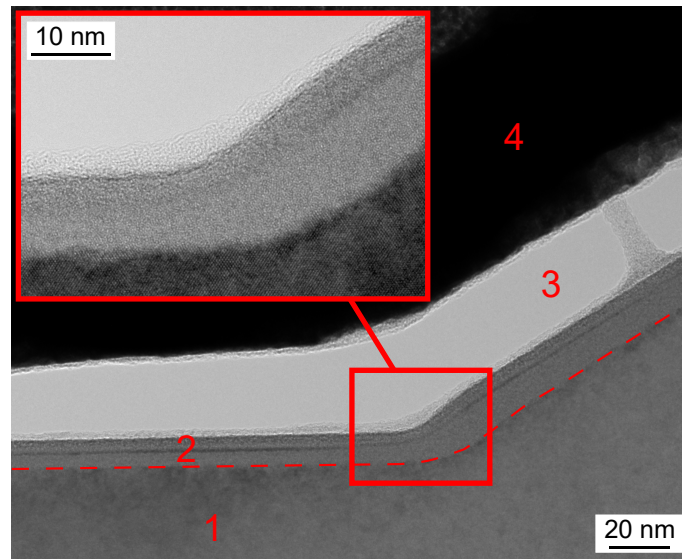


Figure 5.11: TEM micrograph of the edge. Four different regions are visible: (1) the crystalline Si bulk, (2) an amorphous surface region as a result of ion beam bombardment, (3) a region where delamination of the protective Pt-layer occurred and (4) the Pt-layer.

forming a thin line with slightly increased contrast, most likely stemming from Ga implantation during the FIB preparation. There is a smooth transition of the sample from flat terrace regions to the inclined regions without discernable kink or step. The local inclination angle of the sloped surface exhibits a maximum of approximately 40° relative to the terrace within 20 nm, then the curvature changes reverses and the inclination angle is steadily declining.

5 Erosion of Surfaces With Initial Notches

region	layer thickness [nm]	local inclination [°]
A	4.4 ± 0.3	0
B	9.4 ± 0.8	0
C	15.3 ± 0.9	40
D	8.9 ± 0.4	22

Table 5.2: Amorphization layer thickness and local inclination

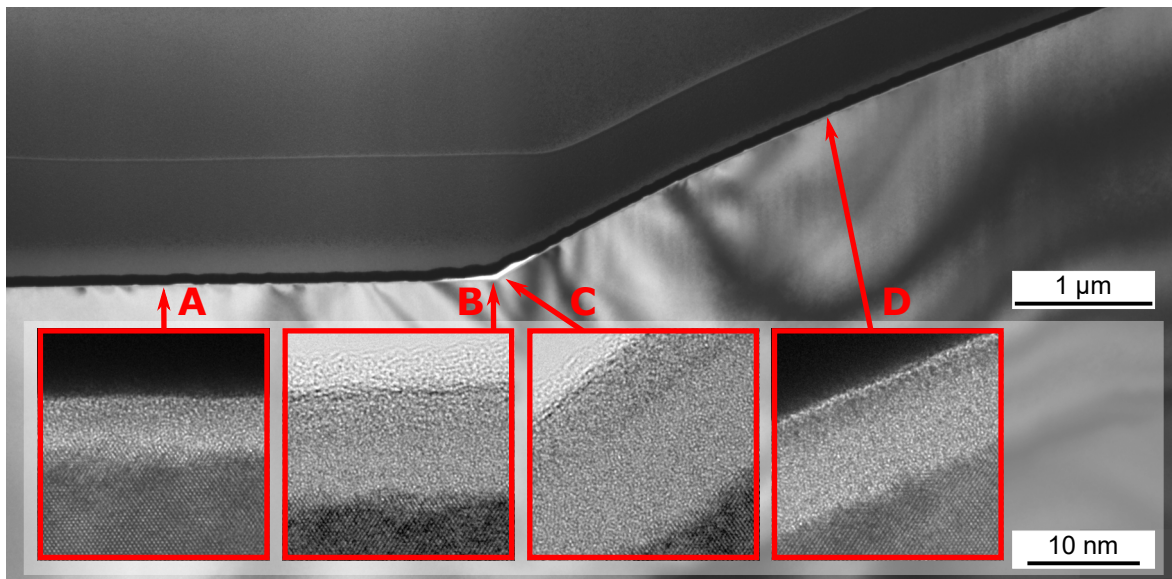


Figure 5.12: TEM micrograph of the whole sample and HR-TEM micrographs of the amorphization layer at different positions: (A) on the terrace 2.5 μm away from the edge, (B) the terrace region directly at the edge, (C) the inclined edge region and (D) the sloped region 2.5 μm away (horizontal distance) from the edge.

The thickness of the amorphous layer along the local surface normal direction was determined at several positions along the sample surface (Table 5.2): (A) on the terrace far away from the edge, (B) on the terrace right before the onset of the edge, (C) right after the onset of the edge and (D) on the inclined region further away from the edge. The lowest layer thickness of 4.4 nm was found in region (A), the largest value of 15.3 nm in region (C). Corresponding micrographs are shown in Fig. 5.12.

5.3 Evolution of Surface Geometry

In order to apply initial notches to sample preparation tasks, a sufficient understanding of the surface geometry is required. Typically, a particular sample feature of interest needs to be investigated, which requires the preparation of well-defined sample sections at a particular depth. Thus, boundary conditions arise on the size and depth of the terrace which is formed during erosion of a notched surface. Since terrace growth is occurring in parallel to erosion of the mean surface as a whole, a model linking the two is required, which is the focus of this section. The results discussed in this section have been published in reference Busch *et al.*, 2021a.

5.3.1 Linear Model

A linearized description of the surface is proposed here based on some simplifying assumptions. The initial surface is assumed to be homogeneous and flat and the incident ion beam is considered parallel as well as spatially and temporally homogeneous. The erosion depth of the mean, flat surface $d_0 \propto Y(\theta_{\text{ion}})J \cos \theta_{\text{ion}} t$ is then proportional to the projection of the ion beam current onto the surface $J \cos \theta_{\text{ion}}$, erosion duration t and sputtering yield $Y(\theta_{\text{ion}})$ (c.f. Section 3.1.2). On the other hand, the terrace length in the regime of stationary growth can be described by a linear function $l_{\text{ter}} = v_{\text{ter}} \cdot t + c$, where v_{ter} is the terrace growth speed and $\tau = -c/v_{\text{ter}}$ can be thought of as an induction time of terrace formation. By substituting the erosion duration t with the mean erosion depth d_0 , a purely geometrical description of the surface without explicit time dependence can then be obtained:

$$l_{\text{ter}} = \text{AR} \cdot d_0 + c^* \quad (5.1)$$

The coefficients of this linear relations can be thought of as an aspect ratio AR between terrace length and depth, and an induction depth $d_{\text{ind}} = -c^*/\text{AR}$ of the terrace, i.e., the erosion depth of the mean surface during the initial phase of terrace formation. In this way, not only the explicit dependence on erosion duration is eliminated, but also parameters such as ion current, material density and the absolute value of the sputtering yield Y (though not its angle dependence $Y(\theta)/Y(0^\circ)$).

An estimate for the steady-state parameters v_{ter} and AR can be obtained using a model of two intersecting surface segments with constant inclination which are subject to ion beam erosion (see Fig. 5.13 for a schematic depiction). In this model, each

5 Erosion of Surfaces With Initial Notches

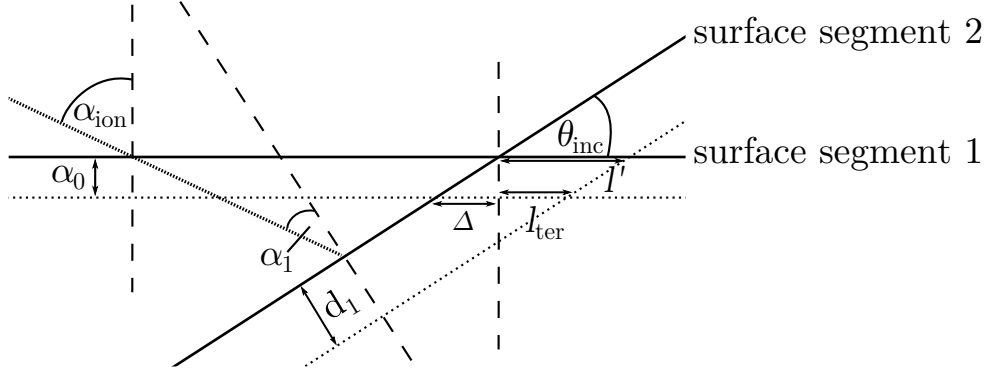


Figure 5.13: Model of two intersecting surface segments under ion beam erosion

surface segment is propagated separately along its surface normal, considering only the angle dependence of the sputtering yield. By appropriate choice of constants ($Y(0^\circ)$, J , etc.), the erosion depth of each segment can be set to $d_0 = Y(\alpha_{\text{ion}}) \cos \alpha_{\text{ion}}$ and $d_1 = Y(\alpha_1) \cos \alpha_1$. Analyzing the movement of the intersection point of both surface segments, estimates for the steady-state parameters can be derived. The terrace growth speed is proportional to the terrace length change, $v_{\text{ter}} \propto l_{\text{ter}}$, and the aspect ratio is given by $\text{AR} = l_{\text{ter}}/d_0$. The following geometric relations hold:

$$\begin{aligned} \alpha_1 &= |90^\circ - (\theta_{\text{ion}} + \theta_{\text{inc}})| \\ l' &= \frac{d_1}{\sin \theta_{\text{inc}}} \\ v_{\text{ter}}(\theta_{\text{inc}}) \propto l_{\text{ter}} &= l' - \Delta = \frac{Y(\alpha_1) \cos \alpha_1}{\sin \theta_{\text{inc}}} - Y(90^\circ - \theta_{\text{ion}}) \sin \theta_{\text{ion}} \cot \theta_{\text{inc}} \end{aligned} \quad (5.2)$$

$$\text{AR}(\theta_{\text{inc}}) = \frac{l_{\text{ter}}}{d_0} = \frac{Y(\alpha_1) \cos \alpha_1}{\sin \theta_{\text{inc}} Y(90^\circ - \theta_{\text{ion}}) \sin \theta_{\text{ion}}} - \cot \theta_{\text{inc}} \quad (5.3)$$

If the inclination angle of the surface θ_{inc} is known, the steady-state terrace growth speed and aspect ratio can directly be calculated from Eqs. (5.2) and (5.3). While the relation between surface inclination and the experimental parameters has not been established yet, an upper estimate can be derived by taking the maximum over all possible angles, i.e. $\text{AR}_{\text{max}} = \max_{\theta \in [0, 90^\circ]} \text{AR}(\theta_{\text{inc}})$ (and accordingly for $v_{\text{ter, max}}$). In Fig. 5.14, v_{ter} has been calculated using the analytical expression Eq. (3.5) for the sputtering yield of silicon.

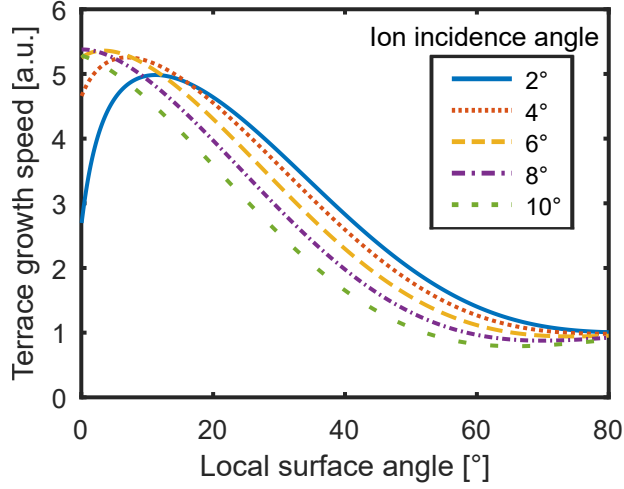


Figure 5.14: Terrace growth speed as function of surface inclination angle θ_{inc} , as calculated from Eq. (5.2) for Si.

5.3.2 Simulations

Simulations of the terrace formation process were performed based on the algorithm discussed in Section 3.1.3 for ion incidence angles from 2° to 10° and notch widths between $10\ \mu\text{m}$ and $50\ \mu\text{m}$. From the obtained terrace length curves, terrace growth speed, aspect ratio, and induction time / induction depth were determined by linear regression.

The simulated dependence of terrace growth speed and aspect ratio on ion incidence angle and notch width is shown in Fig. 5.15 and compared to the theoretical estimates discussed in the previous section. Terrace growth speeds exhibits a moderate dependence on both ion incidence angle and notch width, with a maximum between 3° and 5° for any given notch width. For constant ion incidence angle, the terrace growth speed is larger for narrower notches. At 3° or lower, the growth speed becomes independent of notch width. The relative change in growth speed $(v_{\text{ter,max}} - v_{\text{ter,min}})/v_{\text{ter,max}}$ within the given parameter field is approximately 25%. The theoretical upper bound estimates are able to reproduce the simulated terrace growth speed relatively well, although predicting the maximum value at a higher angle of $\approx 8^\circ$. A very pronounced dependence on ion incidence angle can be observed for the aspect ratio. At grazing ion incidence, the erosion of the mean surface vanishes, whereas the terrace growth speed only moderately declines. Thus, the aspect ratio is diverging for $\theta_{\text{ion}} \rightarrow 0$. At higher incidence angles from 7° to

5 Erosion of Surfaces With Initial Notches

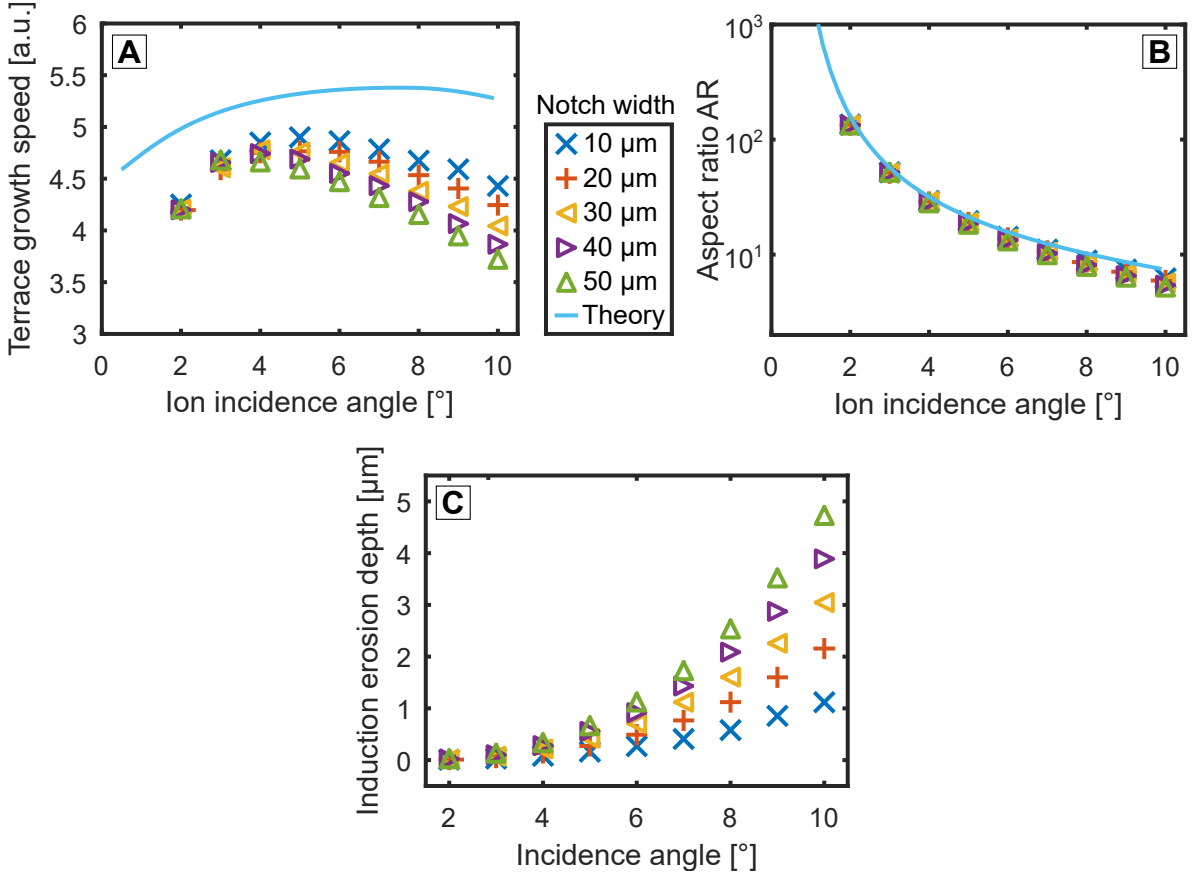


Figure 5.15: Simulated terrace growth velocity v_{ter} in arbitrary units (A) and aspect ratio (B) as well as corresponding theoretical estimates based on Eq. (5.2) and Eq. (5.3). (C) Simulated induction depth d_{ind} as function of ion incidence angle.

10 $^\circ$, the aspect ratio has values of the order of 10, implying the terrace size will grow by $\approx 10 \mu\text{m}$ during a erosion of the mean surface by 1 μm . The theoretical estimate again provides a very accurate upper bound for the aspect ratio.

The induction depth d_{ind} is shown in Fig. 5.15C for different ion incidence angles and notch widths. The induction depth takes values between 0 μm and 5 μm within the given parameter field, implying that the mean surface is eroded up to 5 μm during the initial phase of terrace formation until notable terrace growth occurs. For any given notch width, the induction depth grows monotonously with ion incidence angle and is mostly negligible at the lower end of the parameter field, i.e. for 2 $^\circ$ and lower. On the other

hand, the induction depth exhibits close to linear dependence on notch width for any fixed ion incidence angle.

5.3.3 Experimental Results

Erosion experiments were performed on notched Si surfaces for different ion incidence angles. On each sample, three notches with different widths were milled in closed proximity in order to limit the influence of the ion beam profile. Each surface was partially covered with carbon tape during erosion in order to preserve a reference level for topography measurements. For each ion incidence angle, four samples with different erosion durations (and correspondingly, different erosion depth of the mean surface) were produced. From these samples, terrace growth - erosion depth curves were determined (Fig. 5.16A) and the terrace aspect ratio and induction depth calculated by linear regression. Since notches with a finite aspect ratio do not possess a constant notch width during erosion but 'shrink', the mean of the current notch widths over all milling durations is given for each different notch geometry in these diagrams. In Fig. 5.16B, the relative terrace depth (the difference in depth level between the terrace region and the mean surface level) is also shown. In congruence with earlier results (Busch *et al.*, 2018), the relative terrace depth is systematically and non-randomly increased compared to theoretical predictions as a result of beam divergence. This discrepancy acts like an effective shift of the incidence angle between approximately 2° and 4° in the range between $\theta_{\text{ion}} = 2^\circ$ to 4° .

The aspect ratio data, shown in Fig. 5.17A, exhibits good qualitative agreement with theoretical estimates and simulation results. As predicted, the aspect ratio substantially increases towards grazing incidence. However, quantitative agreement is not achieved, as the aspect ratio value determined at 2° for example differs from simulation results by between 30% and 50%. The aspect ratio at $\theta_{\text{ion}} = 2^\circ$ shows an increase in width notch width, in contrast to simulation results. However, all three data points are roughly within the uncertainty range of the regression analysis.

The induction depth data follows the broad trends predicted by the simulations at ion incidence angles of 2° and 5° . At $\theta_{\text{ion}} = 2^\circ$, the induction depth is close to zero, as predicted by simulations. At 5° incidence angle, the experimentally determined induction depth is larger than simulations suggest by a factor of two. Pronounced deviations from these trends occur at 8° , where too low induction depth occur. In particular, the negative value at 8° ion incidence angle and $9\mu\text{m}$ seems to indicate the breakdown of the linear

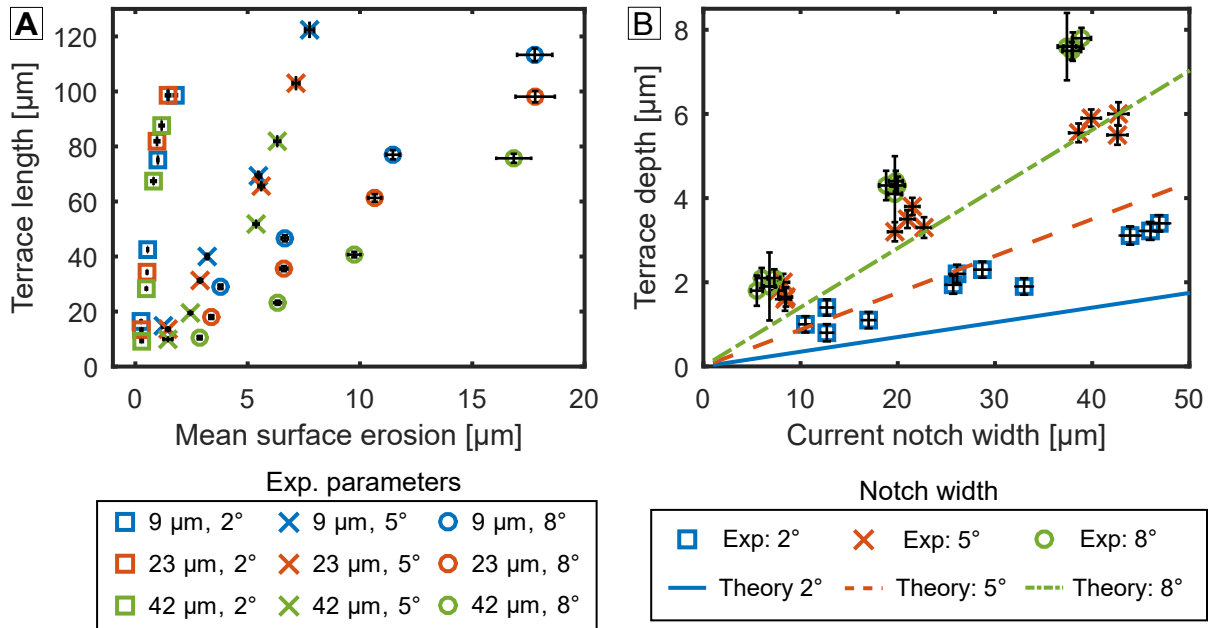


Figure 5.16: Mean erosion depth - terrace length data for different experiment geometries (A) as well as terrace depth difference to the mean surface as function of experiment geometry (B).

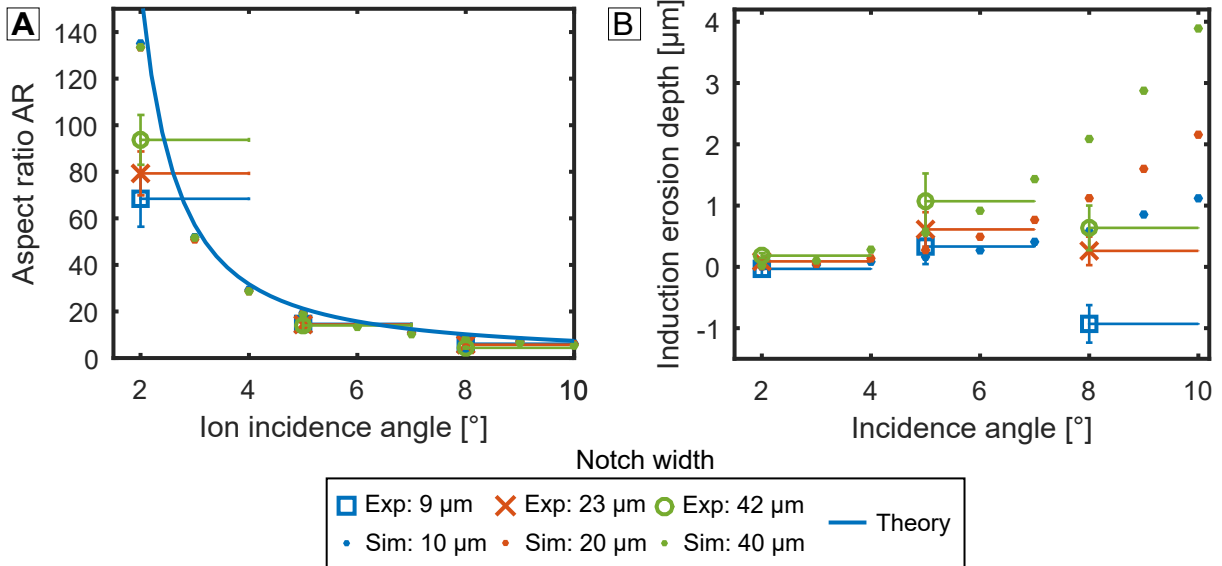


Figure 5.17: Experimental data for aspect ratio (A) as well as induction depth (B). The data are labelled by the mean notch width over all surface erosion state of notches with equal initial geometry. The asymmetric, horizontal bar for the incidence angle is indicating an effective angle shift based on the observed systematic deviations in Fig. 5.16B between theoretical and experimental terrace depth.

model's validity due to notch shrinking and beam profile effects.

The systematic shift in effective incidence angle due to beam divergence is indicated by the horizontal bars in Fig. 5.17. Taking these systematic shifts into account, a reasonably good match between experiment to simulations and analytic estimates can be stated.

5.4 Discussion

5.4.1 Sample Processing

Notches with smooth faces can be readily prepared on polished Si surfaces using high-current plasma FIB milling. Furthermore, upon glancing-angle broad ion beam erosion of these samples, highly smooth terraces are created devoid of any discernable preparation artefacts. In this respect, notch cutting with Xe^+ -plasma FIB exhibits vastly improved potential for preparation of high-quality specimen compared to the approach employed in Busch *et al.* (2018) based on ablation with a ps-pulsed laser. When curtaining artefacts were observed on rough Si substrates, they could be removed by applying additional polishing steps at successively lower ion beam currents.

Significant topography formation on the notch faces occurs as a result of charge build-up and eventual sudden discharging on insulating glass samples. Smooth notches can still be created via extensive polishing at low ion beam currents at the cost of increased preparation time. While usage of a flood gun proved insufficient for charge compensation due to the high inclination of the notch faces, alternative approaches could help at least partially alleviate this problem. For example, Stokes *et al.* (2007) proposed a charge compensation scheme using the primary electron beam in a dual beam FIB-SEM instruments. Another approach could be localized gas injection using a nozzle (Deerinck *et al.*, 2018).

Ablation with fs-pulsed laser ablation is not as capable as PFIB milling of creating smooth notches on Si. Still, compared to the lasers with ps- or ns-scale pulse duration used in Busch *et al.* (2018), a reduced degree of notch face ripple formation, waviness or faceting is observed. Substantial debris redeposition was observed, which could only partially be removed using a CO_2 snow-jet. If the remaining debris should prove problematic for the desired application, an ion milling pre polishing step could be employed, preferably using a rotating specimen stage to avoid introducing shadowing artefacts or preferential erosion. On glass specimens, notches with reduced roughness or ripple formation can be

5 Erosion of Surfaces With Initial Notches

milled using fs-pulsed laser ablation rather than PFIB. The aspect ratio of the notches is reduced in this case, however. Given its orders-of-magnitude higher material removal rates, laser ablation could thus be very advantageous if the demands on notch shape accuracy are not too strict.

Glancing angle erosion experiments using broad ion beams revealed that the demands on notch quality seem to be less stringent for glass samples than for silicon samples. Preparation of terraces with little roughness was possible using glancing-angle BIB even for notches with pronounced topography (single milling step at high current). Considering the experiments with artificially milled ripples on the notch faces, the nature of the notch face topography could be the relevant factor. However, given that the notch face features were observed to change with increasing distance from the surface (see Fig. 5.1C), one would expect this change to be reflected in the terrace topography, which was not the case. Hence, it seems more plausible that the smoothing is related to the physics of erosion on an insulating sample. One possible explanation here is that surface charging under the (locally) nearly homogeneous irradiation with the broad beam leads to an enhancement of gradient dependent smoothing. This could be the case if the electric fields in quasi-stationary conditions lead to a deflection of incoming ions towards local protrusions and away from local surface depressions.

As an alternative approach, glancing-angle erosion of notched surfaces with a focused ion beam is possible. The preliminary results achieved on Si are very promising. Smooth terrace surfaces can be readily created, although some degree of ripple formation was occasionally observed. These ripples are likely an artefact of the beam scanning, which could potentially be enhanced in several ways. One approach could be to create an optimized quasi-broad ion milling scheme by combining a moderate spot overlap, low dwell times, and possibly beam defocusing. Due to the high sample inclination, both spot spacing along the ion beam direction and the focus length need to be (dynamically) corrected for. It could also be possible to use advanced scanning regimes where beam spacing is far larger than the beam diameter, but successive scan frames are shifted relative to each other. Such a regime could be useful if the amount of material removed in a single frame provides too large a deviation from quasi-broad irradiation conditions when using an overlapping spot spacing.

Several potential advantages exist when performing terrace formation via glancing-angle erosion in a FIB. First, both basic processes (i.e. notch cutting and glancing-angle

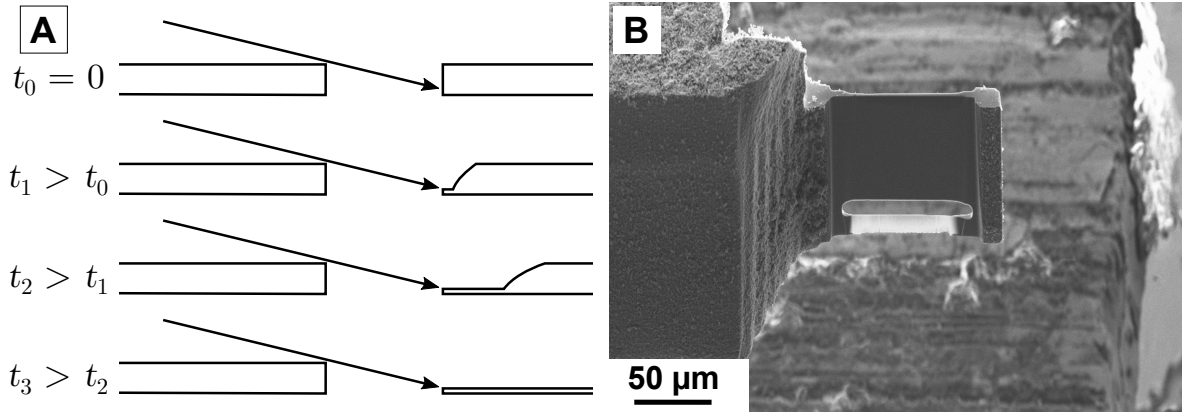


Figure 5.18: Schematic depiction of TEM lamella thinning using initial notches (A) and SEM micrograph of a thinned lamella (B).

erosion) can be performed in a single instrument. Second, it could be used for slicing the surface of a bulk sample without performing any prior sample excavation and lift-out. Such an approach could also be useful if a sample feature in a defined depth need to be excavated in a FIB-SEM experiment but top-down milling is undesirable due to the presence of differential erosion in inhomogeneous materials. Third, glancing-angle FIB erosion of a notched, thin lamella could be useful for the preparation of electron-transparent specimen for TEM analyses. A similar lamella geometry as in Busch *et al.* (2018) could be used, only replacing the broad ion beam erosion step with a focused one (Fig. 5.18). In conventional FIB preparation approaches, lamella thickness is controlled by performing the final polishing steps at high spatial resolution and progressively lower currents (Cooper & Ben Assayag, 2013). Because of the self-masking mechanism inherent to the concept of initial notches, erosion at much higher currents in a quasi-broad ion beam setting could instead be performed until the onset of perforation in the terrace region, similar to the approach used in glancing-angle BIB polishers (Busch *et al.*, 2023). By widening the notch slightly at defined positions, it would even be possible to control where perforation occurs first. This way, indicator regions could be created on the sample which could help with thickness control. Alternatively, the method could be combined with quantitative measurements of lamella thickness (Salzer *et al.*, 2009; Conlan *et al.*, 2020) in order to define a stop criterion for the polishing process. As a further advantage, mechanical stability of the sample can be increased as the lamella is stabilized by the thicker

region in front of the notch.

In the case of insulating materials, glancing-angle focused ion beam erosion is less useful for terrace creation, as significant roughness is introduced to the terrace as a result of charge build-up. The cursory studies performed so far provide little confidence that an optimization of scan and milling parameters can fully alleviate this problem. Future research could clarify if different charge neutralisation schemes are beneficial here, as already discussed. Hence, broad ion beam erosion appears to be advantageous for preparing non-conducting specimens. The differences in milling behaviour between broad and focused ion beams can be explained by two factors. First, upon broad ion beam erosion, a stationary charge distribution is ultimately reached, whereas the charge distribution is explicitly time-dependent due to the scanning of the beam during FIB milling. Second, broad ion beams can contain a significant amount of fast neutrals which contribute to sputtering but are insensitive to sample charging (Harper *et al.*, 1982).

5.4.2 Sample Quality

Terrace roughness

In order to prepare highest-quality samples, formation of both surface roughness and beam-induced microstructure changes needs to be efficiently suppressed. The findings in this thesis clearly demonstrate that the topography both of the initial surface and the notch faces can affect terrace roughness, in particular for non-conducting specimens. On silicon, direct geometric relations between incident broad ion beam, initial sample topography and resulting terrace topography were found in erosion setups with fixed sample stage. As a general trend, features on the initial surface tend to get preserved in the terrace region, in the sense that no additional smoothing mechanisms are active. Ripples aligned parallel to the ion beam (ripple normal parallel to the notch) were shown to be of particular relevance, since they are propagated onto the terrace and can significantly degrade terrace roughness. In contrast, ripples on the initial surface within the region where the terrace is to be formed do not contribute to final terrace roughness. Transversal ripples on the other hand, which behave like miniature notches and lead to the formation of an indented plateau, might be less harmful for subsequent investigations. A deliberate choice of notch orientation relative to pre-existing surface topography should thus be made in order to reduce terrace roughness.

Ripples on the notch faces can also affect terrace roughness. Notably, this holds for

5 Erosion of Surfaces With Initial Notches

both faces of the notch, the one on the terrace side and the opposite one. There is a correspondence in the impact on terrace roughness between longitudinal ripples on the initial surface and ripples on the notch face which are perpendicular to the ion beam and similarly, also between transversal ripples on the initial surface and ripples on the notch faces which are parallel to the surface.

Using an oscillating erosion scheme, a decoupling of terrace topography from initial surface topography is observed. Both features on the initial surface and the back notch face (on the entry side of the ion beam) are effectively smoothed out and do hardly contribute to terrace roughness. This observation suggests that the non-local nature of the erosion process across the notch plays a significant role in determining terrace roughness.

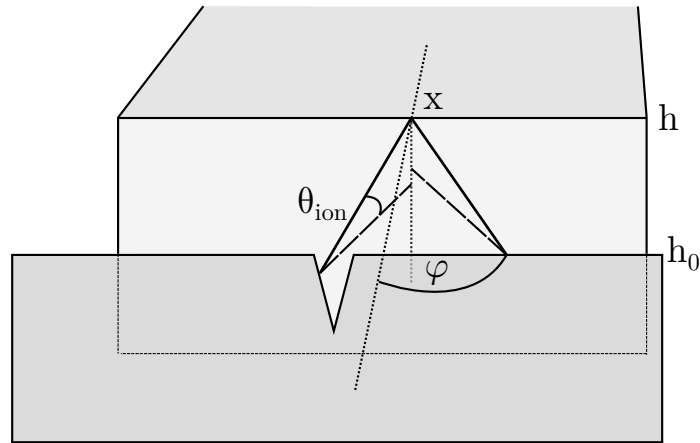


Figure 5.19: Model of the milling process as a mask projection with mask height profile h_0 .

As a simple way to conceptualize this non-locality, consider the propagation of surface features onto the terrace as a case of mask projection (see sketch in Fig. 5.19). In this case, the surface prior to the notch plays the role of the mask, which we assume to be infinitely thin for the sake of simplicity. Let $h_0(x)$ be the mask profile. Then, for any given stage position φ relative to the mean incidence direction and lateral position x , the

5 Erosion of Surfaces With Initial Notches

notch face is irradiated with ions above a height $h_{\text{ter}}(x, \varphi)$. The following relations hold:

$$h(x, \varphi) = h_0(x, \varphi) - \Delta h(x, \varphi) \quad (5.4)$$

$$h_0(x, \varphi) = h_0(x + \tan \varphi \cdot w_{\text{notch}}) \quad (5.5)$$

$$\Delta h(x, \varphi) = \tan \theta_{\text{ion}} \cdot w_{\text{eff}} = \tan \theta_{\text{ion}} w_{\text{N}} / \cos \varphi \quad (5.6)$$

As a first approximation to the actual terrace depth, the mean height $\overline{h_{\text{ter}}(x)}$ of the irradiated region over a milling cycle can be considered. For constant rotation speed, this is given by

$$\overline{h_{\text{ter}}(x)} = \frac{1}{2\varphi_{\text{max}}} \int_{-\varphi_{\text{max}}}^{\varphi_{\text{max}}} h(x, \varphi) d\varphi. \quad (5.7)$$

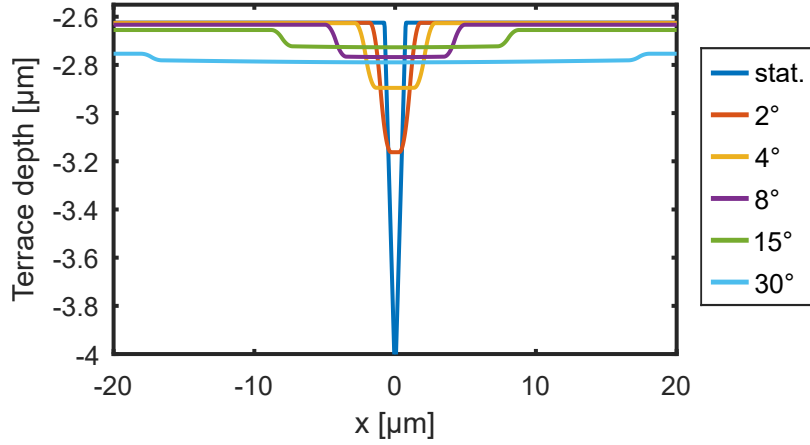


Figure 5.20: Approximation of terrace depth, calculated by numerical integration of Eq. (5.7), for an ion incidence angle of 5° , a notch width of $30 \mu\text{m}$ and several different maximum milling sector angles.

A numerical integration of Eq. (5.7) with a V-shaped ripple profile of $1.5 \mu\text{m}$ depth and width centered at the origin is displayed in Fig. 5.20. A notch size of $30 \mu\text{m}$ and milling sector sizes between 0° (static stage) and $\pm 30^\circ$ were chosen. According to this model, a ripple on the initial surface is hence projected over larger and larger areas with increasing milling sector size, which results in an effective smoothing. As apparent from Eqs. (5.4) to (5.6), this behaviour is independent on the ion incidence angle θ_{ion} , which only affects the discrete depth step occurring at the notch. Importantly, this smoothing by self-masking and projection is fundamentally different from all the mechanisms discussed in

5 Erosion of Surfaces With Initial Notches

Section 3.1.1 such as gradient-dependent smoothing, diffusion or viscous flow, which all act locally.

The only surface features significantly affecting terrace roughness under oscillating ion beam erosion are ripples on the terrace-sided notch face. In their case, no non-local smoothing mechanism is at play. Furthermore, when comparing the ripples on the terrace after oscillating erosion in Fig. 5.9A to the ripples on the initial surface after oscillating erosion in Fig. 5.8A, it is striking that local smoothing is also prevented. While the ripples on the initial surface are subject to erosion, ripples on the notch face are masked and thus protected from erosion. Thus, they cannot be progressively smoothed, but are rather propagated onto the terrace in a stationary way.

While efficient surface smoothing could be demonstrated with a milling sector of $\pm 15^\circ$, the existence of a roughening mechanism not linked to any pre-existing topographic feature on the initial surface was observed at $\pm 30^\circ$. This mechanism results in the formation of wavy surface patterns on the terrace. Three possible mechanisms could be acting here. First, the erosion depth from the initial surface varies during a single milling cycle according to Eqs. (5.4) to (5.6). As a consequence, inhomogeneous and partial irradiation of the terrace occurs, at least in the regions close to the notch. In turn, this could lead to a directional faceting of the terrace. The condition for such a roughening mechanism would then be that the material removal during a single milling cycle is large enough to prevent an effective averaging to take place between cycles. Hence, a combination of ion current, ion energy, milling sector size and rotation speed could define the parameter domain of roughening. Second, scattering of incident ions at the side faces of the notch onto the terrace could cause an additional ion flux with locally altered incident angle, which could potentially cause roughening. Such scattering effects were regularly observed during erosion experiments in this thesis, as can be deduced from the formation of small wedges (c.f. Fig. 5.21) on both sides at the end of the terrace. Since the observed roughening occurred along the whole terrace width and was not restricted to some limited domain at both sides of the terrace, this effect seems less plausible in this context, though. Third, sputtering and redeposition of material from the inclined region at the end of the terrace as well as from the side faces of the notch could contribute another directed flux of target atoms onto the terrace. Similar directional roughening effects have been observed in Macko *et al.* (2011) in erosion experiments where Fe-codeposition from a target behind the sample was facilitated. It is possible that such an effect could also be achieved in case of self-codeposition here.

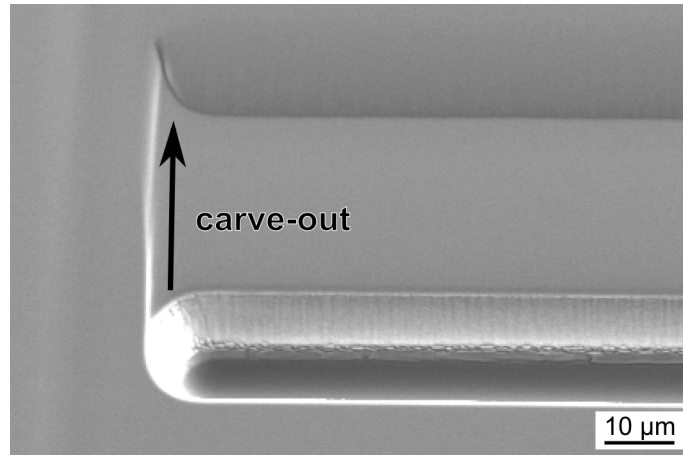


Figure 5.21: Scattering of ions at the sides of the terrace region leads to the formation of carve-outs.

Taken together, all these observations imply that oscillating glancing-angle erosion is generally preferable to static erosion when preparing samples with good conductivity. A polishing sector of $\pm 15^\circ$ is suitable for efficiently removing roughness present on the initial surface, based on self-masking and non-localized smoothing. In this case, only the terrace-sided notch face needs to be polished and devoid of curtaining artefacts. The experiments on terrace roughness discussed here were performed with idealized surface features. Yet, the implications derived should be relevant in broader contexts, as many rough surfaces can effectively be treated as a sequence of ripples or grooves.

Amorphization

Variation of amorphization layer thickness along the terrace was observed, which shall be compared to available literature data. A variety of studies has investigated amorphization of Si under Ar^+ bombardment and its dependence on ion incidence angle and energy (Schuhrke *et al.*, 1992; Barna *et al.*, 1998, 1999; McCaffrey *et al.*, 2001). A close to linear relation holds with respect to ion energy in the single digit keV-range, although there is some scatter in the available experimental data between studies. Similarly, at not too low angles in the range of 5° and 35° , the amorphization layer thickness increases linearly with incidence angle (Barna *et al.*, 1998). These trends are supported by theoretical considerations based on linear transport theory and the Schuhrke-Winterbon approach

5 Erosion of Surfaces With Initial Notches

(Schuhrke *et al.*, 1992) and simulations (Barna *et al.*, 1998; McCaffrey *et al.*, 2001) using SRIM code (Ziegler *et al.*, 2010).

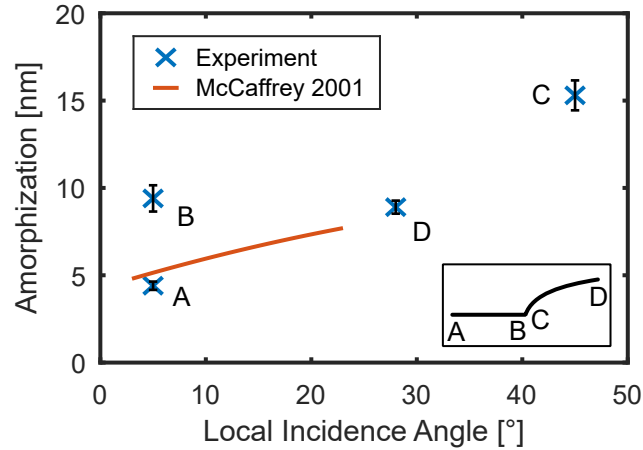


Figure 5.22: Thickness of amorphization layer (cf. Table 5.2) in the terrace region, on the terrace directly at edge, directly behind the edge and on the sloped region away from the edge as a function of local incidence angle, compared to data extrapolated from McCaffrey *et al.* (2001).

The measured amorphization layer thickness is shown in Fig. 5.22 as a function of local incidence angle $\theta_{\text{inc}} = \theta_{\text{loc}} + \theta_{\text{ion}}$ (θ_{loc} is the local surface inclination angle) alongside a spline interpolation of the experimental data from McCaffrey *et al.* (2001). The regions far away from the edge at the end of the terrace (A and D) agree very well with the reference data, whereas the regions at the edge (B, C) exhibit increased amorphization. This implies that the influence of the edge is spatially restricted to a small region within a distance of $\lesssim 1 \mu\text{m}$. Sufficiently far away from the edge, the erosion of the terrace region generally proceeds similar to erosion of a flat surface. Scattering of incident ions from the flat surface at B onto the curved slope at C and vice versa could lead to an additional local flux of ions with an increased incidence angle, thus causing such an increase in amorphization. Another possible cause of increased amorphization could be redeposition of sputtered material.

In terms of sample quality, the observed increases in amorphization should be negligible, since they are confined to a small region around the edge. Furthermore, additional polishing steps at smaller ion energies could be applied to reduce amorphization. Therefore, sample preparation using initial notches provides essentially comparable performance as

conventional broad ion beam polishing with respect to amorphization.

5.4.3 Kinetic Model of Surface Evolution

The evolution of sample geometry is reasonably well-described in terms of a linear model with the parameters aspect ratio and induction depth, despite the substantial simplifying assumptions involved. This model is a purely geometrical one, i.e., it is not explicitly time-dependent. Simulation results provide valuable insights into the dependencies of both parameters on experimental conditions, in particular notch width and ion incidence angle. Of these, the ion incidence angle is the primary factor controlling the magnitude of both aspect ratio and induction depth. For any fixed ion incidence angle, both quantities exhibit a linear dependence on notch width. More precisely, induction depth does even exhibit proportionality to notch width, whereas only a small correction term is provided in the case of aspect ratio. In contrast to aspect ratio, terrace growth speed (in the time-dependent parametrization) is only weakly dependent on experimental parameters. Hence, the divergence of the aspect ratio at gracing incidence ($\theta_{\text{ion}} \rightarrow 0^\circ$) is a direct consequence of the vanishing of the mean surface erosion.

A theoretical upper-bound steady-state estimate of both terrace growth speed and aspect ratio was given, which showed good agreement with the simulation results. This estimate provides a reasonable first approximation for most experimental situations and requires only knowledge of the angle dependence of the sputtering yield. Considering the steady-state shape in the derivation of the estimate will likely improve the prediction's accuracy. Notably, predictions for the induction depth are not possible within a steady-state framework and require a treatment of the full evolution equations.

Experimental results showed good qualitative agreement with both the theoretical estimate and the simulation data. However, an overall weaker angle dependence for the aspect ratio parameter was found. The induction depth data is somewhat inconclusive: while the overall magnitude is correct and the data shows the predicted dependence on notch width at 2° and 5° , the validity of the model appears to break down at 8° .

There are several possible sources of deviation between simulation and experiment. For example, the role of *beam divergence* should be noted. A divergent beam contains a fraction of ions with increased incidence angle relative to the surface. Hence, a shift of all data towards higher angles occurs. *Beam alignment* errors both relative to the sample surface (vertical) and relative to the normal direction of the notch (horizontal)

5 Erosion of Surfaces With Initial Notches

could have a similar effect. Notably, in-plane alignment errors away from perpendicular incidence always increase the depth at which ions hit the notch face, thus constituting an error type of non-zero mean. These kinds of systematic shifts of the discrete depth steps were observed both in Busch *et al.* (2018) and in this thesis. An effective ion incidence angle θ_{eff} with an correction term ϵ_{θ} could be introduced to compensate for these systematic shifts, $\theta_{\text{eff}} = \theta_{\text{ion}} + \epsilon_{\theta}$.

The finite size of the ion beam and the *beam profile* could also play a role, as they can cause a variation in ion current along the sample. Consequently, changes in local surface inclination will occur with increasing erosion duration, which alters the local material removal rates. These beam profile effects tend to increase with ion incidence angle and erosion duration. The assumption of *perpendicular notches* is also not perfectly satisfied in experiments. Deviations will be most pronounced at smallest notch widths due to the limited aspect ratio of the milling techniques. A finite aspect ratio should be more relevant at higher ion incidence angles, since the terrace will be formed at an increased depth - thus, the difference in effective notch width between surface and terrace level will be larger. Furthermore, notch shrinking increases with the erosion of the mean surface, which is also larger at higher incidence angles.

The anomalous behaviour of the experimental induction depth at the largest ion incidence angle likely relates to these effects. As is apparent by its high relative uncertainty, (cf. Fig. 5.17B), the induction depth obtained via linear regression is more sensitive to deviations from the predicted linear functional dependence than the aspect ratio. The range of validity for the linear model is limited from above (with respect to mean surface erosion depth) by beam profile related deviations from planar sample geometry and by the limited aspect ratio of the notch. However, it is also restricted from below by the induction phase of terrace formation itself, which does not yet follow steady-state kinetics. As the simulation results predict longer induction depths at larger angles (meaning a larger erosion period has to occur before the steady-state growth regime is reached), it is evident that the range of validity is narrower for larger ion incidence angles .

Finally, deviations can be caused by an insufficient treatment of material removal. As discussed in the preceding subsection, *ion scattering* can lead to locally increased ion fluxes, which could affect terrace growth speed and aspect ratio. Furthermore, the observed deviations between experiment and simulations might also be caused by inaccuracies of the used yield function. The slope of the yield is particularly high

5 Erosion of Surfaces With Initial Notches

at grazing incidence, where the erosion of the mean surface occurs. At the same time, experimental data in this angle region tend to be more sparse compared to close to normal incidence (Dieterle *et al.*, 2011). Since the divergence of the aspect ratio parameter is controlled by the vanishing of the mean erosion, it should be particularly sensitive to such inaccuracies of the yield function.

Aggregating all these observations, it seems reasonable to model the geometric parameters by a functions of the form:

$$d_{\text{ter}} = \tan \theta_{\text{eff}} \cdot w + d_0 \quad (5.8)$$

$$l_{\text{ter}} = \text{AR}(\theta_{\text{eff}}, w) \cdot (d_0 - d_{\text{ind}}) \quad (5.9)$$

$$\text{AR}(\theta_{\text{eff}}, w) = \text{AR}(\theta_{\text{eff}}, w_0) + c_{\text{AR}}(\theta_{\text{eff}}) \cdot w \quad (5.10)$$

$$d_{\text{ind}}(\theta_{\text{eff}}, w) \approx c_{\text{ind}}(\theta_{\text{eff}}) \cdot w \quad (5.11)$$

These need to be determine for a given combination of target and ion species, ion energy¹, and ion beam characteristics, such as beam profile. These questions should be prioritized in future extensions of the model. Adoption of a three-dimensional model of surface erosion could also be useful in order to describe erosion with oscillating ion incidence.

¹Both the position of the peak of the sputtering yield's angular function and its relative strength can change with ion energy (Smentkowski, 2000).

6 Depth-Resolved Microstructure Characterization of Surface-Crystallized Glass Ceramics Using Initial Notches

In this chapter, two case studies of initial notch sectioning are presented. The first material system under investigation is a diopside glass ceramic with pronounced texture formation which was crystallized from an near-stoichiometric melt. The second case study was performed on a $\text{Ba}_2\text{TiSi}_2\text{O}_8$ fresnoite glass ceramic crystallized from a glass with excess SiO_2 , which exhibits a more complex growth behaviour due to the presence of chemical enrichment effects.

6.1 Diopside

In work related to this thesis, parameters influencing texture formation and oriented nucleation resulting from surface crystallization were investigated, such as annealing duration, surface finish, and ambient atmosphere during annealing. Diopside was chosen as one model system with a known strong tendency towards oriented nucleation (Wisniewski *et al.*, 2012; Otto *et al.*, 2013). Selected results are depicted in Fig. 6.1. Further details on these studies can be found in Tielemann *et al.* (2021). From these diopside glass ceramics, a sample was selected in order to analyze orientation-dependent growth phenomena. The results discussed in the subsequent paragraphs were published in Busch *et al.* (2021b).

A sectioning scheme with a single erosion cycle was used. First, the pristine sample surface was characterized using SEM, EBSD and WLI. Then, sectioning using initial notches was performed, followed by another iteration of surface characterization. Notches were cut using PFIB milling and terrace formation was facilitated using stationary glancing angle broad ion beam erosion at 5° ion incidence angle and 3.5 kV acceleration

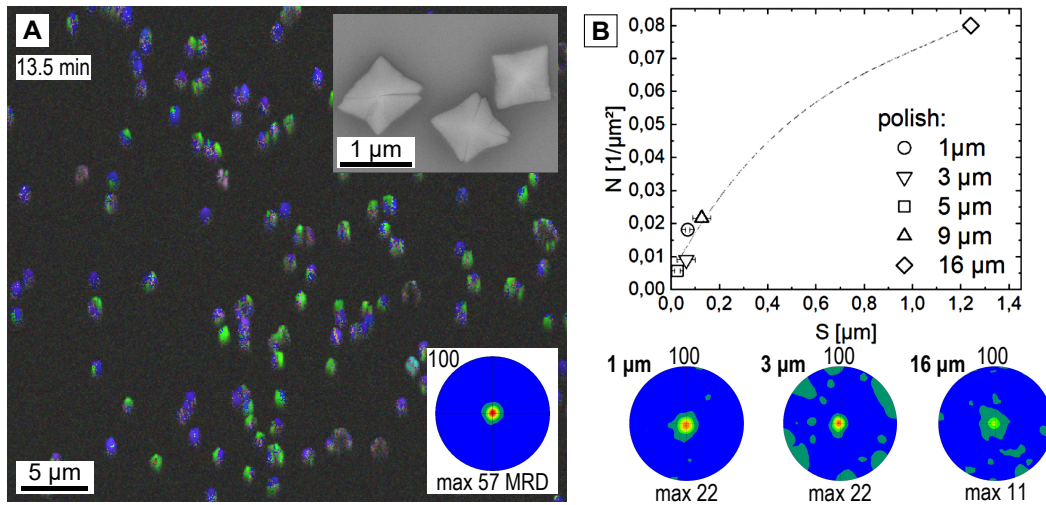


Figure 6.1: Dependence of surface crystallization and texture formation of diopside on annealing conditions. (A) Oriented surface crystallization was confirmed for very early stages with crystal sizes close to the EBSD detection limit (annealing for 13.5 min at 850 °C). (B) Dependence of surface crystallization on surface polish (using a diamond polishing slurry with grain sizes from 1 μm to 16 μm). Nucleation density strongly depends on surface finish, which is apparent in the diagram on top linking nucleation density N and mean surface roughness S . In contrast, orientation preference depends weakly on surface polish, only showing a broadening due to increased roughness (bottom row). For details, see Tielemann *et al.* (2021).

voltage, followed by a final polishing step at a reduced acceleration voltage of 1 kV.

SEM micrographs of the surface prior to and after broad ion beam erosion are shown in Fig. 6.2. The sample is relatively densely covered with diopside crystals protruding from the surface, but hasn't fully crystallized yet (Fig. 6.2A). In the upper part of the micrograph, most crystals are in direct contact with at most one neighbouring crystal, whereas in the lower part of the micrograph, some clustering of the crystals occurs. The diopside crystals exhibit a narrow size distribution around $\approx 10 \mu\text{m}$ diameter. A pyramidal shape is most common, but some crystals also feature an oval shape. After broad ion beam erosion (Fig. 6.2B), the protruding crystals have been levelled and a flat terrace has formed. Formation of fine grooves along the ion beam incidence direction is found. In the higher magnification micrograph (inlay in Fig. 6.2B), it can be seen that groove formation tends to take place at the edges of crystals, pointing to differential milling between the glass matrix and diopside crystals.

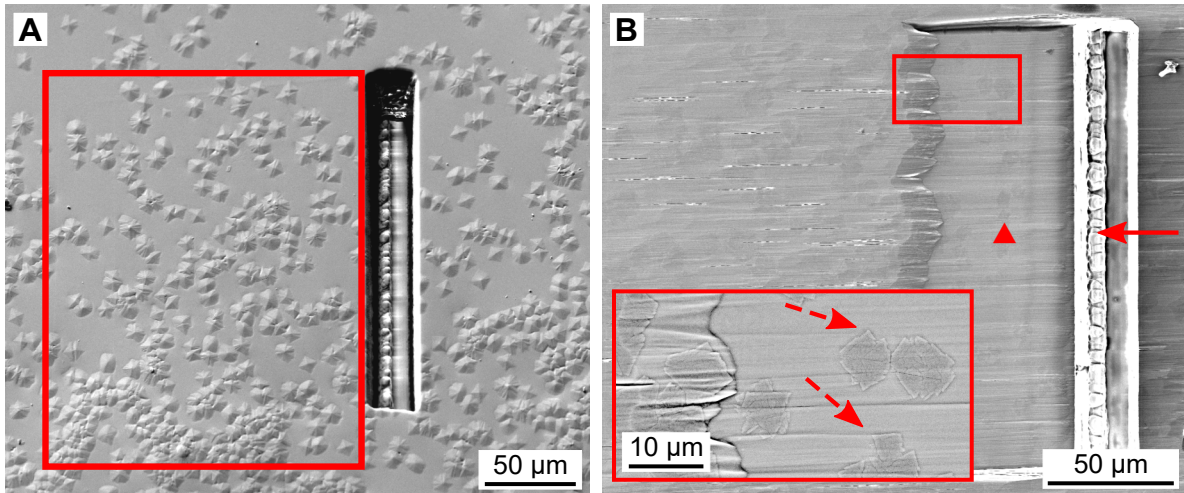


Figure 6.2: Top-view SEM micrographs of surface crystallized diopside before (A) and after (B) initial notch sectioning. The rectangle in (A) indicates the region where EBSD measurements were subsequently performed. The inlay in (B) shows a micrograph taken with increased backscattered electron signal to enhance the visibility of the diopside crystals. The incidence direction of the Ar^+ ion beam is indicated in panel (B) by an arrow and the terrace area by a triangle \blacktriangle . The dashed arrows are highlighting curtaining artefacts introduced at the edges of the crystals during erosion.

EBSD and WLI measurements have been performed in the region indicated by the box in Fig. 6.2A. A topography map showing the erosion depth after broad ion beam erosion is shown in Fig. 6.3A. The terrace is situated at an average depth of $5.1\ \mu\text{m}$ from the initial surface, whereas the average erosion depth within a similarly sized region behind the terrace is $2.0\ \mu\text{m}$. A gradient is visible in the topography map, which stems from the initial topography of the sample possessing a pronounced curvature.

Normal direction inverse pole figure mappings of the surface prior and after broad ion beam erosion are shown in Fig. 6.3B and Fig. 6.3C, respectively. Prior to broad ion beam erosion, the surface consists mostly of crystals which are oriented either with their (100) pole or their (010) pole parallel to the surface normal.¹ The crystals exhibit notable distinctions in form, with the former having a quadratic base and the latter a rectangular base. These differences are pointing to different, orientation-dependent growth velocities. After broad ion beam erosion, a decrease in the amount of crystals with

¹Conversely, the (100) and (010) planes are perpendicular to the surface normal and parallel to the surface plane.

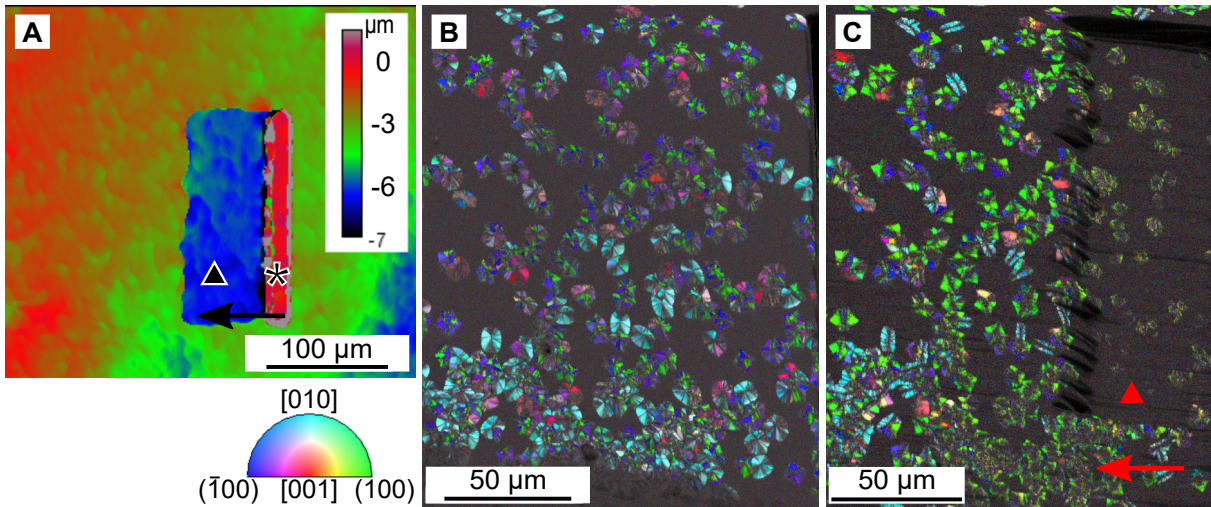


Figure 6.3: Erosion depth map, calculated as difference between topography measurements before and after erosion (A) and inverse pole figure maps of surface crystallized diopside before (B) and after (C) initial notch sectioning. The incidence direction of the Ar^+ ion beam is indicated by an arrow, the notch by an asterisk $*$ and the terrace area by a triangle \blacktriangle . Note that the bottom of the notch is not subject to ion bombardment, hence no change in depth occurs at $*$ in (A).

(010) perpendicular to the sample normal is noticeable, particularly in the bottom region of the dataset and in the terrace region. These observations are confirmed by texture calculations, which were performed on different subsets of the data: (A) the pristine surface, (B) the surface after broad ion beam erosion except for the terrace region and (C) the terrace region (Fig. 6.4). At the pristine surface, a bimodal orientation distribution is present where either (100) or (010) is parallel to the surface (Fig. 6.4A). With a maximum value of 17 multiples of random distribution (MRD), the (100) component is the stronger of the two components. With increasing depth from the surface, the texture changes towards a unimodal distribution, leading to a stronger peak of 23 MRD for the (100) component and a decreasing (010) component (Fig. 6.4B). In the terrace region (Fig. 6.4C), the (010) component has completely vanished. Moreover, the peak in the (100) pole figure is moving away from the normal direction. This indicates a rotation of the crystals upon further growth into the bulk.

Deeper insights in the growth processes can be gained by analyzing the relation between orientation, morphology, and growth behaviour of individual crystals. In Fig. 6.5, inverse

6 Depth-Resolved Microstructure Characterization Using Initial Notches

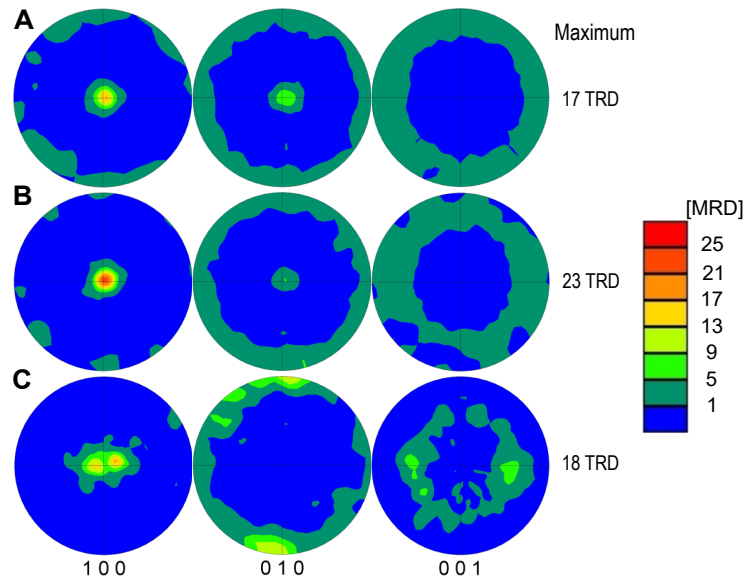


Figure 6.4: Crystallographic texture in multiples of random distribution (MRD), calculated for three different regions-of-interest: at the pristine surface (A), the eroded surface excluding the terrace area (B) and the terrace area after erosion (C).

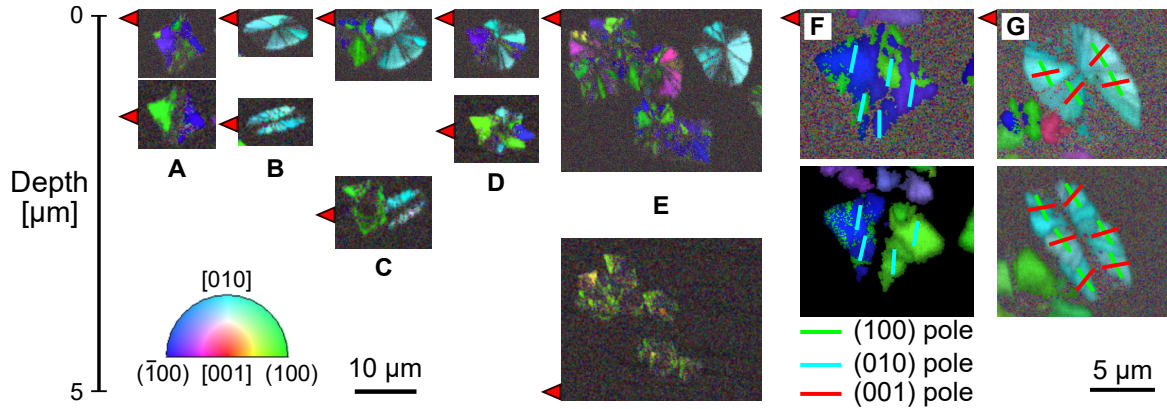


Figure 6.5: Inverse pole figure map of five crystals or agglomerations of crystals at the pristine surface (top) and at the eroded surface (bottom) at depths of 1.3 μm (A), 1.4 μm (B), 2.6 μm (C), 1.5 μm (D) and 5.0 μm (E), respectively. The triangles \blacktriangleleft indicate the depth position of each map fragment as determined from Fig. 6.3A. The directions of the (100), (010) and (001) poles in the surface plane are shown for a crystal with (100) pole and (010) pole perpendicular to the surface normal in (F) and (G), respectively.

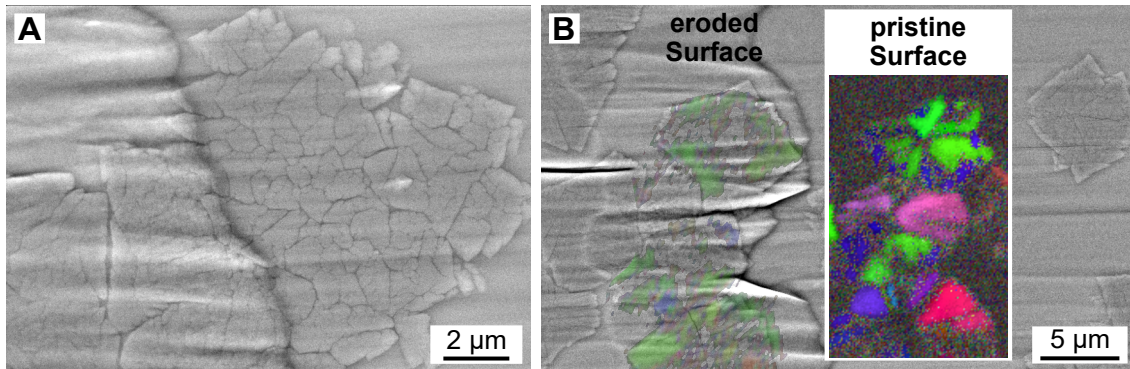


Figure 6.6: Top-view SEM micrograph of a crystal at a deeper erosion depth, which shows a strong fragmentation (A), and crystals directly on the end of the terrace sliced at an elevated angle (B). Inverse pole figure maps are overlaid on the SEM micrograph (note that the topography causes local distortions which cannot be corrected for by global linear transformations such as rotations, stretching and shear) and the inlay shows the corresponding 001-IPF map at the initial surface.

pole figure representations of selected crystals are shown both at the pristine and the eroded surface. Crystals with (100) parallel to the surface tend to maintain their shape during the first few μm of growth (Fig. 6.5A). In contrast, crystals with (010) parallel to the sample surface exhibit clearly anisotropic growth into the bulk, where the long axis doesn't show a notable length change from the surface, but the short axis becomes even narrower (Fig. 6.5B). Notably, a segmentation of the crystal is observed, as indicated by the lines of lower image quality within the two wedges. No similar behaviour was observed for crystals of the (100) component at the same depth. As a consequence of their increased growth speed, crystals with (100) perpendicular to the surface tend to outgrow the crystals with (010) perpendicular to the surface (Figs. 6.5C and 6.5D). On the terrace, it can be clearly observed that the (010)-oriented crystals have grown less deep than the (100)-oriented crystals (Fig. 6.5E). At this depth, the image quality of the (100)-oriented crystals deteriorates and considerable fragmentation can be noted, which is also observed in SEM micrographs of the terrace region (Fig. 6.6).

In Figs. 6.5F and 6.5G, the in-plane orientation of (100)- and (010)-oriented crystals is indicated by highlighting direction of (100), (010) and (001) poles. For (100)-crystals, the (010) pole is found to be uniformly oriented over the whole crystal. The (001)-pole is perpendicular to this direction, but with a slight out-of-plane inclination due to the

6 Depth-Resolved Microstructure Characterization Using Initial Notches

monoclinic angle. Upon further growth, these crystals tend to develop an unindexable region across the center and parallel to (010). In contrast, (010)-oriented crystals tend to exhibit four indexable regions characterized by an alternating in-plane orientation of the (001)-pole. The unindexable parts at the two short edges of the crystals are thus pointing towards the (100)-pole. Hence, each two opposite sectors share the same orientation but are separated from neighbouring sectors by a twin relation. In addition to crystals on either of the plane sample regions (terrace or the surrounding regions at mean surface erosion depths), crystals on the sloped region were indexable and can be analyzed this way as well (c.f. Fig. 6.6B), with some limits due to topography (detector shadowing, data distortion).

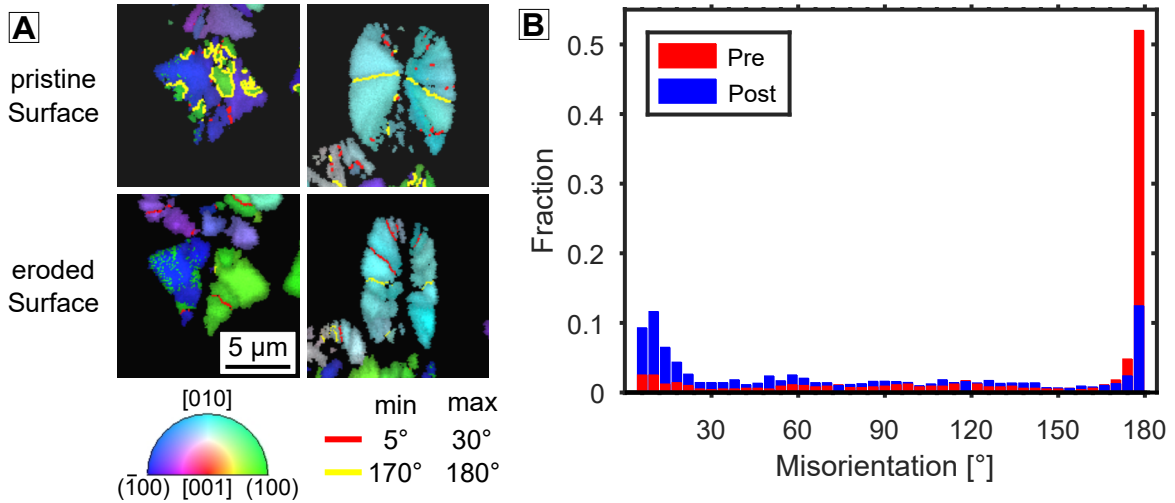


Figure 6.7: Misorientations of boundaries between diopside grains: inverse pole figure map with indicated grain boundaries of (100)- and (010)-oriented crystals at pristine and eroded surface levels (A) and misorientation histogram (B).

Analysis of grain boundaries was performed using an additional, single-cycle grain dilation process for regularisation of the dataset. In Fig. 6.7A, inverse pole figure maps are shown where grain boundaries have been colour coded². At the immediate surface, most diopside crystals feature some grain boundaries with 180° misorientation angle (yellow). For (100)-oriented crystals, these boundaries are distributed irregularly over

²Note that grain identification was performed on a threshold misorientation value of 5°, i.e. a point belongs to a grain if there is at least one neighbouring point from that grain with less than 5° misorientation.

the crystal area. For (010)-oriented crystals, the 180° boundaries generally cut across the middle of the crystal between the two indexable sectors on each side. After erosion, clear changes to these patterns occur. Most of the grain boundaries with 180° misorientation have vanished for the (100)-oriented crystals, but are still present for the (010)-oriented crystals. Furthermore, a pronounced increase in a small-angle grain boundaries with misorientations between 5° and 15° can be observed for crystals of both kind. These trends are confirmed by the misorientation histogram in Fig. 6.7B.

6.2 $\text{Ba}_2\text{TiSi}_2\text{O}_8$ fresnoite (BTS)

As a second model system, near-stoichiometric $\text{Ba}_2\text{TiSi}_2\text{O}_8$ fresnoite (BTS) glass ceramics with additional SiO_2 were investigated. The role of ambient conditions in surface crystallization was studied by performing annealing experiments in different atmospheres (ambient and dry air, Ar, and vacuum). Pronounced differences in crystal growth rates and resulting crystal morphologies were observed (see Fig. 6.8). The morphologies ranged from relatively circular crystals slightly depressed into the surface (ambient air) to spear-shaped crystals (dry air), weakly-branched, plate-like dendrites with parallelly arranged ramifications (Ar) to strongly-branched, star-shaped dendrites (vacuum). A detailed account of these studies can be found in Scheffler *et al.* (2023). The sample annealed in dry air was further analysed using initial notch sectioning.

In Fig. 6.9A, an SEM micrograph of the initial surface is shown. The surface is sparsely covered with elongated, leaf-shaped crystals with typical lengths of $20\ \mu\text{m}$ to $30\ \mu\text{m}$. Most crystals are spatially separated from each other and proximity between crystals is low. Some of the crystals are surrounded by smaller areas of fine-grained, dendritic crystal growth with significant amounts of residual glass between crystals. In a few cases, inclusion or pockets of dendritic growth have also formed within a crystal, as in Fig. 6.9B. The leaf-shaped crystals exhibit a topography which is depressed towards the center by orders of $3\ \mu\text{m}$ (Fig. 6.9C).

EBSD measurements were performed on the initial surface using a scan step size of $1\ \mu\text{m}$ (Fig. 6.10). The larger leaf-shaped crystals could be resolved relatively well. However, some crystals exhibit regions of very low image quality value (low pixel brightness in the map). This effect appears to be directional, with crystals aligned parallel to the incident electron beam being less affected than crystals perpendicular to the incident electron beam. These observations suggests that the crystal topography is adversely

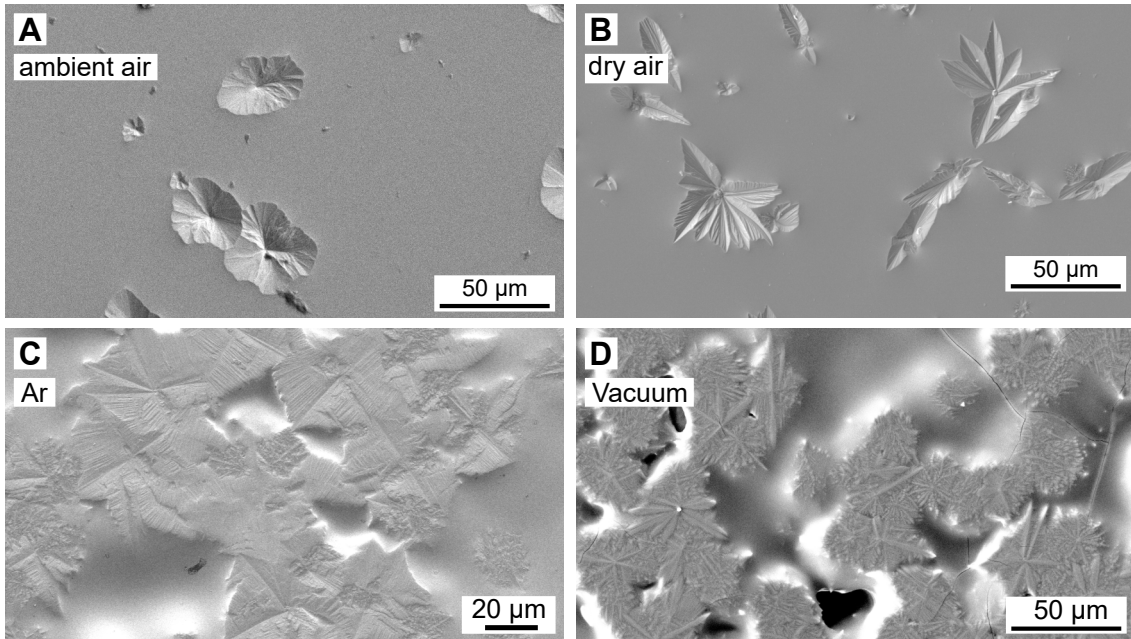


Figure 6.8: Morphologies resulting from surface crystallization of fresnoite in different ambient conditions. Samples were annealed at 825 °C for (A) 70 min in ambient air (43% relative humidity, 20 °C), (B) 75 min in dried air (48 ppmv), (C) 225 min in an argon atmosphere and (D) 435 min in vacuum. For details, c.f. Scheffler *et al.* (2023).

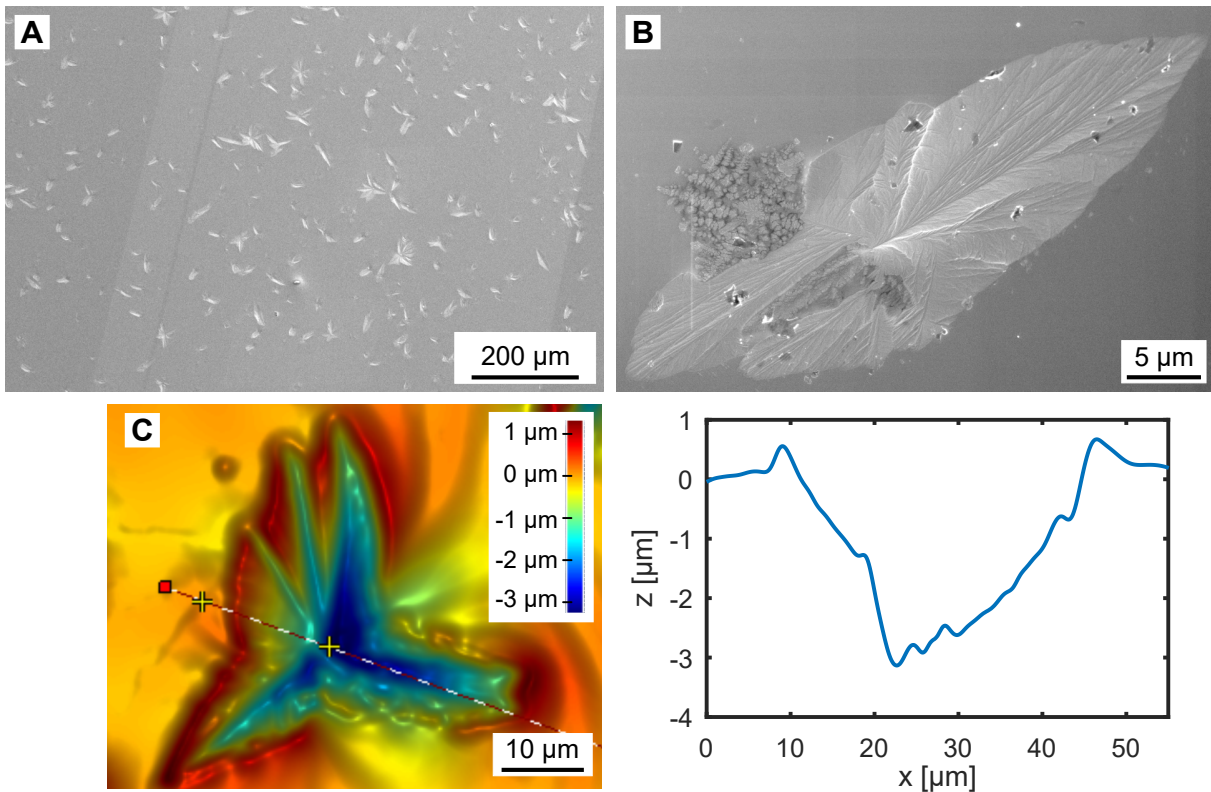


Figure 6.9: Initial surface state of the BTS fresnoite sample: (A) SEM overview micrograph taken after the EBSD measurement on the initial surface (the scan area is noticeable as brighter parallelogram area), (B) SEM micrograph of an individual, leaf-shaped crystal with regions of dendritic growth, and (C) topography map and line profile of an individual crystal measured with WLI.

6 Depth-Resolved Microstructure Characterization Using Initial Notches

affecting backscatter patterns, for example via detector shadowing. A moderate orientation preference for (310) parallel to the surface was detected. In contrast, (001) is perpendicularly oriented to the surface, or in other words, the (001) pole is lying in the surface plane.

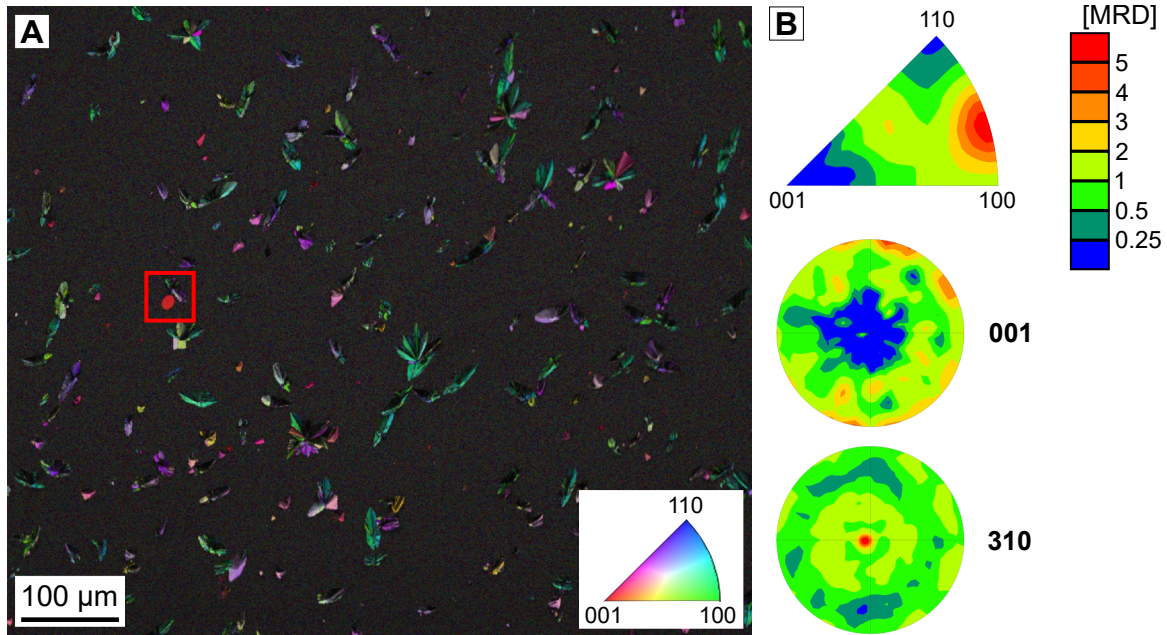


Figure 6.10: (A) EBSD data of the pristine fresnoite surface: normal direction IPF map where the pixel brightness is modulated by image quality. The rectangle indicates the circular crystal depicted in Fig. 6.15. (B) Normal direction inverse pole figure as well as (001) and (310) representation of crystallographic texture.

Regions-of-interest were defined for further analysis by initial notch sectioning based on the EBSD data. Notches of different shapes and dimensions were milled into the surface using fs-laser ablation. A SEM micrograph of the surface after notch cutting and subsequent snow-jet cleaning is shown in Fig. 6.11A. Notches consisting of two differently wide parts as well as notches with a trapezoidal shape have been used in addition to basic, rectangular notches. This way, both discrete height steps and continuous depth gradients were created as a result of the locally varying notch width. The maximum notch width of 100 μm was chosen based on the simulation data in Section 5.3.2 in order to achieve a maximal target depth on the order of 10 μm. This choice of depth scale was motivated assuming not too anisotropic growth speeds along the surface and into

6 Depth-Resolved Microstructure Characterization Using Initial Notches

the depth. The notch faces showed a limited degree of faceting, mostly in the first few μm below the surface. Only the smaller part of the double rectangles showed significant notch face roughness caused by the milling process (Fig. 6.11B). The two parts of the notch were milled sequentially with the small one being milled first, causing redeposition of ablated material upon milling of the second part.

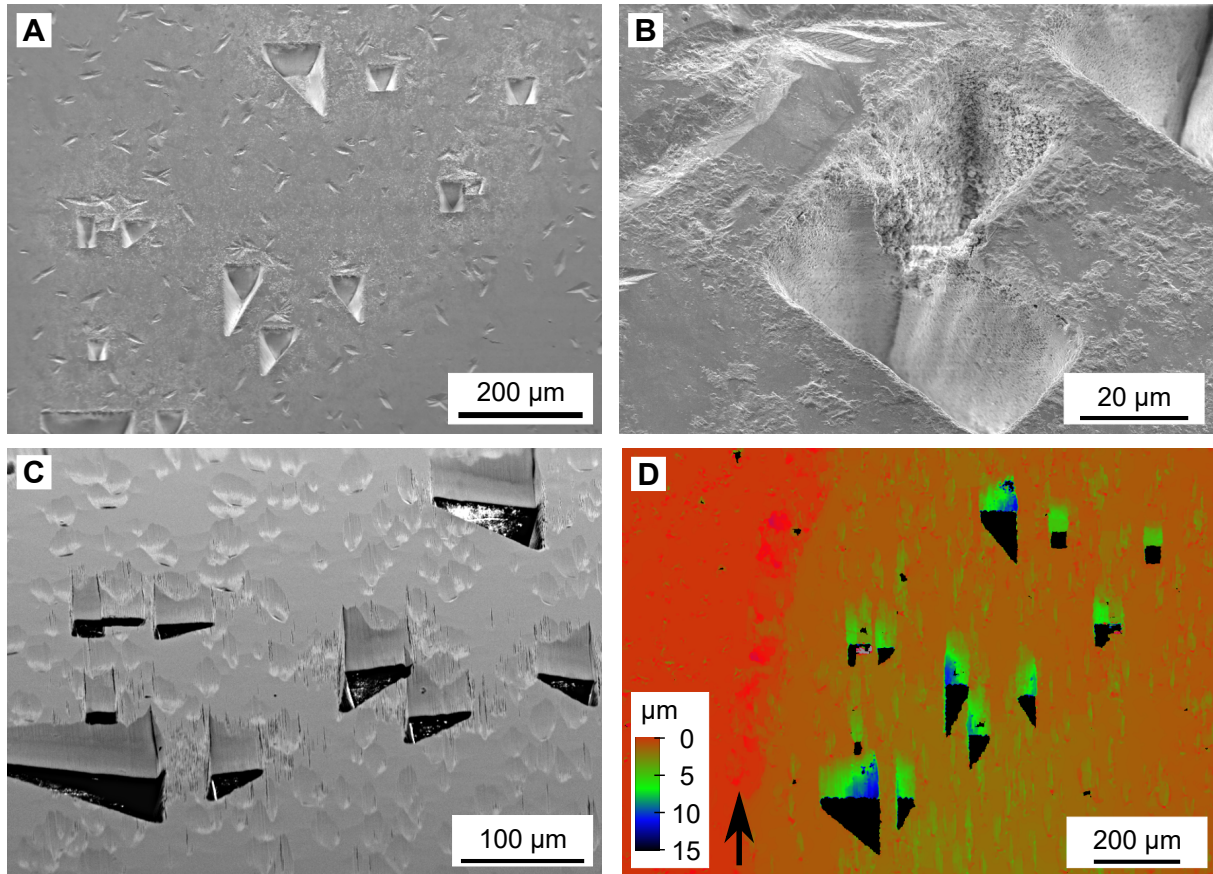


Figure 6.11: SEM micrographs of the fresnoite sample surface after notch milling with fs-laser ablation, taken at 70° sample inclination (A), and SEM micrograph of a single notch (B). SEM micrograph of the surface after glancing angle broad ion beam erosion, taken at 70° sample inclination (C), and erosion depth map of the eroded surface, determined from WLI measurements (D). The area on the left side of the depth map was covered with carbon tape during erosion to serve as a reference region for topography data alignment).

SEM micrographs and topography data of the surface after glancing angle broad ion beam milling are shown in Figs. 6.11C and 6.11D. Cracks were present around some of

6 Depth-Resolved Microstructure Characterization Using Initial Notches

the notches. Furthermore, pronounced formation of grooves aligned parallel to the ion beam milling direction is apparent on the surface. Grooves can be observed both on terraces and the surrounding regions in the ion beam irradiated area. Some of these grooves correlate with the position of crystals on the surface. Curtaining effects caused by the topography of the leaf-shaped crystals thus likely play a role, as could preferential erosion at spatial inhomogeneities such as inclusions of residual glass. Another possible influence is residual debris that stuck to the surface and could not be removed by the cleaning procedure. Microcracks caused by thermal load during laser ablation or ion beam erosion could also be responsible for these grooves. Noteworthy, these grooves appear to be less pronounced or absent on the deeper terrace levels behind wider notches or notch areas. The depressed central region of some crystals can still be discerned on the surface, particularly outside of the terrace regions.

The morphology of crystals below the initial surface can be clearly discerned in backscattered electron micrographs. Figure 6.12A shows a crystal at 4.6 μm distance from the initial surface is shown. It is exhibiting a pronounced dendritic morphology and reduced apparent grain sizes. Furthermore, there are several pockets of residual glass within the cluster. At higher magnification, small spherical structures with a mean structure size of (21 ± 5) nm can be discerned in the residual glass (* in Fig. 6.12B). The reduced backscattered electron intensity indicates a lower average atomic number than the surrounding fresnoite crystal. Hence, these spherical particles likely are SiO_2 -droplets formed via liquid phase separation in the silicon enriched residual glass between the fresnoite crystal. A second peculiarity is the presence of small inclusion within the some of the crystals (#).

Occurrence of similar growth morphologies was also observed in STEM measurements performed on a cross-sectional lamella from a sample annealed in Ar (Fig. 6.12C and Fig. 6.12D). Elemental mappings taken with EDXS are shown in Fig. 6.12E. A pronounced depletion of Ti and an enrichment of Si are visible in the inclusion (marked by the red contour). Conversely, an enrichment of Si is discernible in the droplets. Quantification of the inclusion region marked by a red contour yielded a molar composition of 53.5 ± 5.0 mol% BaO, 12.0 ± 0.4 mol% TiO_2 and 34.5 ± 0.5 mol% SiO_2 . The crystalline region surrounding the inclusion was of fresnoite composition (51.3 ± 4.7 mol% BaO, 24.8 ± 0.4 mol% TiO_2 and 23.9 ± 0.3 mol% SiO_2), while the other regions were not well-enough spatially separated for reliable quantification.

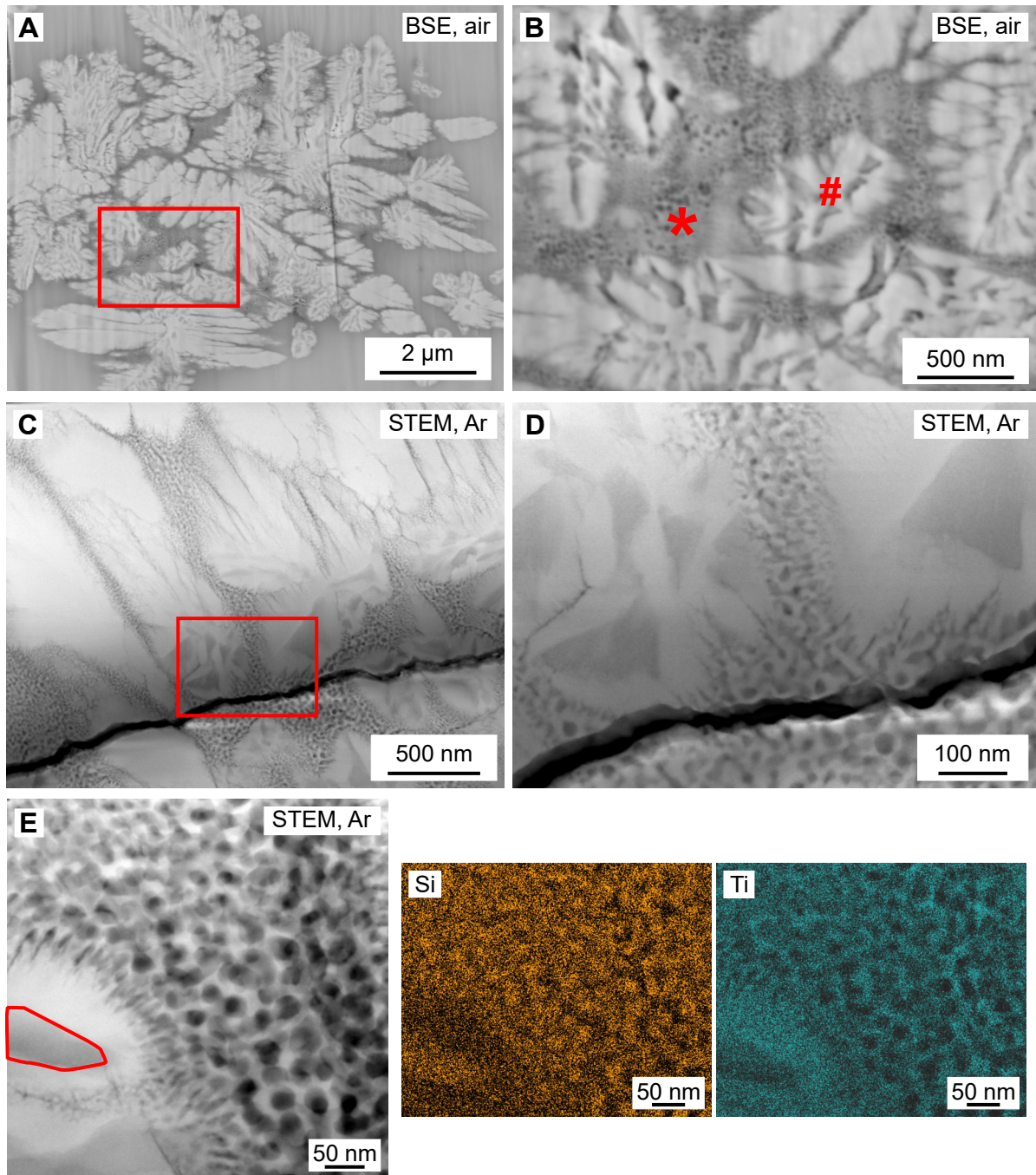


Figure 6.12: (A) Backscattered electron micrograph of a fresnoite crystal on a terrace at 4.6 μm depth from the initial surface. The region within rectangle is shown at higher magnification in (B). Similar morphologies were found in STEM high-angle annular dark-field (HAADF) micrographs of a cross-sectional lamella prepared from the BTS sample of Fig. 6.8C annealed in Ar atmosphere, (C) and (D). In this region of the sample, the secondary growth mechanisms start to occur at a distance of $\approx 1 \mu\text{m}$ from the surface. The black line across the micrographs is a fracture that occurred during lamella thinning. (E) HAADF micrograph and EDXS elemental mappings for Si and Ti.

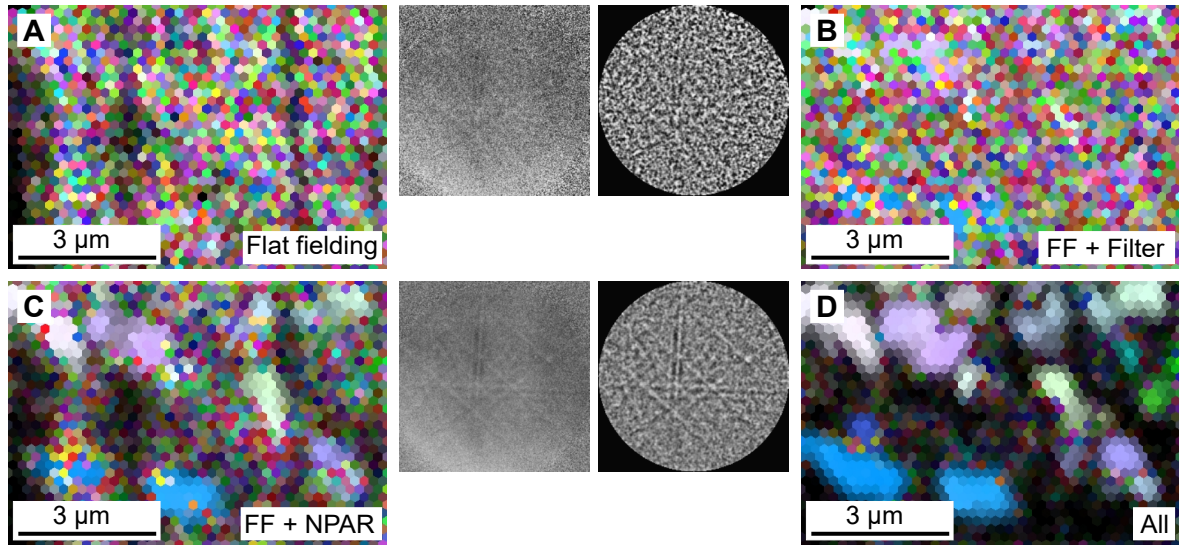


Figure 6.13: Electron backscatter pattern and inverse pole figure maps collected at 20 kV. Different image processing algorithms were applied to the backscatter patterns prior to indexing: (A) only flat fielding using division by a static back ground image, (B) flat fielding and noise reducing filters (mean filter and dynamic flat fielding using a Gaussian rolling ball technique), (C) flat fielding and spatial pattern averaging (NPAR) and (D) all processing steps combined.

Electron backscatter patterns of the crystals at increased depth exhibit significantly reduced band contrast compared to the initial measurements at the pristine surface. Consequently, EBSD measurements using comparable measurement parameters as during initial acquisition failed to provide satisfactory pattern quality and indexing rates. Lowering the scan step size to 200 nm did not alleviate this problem. By applying spatial pattern averaging to the recorded EBP and reindexing the data (NPAR, see Wright *et al.* (2015)), indexing rates could be significantly increased and at least partial indexing of the crystals regions achieved. Comparisons of patterns and data obtained thereof using different degrees of pattern processing and averaging are shown in Fig. 6.13 for the crystal depicted in Fig. 6.12A. As an overall trend, higher quality data can be recorded from crystal regions which contain less inclusions (#), and no bands can be detected from the region containing the small droplets (*).

Due to the drastically decreased feature size and crystal homogeneity below the surface,

6 Depth-Resolved Microstructure Characterization Using Initial Notches

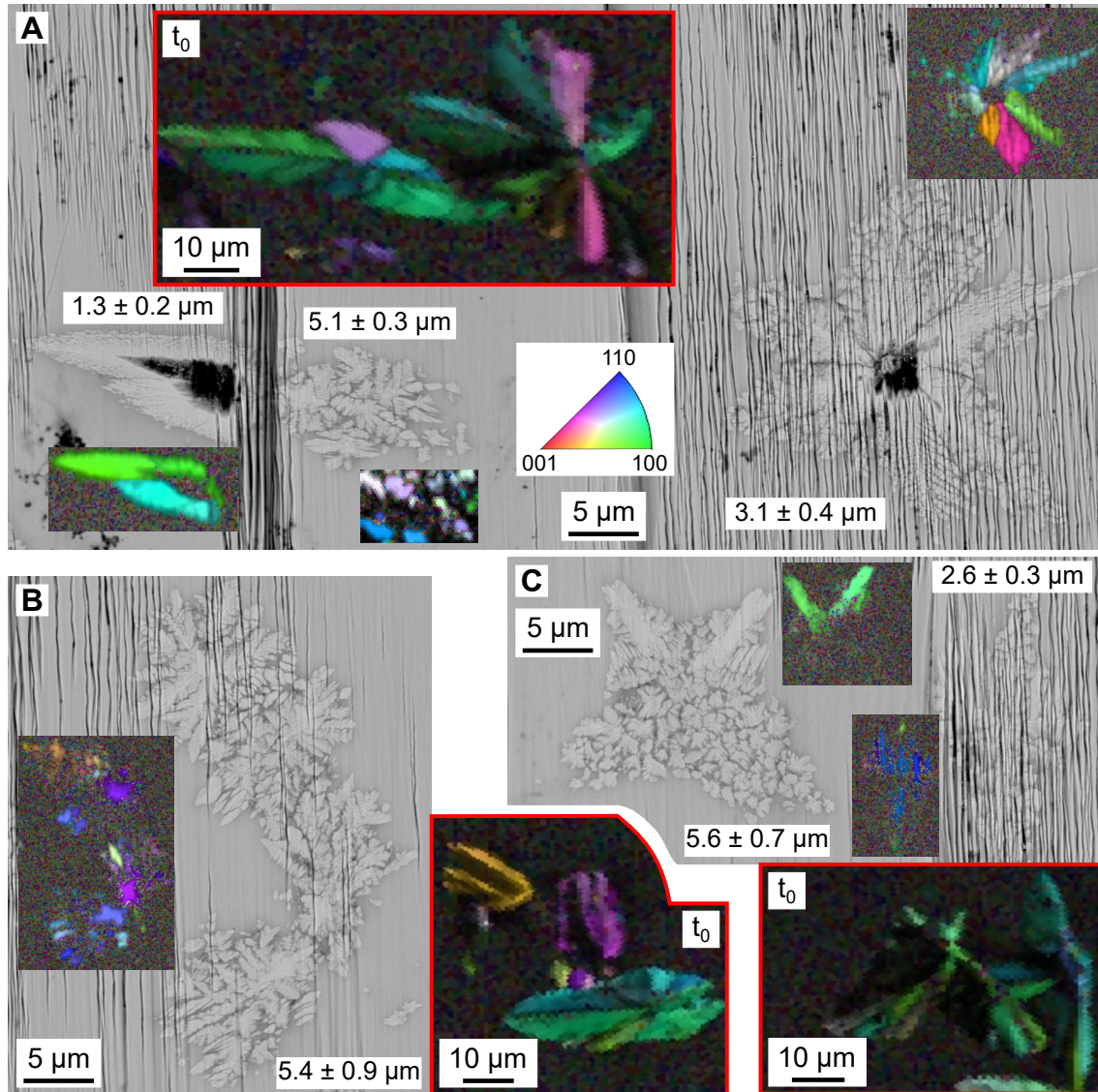


Figure 6.14: Backscattered electron micrographs of fresnoite crystals at different depths (indicated by the labels on each surface segment) from the immediate surface. Inverse pole figure maps are shown next to each crystal, at a reduced size for visual clarity. Given within the red contours are the IPF data of the corresponding region on the pristine surface (t_0). Note that distortions are present in the IPF data from the pristine surface due to topography.

6 Depth-Resolved Microstructure Characterization Using Initial Notches

performing a full surface scan comparable to Fig. 6.10 proved unfeasible. Quantitative analysis of texture differences or misorientation relations was therefore also unachievable. Hence, only qualitative analysis of individual EBSD crystals could be performed. In Fig. 6.14, inverse pole figure maps of scans performed with 200 nm are depicted alongside backscattered electron micrographs and the IPF data from the initial surface. In the shallow region (left) of Fig. 6.14A, a plane cross-section of leaf-shaped crystal is visible. The projected thickness around its central depression is approximately $2\ \mu\text{m}$ at $(1.3 \pm 0.2)\ \mu\text{m}$ depth from the surface. The other half of that crystal is lying on a lower surface level at an depth of $(5.1 \pm 0.3)\ \mu\text{m}$, where no remnant of the initial morphology can be determined. The crystal on the right at a depth of $(3.1 \pm 0.4)\ \mu\text{m}$ still exhibits the central leaf-shaped region with its depression, but shows a sharp transition outwards to a more highly branched morphology with substantial residual glass. Interestingly, the bottom branch of this crystal shows a rather regular dendritic morphology with parallel branches, while most other highly-branched dendrites show a rather irregular morphology. In Fig. 6.14B, crystals at $(5.5 \pm 0.9)\ \mu\text{m}$ already show a strongly branched morphology and a high fraction of residual glass, but still maintain a coarse orientation relation to the initial surface. In (C), the left crystal still shows remnants of the initial morphology at a depth of $(5.6 \pm 0.7)\ \mu\text{m}$ with a relatively good indexing rate, but the rest of the crystal fails to provide any indexable pattern. This behaviour confirms the relation stated above between pattern quality and degree of dendritic branching / inclusions. Overall it can be stated, that while the homogeneity of the crystal degrade substantially with depth, an approximate orientation relation to the surface crystals is preserved in most cases for depth $< 6\ \mu\text{m}$.

One peculiar observation should be noted here. Two crystals with a distinctly different, circular shape were found in the EBSD data set, which are oriented with the (001)-plane parallel to the surface. One of these crystals is marked in Fig. 6.10 by a rectangle. Notably, these crystals were hardly detectable using the in-lens SE detector under normal settings and didn't show any discernable topography, quite in contrast to all other crystals observed. With increasing backscatter signal (by suppressing low-energy electrons using the E×B filter of the in-lens detector and successively increasing the filter strength), the contrast could be enhanced significantly (Fig. 6.15). Furthermore, the pattern created by the scanning electron beam during EBSD data acquisition was visible atop the circular crystal in SE micrographs taken without energy filtering. These observations could

6 Depth-Resolved Microstructure Characterization Using Initial Notches

indicate that the circular crystals are not located directly at the surface, but rather below a thin covering layer.

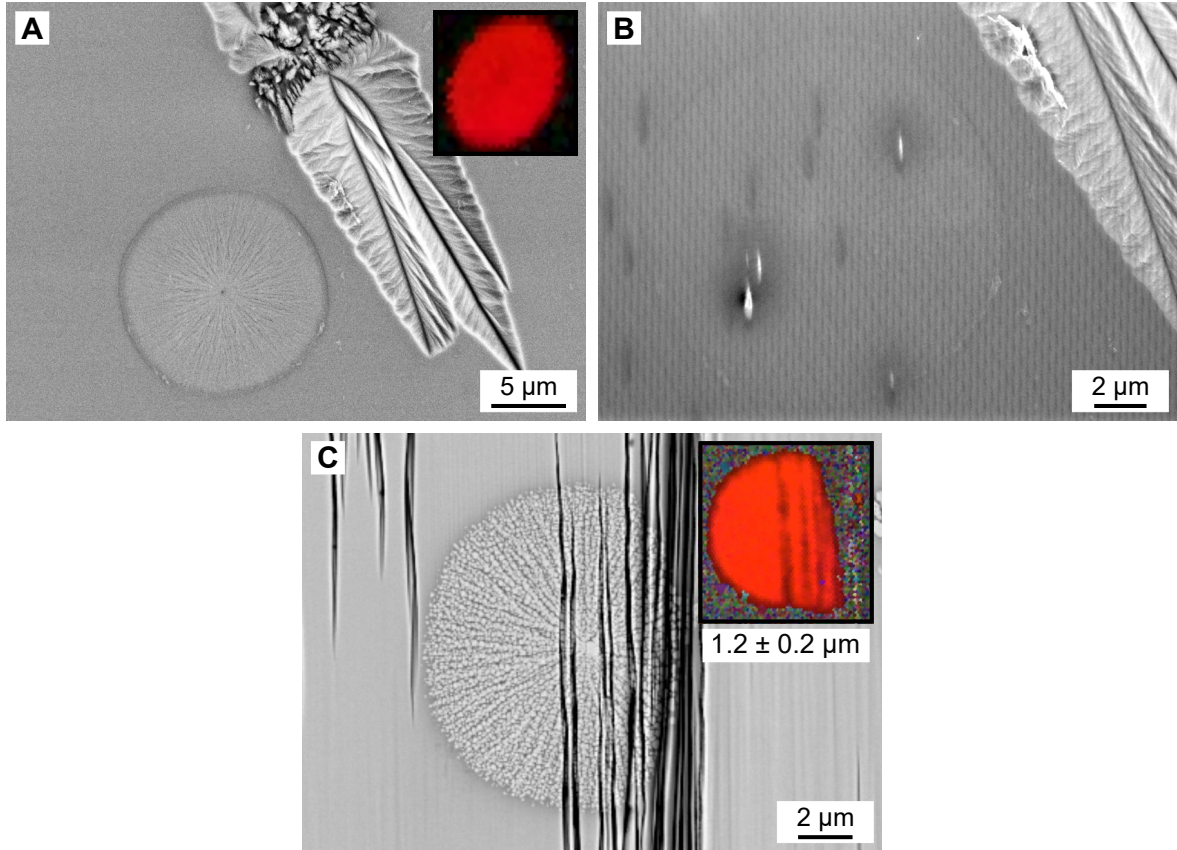


Figure 6.15: SEM micrographs of a spherical fresnoite crystals on the initial surface. In (A), low-energy secondary electrons have been suppressed using the E×B filter below the in-lens detector. In (B), no energy filtering has been applied and the surface patterning caused by the preceding EBSD measurement is visible. (C) Spherical crystal after initial notch sectioning at a depth of $(1.2 \pm 0.2) \mu\text{m}$. Inverse pole figure data are shown next to the crystal (not to scale).

6.3 Discussion

6.3.1 Methodological Aspects of Initial Notch Sectioning

Initial notch sectioning was successfully applied to a diopside and a fresnoite glass ceramic and enabled a depth-resolved study of the surface-near microstructure. Two different experimental approaches were applied, using either focused ion beam milling or laser ablation for notch milling. Both techniques proved feasible for the purpose of initial notch sectioning. Focused ion beam milling in principle allows for higher precision notch creation due to the orders of magnitude lower beam spot size (depending on device and beam current: one to two orders for Xe PFIB, two to three orders for Ga FIB; see Bassim *et al.* (2014)). Furthermore, very little debris is created compared to laser ablation notch milling. However, this could also be a result of the different processing conditions involved, i.e. ambient atmosphere for laser ablation and vacuum for FIB milling, respectively. While pronounced notch face roughening was observed on the diopside glass ceramic (similar to the case of float glass, see Fig. 5.1C), the final terrace roughness was found to be rather influenced by differential milling between glass phase and crystals rather than by the notch quality. In contrast, laser ablation notch cutting allows for very rapid preparation but reduced accuracy, owing to the spot size of order 10 μm . Notches as large as 150 μm in lateral dimensions and 50 μm depth have been prepared in less than a minute process time.

Using particular notch geometries and notch arrangements on the sample provides a high degree of control over the precise location of the prepared sample region. By using notches in parallel (i.e. side by side), several neighbouring terraces can be formed at different depths. For samples with a laterally uniform microstructure, this scheme can facilitate simultaneous preparation of ROIs at multiple different depths. In turn, this can enable multiple measurements to be performed using just a single broad ion beam erosion cycle, as was demonstrated for the fresnoite glass ceramic. Alternatively, it would also be possible to use multiple notches in a row in order to rapidly excavate slices at successively increased depths, but one particular lateral position. In this case, each time the terrace formed behind a particular notch grows onto the next notch in line, a further jump in erosion depth occurs (c.f. Fig. 6.16A and (Höche & Krause, 2018)). An iterative procedure of erosion - measurement - erosion then enables the analysis of the same region at separate, distant depth levels.

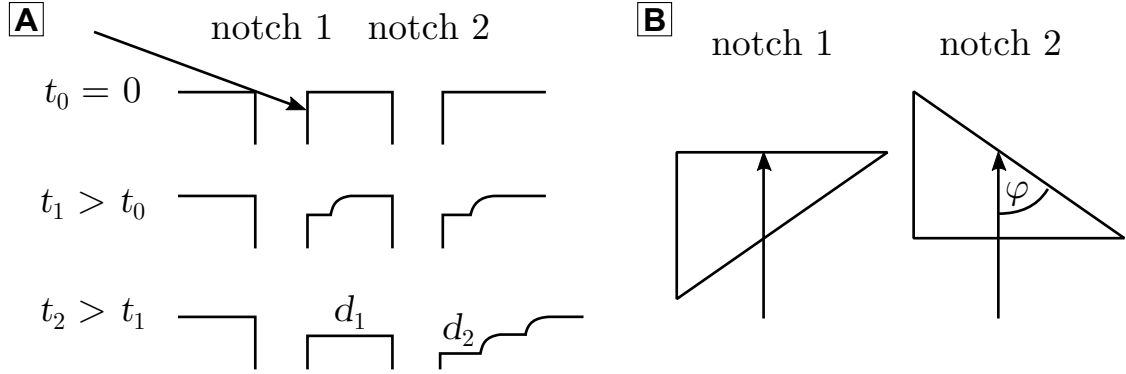


Figure 6.16: (A) Initial notch sectioning approach using two notches in a serial arrangement. First ($t = t_1$), the terraces grow separately behind each notch at a terrace depth d_1 . When the first terrace has fully developed and 'grows onto' the second notch at a time t_2 , a further receded terrace at a depth d_2 is formed. (B) Two notches related by a mirror transformation along the horizontal in top view. Non-perpendicular ion incidence at an angle φ can occur based on notch orientation.

Besides the basic rectangular geometry, advanced notch geometries such as triangles or trapezoids (as in Fig. 6.11) can be used in order to create terraces at a depth that varies with lateral position along the notch. Inclined terraces are formed as result of such a geometry, where the angle of inclination is controlled by the ratio of notch length and the difference in width along the notch. Preparation of inclined terraces could serve as an approach positioned between creation of parallel surface sections and cross-sectional preparation approaches. Other potentially useful notch geometries with variable width along the ion beam path could include sinusoids or step-wise, staircase-shaped notches.

It should be noted that notch shape and the orientation relative to the incident ion beam can influence the evolution dynamics of the terrace, which needs to be considered when designing initial notch sectioning experiments. In particular, the local ion incidence angle at the notch face can be altered for non-rectangular notches. When using triangular notches, for example, different terrace formation kinetics could be obtained depending on the orientation of the triangle (Fig. 6.16B), even when the notch width profile $w_{\text{notch}}(x)$ remains the same. In case of sinusoids, this out-of-plane angle would be furthermore position dependent. An extension of the model presented in Section 5.3 to three dimensions would be required for these settings, which would also be able to describe the effect of oscillating erosion strategies on terrace evolution kinetics.

6 Depth-Resolved Microstructure Characterization Using Initial Notches

Large sample regions of several hundred microns up to a millimeter were analyzed using initial notch sectioning. Especially for non-conducting specimen such as glass ceramics, the particular geometry employed proves advantageous. In conventional serial sectioning approaches (both FIB and laser), edge-on milling is performed, i.e. slicing from the side of the sample. This approach is prone to curtaining effect, which can become hard to control, particularly for larger, inhomogeneous samples (Gholinia *et al.*, 2020). Similarly, sample charging can be a problem in this geometry (Holzer & Cantoni, 2012). Furthermore, it usually requires extraction of a suitable test piece from a larger sample prior to the experiment and poses limits on the dimensions of said test piece. In contrast, no test piece extraction is required for initial notch sectioning using broad ion beams. As discussed in Chapter 2, broad ion beam milling is also advantageous in terms of milling rate over FIB. Analysis of samples with several millimetres lateral dimensions is thus enabled. However, for preparation of very large samples, a broad ion beam with appropriately large beam diameter is required in order to limit beam-profile related topography formation.

An extension of initial notch sectioning could be obtained by combining the technique with the broad ion beam serial sectioning approach introduced by Winiarski *et al.*, 2017. For example, initial notch sectioning could be used in a first step in order to quickly identify volumes of interest for further analysis. Afterwards, a full three-dimensional analysis could be enabled by continued broad ion beam erosion on the terraces created during initial notch sectioning. This amounts to analysis of a discrete number of subvolumes at different depth from the initial surface. Alternatively, a surface-near volume could be analyzed first using broad ion beam serial sectioning. Afterwards, a second region at the same lateral position and increased depth from the initial surface could be excavated using initial notch sectioning, followed by analysis of a second data volume at this depth level. This way, the microstructure could be traced over larger depths using a reduced number of measurements, reducing measurement duration and data sizes required.

Initial notch sectioning has some notable limitations. Due to the discrete step in erosion depth at the notch, the finite induction depth of terrace formation and the finite aspect ratio, the method is disadvantageous if very thin layers of material ($<1\ \mu\text{m}$) needs to be removed. Here, conventional broad erosion without notch is a better alternative. Furthermore, the proper choice of notch and ion beam geometry requires some degree of prior knowledge about the relevant length scales over which the microstructure changes

from the initial surface. Usage of multiple, differently-sized notches can alleviate this problem in cases of laterally homogeneous samples. If targeted preparation of a specific sample feature is required and no such prior knowledge is available, an edge-on FIB or laser sectioning approach might be better suited.

6.3.2 Microstructure Analysis on Surface-Crystallized Glass Ceramics

Diopside

Preferentially oriented crystalline surface layers as well as depth-dependent changes in microstructure were found in both systems under investigation. In diopside, textured surface crystallization has previously been reported by Wisniewski *et al.* (2012) and Otto *et al.* (2013). There, bimodal orientation distributions were found where the (100)- or the (010)-pole is preferentially oriented parallel to the surface normal and (001)-pole is lying in the surface plane. Furthermore, investigations on mechanical cross-sections as well as surfaces polished at low angles had been performed by (Wisniewski *et al.*, 2012) to reveal depth-dependent changes in microstructure. It was found that a relative weakening of the (010)-component of the texture and a strengthening of the (100)-component occurs. This observation had been explained by growth selection effects. Furthermore, a continuous shift in orientation was also observed, where the (001)-pole rotates from a preferred in-plane orientation towards one parallel to the surface normal. Chemical changes at the growth front leading to a depletion of magnesium and oxygen and a accumulation of calcium had been suggested to cause these growth effects. Results presented herein as well as in a related contribution (Tielemann *et al.*, 2021) mostly confirmed these observations, while providing extensions of some aspects.

First, occurrence of textured surface crystallizations was confirmed for glass ceramics with low surface nucleation density and short annealing durations, corresponding to early crystallization stages and small crystal diameters (down to 700 nm total crystal diameter, cf. Fig. 6.1). Considering that diopside crystals exhibit formation of sectors with different orientation, some of which fail to provide Kikuchi patterns suitable for EBSD analysis, this crystal size has to be considered close to the detection limit of the technique. Hence, evidence is strengthened that the observed preferential orientation is purely a result of oriented nucleation and not growth selection (whether in-plane or out-of-plane within surface-near regions). Furthermore, potential effects from crystal-crystal interaction on orientation, for example caused by chemical gradients or strain fields around the crystals,

6 Depth-Resolved Microstructure Characterization Using Initial Notches

can also be excluded in this current setting.

Second, differences in the relative strength of the two dominant texture components were observed. In contrast to Wisniewski *et al.* (2012) where the texture at the immediate surface was dominated by the component with (010) parallel to the surface, both bimodal textures with a dominant (100)-component as well as unimodal textures only possessing the (100)-component were found in Tielemann *et al.* (2021) (note that the latter constitutes a limiting case of the more general bimodal texture). The same nominal glass composition has been used in both studies as well as similar maximum annealing temperatures (850 °C and 870 °C, respectively). Hence, it can be concluded that the relative strength of the different components is sensitive to the ambient conditions during annealing as well as to the precise heating protocol, providing further opportunities to tailor the surface texture.

It is worthwhile discussing these observations in context of the crystal structure of diopside. Diopside is a clinopyroxene chain silicate crystallizing in the monoclinic system. It has space group $C 2/C$ and unit cell parameters are $a = 9.741 \text{ \AA}$, $b = 8.919 \text{ \AA}$, $c = 5.257 \text{ \AA}$ and $\beta = 105.97^\circ$ (Sasaki *et al.*, 1980). While classical treatments of nucleation (e.g. Gutzow, 1980a, 1980b) are not able to predict orientation dependent surface nucleation, two different empirical approaches towards linking orientated nucleation to crystal structure have recently been proposed (Wisniewski & Rüssel, 2021; Tielemann *et al.*, 2021). The first treatment proposes a minimization of the area per atom of the least mobile species (generally being the network formers) in the plane parallel to the sample surface. Applied to diopside, values of 24.03 \AA per Si atom for the (100) plane and 25.28 \AA for the (010) plane are given, whereas the (001) possesses a much higher value of 44.63 \AA . Hence according to this approach, both (100) and (010) should possess relatively similar likelihood to be parallel to the surface, with a slight preference for (100). The second approach - based on the assumption of different interfacial energies between crystal and melt on the one hand and crystal and ambient atmosphere on the other hand - argues for a minimization of the total surface energy of the nucleus when a minimum-energy cut plane is oriented parallel to the surface. This minimum-energy cut plane is estimated in Tielemann *et al.* (2021) based on the number of atomic bonds severed, the coordination, and on tabulated diatomic bond energies. Applied to diopside, the following estimates are provided therein for the minimum cut energy E_{hkl} : $E_{(010)} = 1.4 \text{ J/m}^2 < E_{(100)} = 2.7 \text{ J/m}^2 < E_{(001)} = 7.3 \text{ J/m}^2$. According to this model,

6 Depth-Resolved Microstructure Characterization Using Initial Notches

the strongest texture component should thus exhibit (010) parallel to the surface.

Both of these models provide reasonable explanations for the overall surface crystallization behaviour of diopside, but are insufficient to fully predict the details of the texture. In particular, both (100) and (010) appear to exhibit relatively similar orientation preferences at the immediate surface, which experimentally appears to be swayed in one direction or the other by the precise annealing conditions. Comparing the basic assumptions of both models, it might be possible that they are best applied to different nucleation regimes. More precisely, Wisniewski and Rüssel (2021) posit that nucleation is essentially a diffusion limited process, hence the prominent role of the least mobile species. Accordingly, it might be expected that annealing at higher viscosity matches more closely to the predictions of this model. This can for example be achieved by lowering the annealing temperature. Another possible influence on viscosity might be humidity in the furnace atmosphere, as discussed below for the fresnoite glass ceramics. Conversely, a minimization of surface energy as suggested by Tielemann *et al.* (2021) might more accurately describe annealing at lower viscosities.

Additional insight into the mechanisms affecting growth into the bulk have been provided in this study. The previously reported growth selection mechanism leading to a shift from bimodal to unimodal texture was confirmed in this thesis. However, it was found that subtle changes in crystal structure also occur over the first few μm . First and most notably, an increase in small-angle grain boundaries with misorientations between 5° to 15° occurs, both for (100)-oriented and (010)-oriented crystals. In the case of (010)-oriented crystal, these small-angle grain boundaries are aligned radially and are in correspondence with the observed, increased fragmentation of the crystals beneath the pristine surface. These effects are likely a reflection of orientation dependent stress fields, which induce particular spatial distributions of crystal defects. Furthermore, a decrease in 180° twin boundaries was observed for (100)-oriented crystals, along with the formation of a central region from which no indexable patterns were obtained. In contrast, no change in the arrangement of 180° twin boundaries was observed for crystals with (010) parallel to the surface.

Different mechanisms of twin formation could explain the observed twinning patterns in both cases. The fact that twins do not persist for (100)-oriented crystals makes it unlikely that they were already present during growth from the surface. Rather, it is likely that the twins at the immediate surface were formed as deformation twins during

6 Depth-Resolved Microstructure Characterization Using Initial Notches

cooling of the sample. Relatedly, tensile stresses at the immediate surface were already suggested by Wisniewski *et al.* (2012) in order to explain the observed protrusion of diopside crystals out of the surface. The irregular spatial distribution of twins seems to support this hypothesis. In contrast, the twins present in (010)-oriented crystals likely stem from growth twinning, i.e. they are formed during the growth of these crystals. Hence, their twinning patterns persist into the bulk.

Further rotation of crystals initially oriented with (100) parallel to the surface upon growth was also observed in the present data. However, the hypothesis of chemical gradients as the cause, as argued for by Wisniewski *et al.* (2012), does not appear convincing. While chemical gradients were also observed for the diopside samples under investigation (for details, see Tielemann *et al.* (2021)), there was no indication that these gradients are anisotropically distributed. In contrast to the studies by Wisniewski where a high nucleation density led to the formation of a well developed growth front and a strong anisotropy along the surface normal, the samples in this thesis possessed a much lower nucleation density. Hence, effects related to chemical depletion or excess should be similarly present in the in-plane directions and along the surface normal. Anisotropic growth behaviour into the bulk could thus not sufficiently be explained by compositional effects. Rather, the noted increase of small-angle grain boundaries at smaller depth levels seems to relate to the rotation of the diopside crystals. Accordingly, mechanical stress should be considered the main driver of orientation change away from the surface in diopside.

Fresnoite

A very pronounced dependence of crystal growth on ambient annealing conditions was found for the fresnoite samples studied within the scope of this thesis. Depending on the atmosphere in the furnace, very different growth mechanisms were observed. As a general trend, the crystals tend to grow more slowly and exhibit a larger fraction of strongly branched dendrites with decreasing humidity in the atmosphere (10×10^4 , 48, ≤ 3 and $\leq 5 \times 10^{-3}$ ppmv in the order ambient air, dry air, Ar and vacuum; see Scheffler *et al.* (2023)). This finding was linked to a reduction in viscosity at the immediate surface caused by water adsorption and the formation of silanol groups. As a consequence, strong gradients from near-surface towards bulk properties are to be expected. Due to the non-stoichiometric composition between crystal phase and glass, in-plane gradients

6 Depth-Resolved Microstructure Characterization Using Initial Notches

also form during crystallization, which are causing the occurrence of more than one growth mechanism at the immediate surface. This effect is evidenced by the smaller regions of finely-branched dendrites often found in the direct vicinity of larger crystals as a result of SiO_2 enrichment and corresponding viscosity increase. Thus, a complex three-dimensional configuration of quantities such as temperature, viscosity and chemistry governs the growth of crystals.

Applying initial notch section to the fresnoite sample annealed in dry air, it was found that the area fraction of weakly branched dendrites and spear-shaped crystals decreases with depth. Increasingly, crystals below the surface exhibit highly branched dendritic structures. Furthermore, it was found that secondary phases are formed within and around these dendrites. First, the formation of small, circular inclusions inside a matrix likely consisting of residual glass was found in between dendrite branches (cf. Fig. 6.12). These circular inclusions are probably the result of liquid-liquid phase separation. TEM analysis of the sample annealed in Ar atmosphere has revealed similar structures, where the droplets were found to be composed of SiO_2 using EDXS analysis. While the limited resolution of EDXS in the SEM made it unfeasible to determine the composition of these regions from the bulk sample, the reduced signal from the droplets in the backscattered electron micrographs would agree with an assumed SiO_2 composition. Second, inclusions were found inside the dendrite branches, which were also found in the TEM analysis performed for the sample annealed in Ar atmosphere. Determining the structure of these inclusions could be facilitated with TEM diffraction studies, which was beyond the scope of this thesis. The occurrence of several type of glassy or eutectoid inclusions in BTS glass ceramics, for example formation of the inosilicate $\text{Ba}_5\text{Si}_8\text{O}_{21}$, was however reported in Höche *et al.* (1999).

The observation of similar growth mechanisms in Ar and dried air annealing conditions at increased distance from the surface (despite very different behaviour at the immediate surface) indicates a transition of annealing regimes with depth. At the immediate surface, the crystallization dynamics is predominantly governed by the previously discussed water adsorptions, which mostly counteracts the effects of excess SiO_2 and enables relatively uninhibited growth of the crystals. Since the samples were only subjected to different atmospheres during the annealing process, the diffusion of water into the bulk was limited. As a result, the growth dynamics become dominated by SiO_2 enrichment independent of ambient conditions at a certain depth. Similarly, only after prolonged growth of a first

6 Depth-Resolved Microstructure Characterization Using Initial Notches

generation of surface crystals does the enrichment effect overtake the water adsorption effect and secondary, highly-branched dendrites grow.

7 Summary and Outlook

In this thesis, initial notch sectioning has been established as a novel, flexible and efficient approach to sectioning experiments for the purpose of depth-resolved microstructure analysis. Initial notch sectioning is based on the formation of a terrace at a defined depth upon glancing angle ion beam erosion of a notched surface. In the first part, fundamental aspects concerning the erosion of a notched surface were studied for two selected model systems, float glass and (100) Si. Different methodological approaches to notch creation and terrace formation were evaluated, factors influencing sample quality were identified and a model relating the terrace geometry to the experimental design was derived. In the second part, initial notch sectioning was applied to selected, surface-crystallized glass ceramic samples for the purpose of depth-resolved electron backscatter diffraction studies, enabling insights into microstructure formation in the surface-near region of diopside and fresnoite.

Notch cutting was demonstrated using both fs-pulsed laser ablation and PFIB milling. High-quality notches could be obtained with PFIB milling on Si, which in turn enables creation of very smooth terraces without ripple formation. On glass, charging effects caused significant notch roughening unless extensive polishing at low currents was applied. In contrast, fs-pulsed laser ablation allowed for rapid notch creation at the cost of reduced tool resolution (posing limits on notch dimensions), debris deposition on the surface and slight notch face texturing. For terrace formation, broad and focused ion beam erosion were shown to be suitable techniques. Highly smooth terraces were created very efficiently using broad ion beams, both on conducting and insulating materials. In contrast, terrace formation using PFIB was only possible for conducting specimen, as sample charging caused substantial roughening or even prevented terrace formation on insulators. Due to its self-aligned and self-masked nature, terrace formation using initial notches could be a promising approach towards high-current thinning of lamella for TEM sample preparation.

Both features on the initial surface and on the notch face were shown to contribute to

7 Summary and Outlook

terrace roughness, depending on the erosion strategy used for terrace formation. In the case of a broad ion beam process with stationary sample stage, topographic features on the initial surface and both notch faces tend to be preserved and propagated onto the terrace. In contrast, using an oscillating sample stage, features on the initial surface and the entry-side notch face are averaged over a region of the terrace. This constitutes a novel smoothing mechanism which is acting non-locally, in contrast to angle-dependent smoothing or diffusion related processes. At larger milling sector size (30°), faceting of the terrace was observed. It was found that the amorphization layer on the terrace is comparable to conventional broad ion beam milling, except in the immediate vicinity ($<1\ \mu\text{m}$) of the edge at end of the terrace.

A model for the final terrace geometry as a function of ion incidence angle and notch width was developed. If the ion beam and target medium are sufficiently homogeneous within the region of interest, a linear relation between terrace depth and mean surface erosion holds. This relation can be characterized by an aspect ratio parameter of the terrace and an induction depth, i.e. the mean erosion depth that occurs during the initial phase of terrace formation. For grazing incidence angles, the terrace aspect ratio diverges due to vanishing mean surface erosion. For the induction depth, an approximate proportionality to notch width was found. Model predictions qualitatively agree with experiments, where deviations were found to mainly arise from the finite ion beam profile and divergence, and the finite aspect ratio of the notch.

Application of initial notch sectioning to selected glass ceramics was demonstrated using different sample designs and notch cutting processes. The most basic design consisted of a single notch with uniform width, leading to the formation of a single plane terrace. An advanced design with employing multiple notches with different dimensions and shapes was utilized to enable the formation of several terraces with different depth and inclination in a single preparation cycle. Choosing suitable notch designs thus provides a high degree of control over target location and depth. It was found that surface roughness of glass ceramics processed with glancing angle ion beam erosion can be degraded by differential erosion between crystals and glass matrix.

Depth-resolved electron backscatter diffraction studies using initial notches enabled deeper insights into the growth mechanisms affecting surface-near microstructure. On diopside, the presence of two separate orientation-changing mechanisms was observed. The relative strength of two texture components present at the initial surface was changed

7 Summary and Outlook

towards a unimodal distribution with (100) parallel to the surface via growth selection. Upon continued growth, the remaining (100) component exhibited a continuous shift towards the surface plane caused by stress and the successive formation of small-angle grain boundaries. On a non-stoichiometric fresnoite sample, crystal growth was found to be strongly affected by ambient annealing conditions via water adsorption. Upon growth (both in-plane and into the bulk), SiO₂ enrichment becomes the main determinant of growth mechanisms and leads to the occurrence of liquid-liquid phase separation as well as inclusions of secondary phases inside the fresnoite crystals.

Future developments might include improvement of the theoretical models developed in this thesis. The most important tasks in this regard are the extension to a three-dimensional geometrical description and use of a more accurate model for the ion beam profile. The adoption of initial notches for existing FIB workflows might open completely new vistas for preparation tasks. For example, the self-aligned nature of this particular erosion geometry could clear new paths towards high-current, high-throughput TEM lamella preparation routines. Finally, adopting initial notches to a broader range of analysis tasks and materials should hopefully help make depth-resolved analysis more accessible to a wider community — in particular for samples that would be otherwise too large, or materials that would be otherwise too challenging to prepare.

Bibliography

- Alkemper, J., & Voorhees, P. W. (2001). Quantitative serial sectioning analysis. *Journal of Microscopy*, 201(3), 388–394. <https://doi.org/10.1046/j.1365-2818.2001.00832.x>
- Avramov, I., & Voelksch, G. (2002). Near-surface crystallization of cordierite glass. *Journal of Non-Crystalline Solids*, 304(1), 25–30. [https://doi.org/10.1016/S0022-3093\(02\)00999-7](https://doi.org/10.1016/S0022-3093(02)00999-7)
- Barna, Á. (1991). Topographic Kinetics and Practice of Low Angle Ion Beam Thinning. *Symposium W - Specimen Preparation for Transmission Electron Microscopy of Materials III*, 254, 3–22. <https://doi.org/10.1557/PROC-254-3>
- Barna, Á., Pécz, B., & Menyhard, M. (1998). Amorphisation and surface morphology development at low-energy ion milling. *Ultramicroscopy*, 70(3), 161–171. [https://doi.org/10.1016/S0304-3991\(97\)00120-4](https://doi.org/10.1016/S0304-3991(97)00120-4)
- Barna, Á., Pécz, B., & Menyhard, M. (1999). TEM sample preparation by ion milling/amorphization. *Micron*, 30(3), 267–276. [https://doi.org/10.1016/S0968-4328\(99\)00011-6](https://doi.org/10.1016/S0968-4328(99)00011-6)
- Bassim, N., Scott, K., & Giannuzzi, L. A. (2014). Recent advances in focused ion beam technology and applications. *MRS Bulletin*, 39, 317–325. <https://doi.org/10.1557/mrs.2014.52>
- Brackmann, V., Hoffmann, V., Kauffmann, A., Helth, A., Thomas, J., Wendrock, H., Freudenberger, J., Gemming, T., & Eckert, J. (2014). Glow discharge plasma as a surface preparation tool for microstructure investigations. *Materials Characterization*, 91, 76–88. <https://doi.org/10.1016/j.matchar.2014.02.002>
- Brodusch, N., Demers, H., & Gauvin, R. (2014). Ionic liquid used for charge compensation for high-resolution imaging and analysis in the FE-SEM. *Microscopy and Microanalysis*, 20(S3), 38–39.
- Bunge, H.-J. (1993). *Texture analysis in materials science: mathematical methods*. Cuvillier Verlag Göttingen.

Bibliography

- Burnett, T., Kelley, R., Winiarski, B., Contreras, L., Daly, M., Gholinia, A., Burke, M., & Withers, P. (2016). Large volume serial section tomography by Xe Plasma FIB dual beam microscopy. *Ultramicroscopy*, *161*, 119–129. <https://doi.org/10.1016/j.ultramic.2015.11.001>
- Busch, R. (2016). *Lokalisierte Ionenstrahlerosion von Oberflächen an Initialkanten* [Master's thesis, Universität Leipzig].
- Busch, R., Krause, M., Coyle, S., & Höche, T. (2018). Rapid and localized ion-beam etching of surfaces using initial notches. *Micron*, *107*, 35–42. <https://doi.org/10.1016/j.micron.2018.01.002>
- Busch, R., Krause, M., & Höche, T. (2021a). Evolution of a notched surface under glancing-angle broad ion beam erosion. *Nuclear Instruments and Methods in Physics Research Section B: Beam Interactions with Materials and Atoms*, *509*, 12–20. <https://doi.org/10.1016/j.nimb.2021.09.008>
- Busch, R., Tielemann, C., Reinsch, S., Müller, R., Patzig, C., Krause, M., & Höche, T. (2021b). Sample preparation for analytical scanning electron microscopy using initial notch sectioning. *Micron*, *150*(103090). <https://doi.org/10.1016/j.micron.2021.103090>
- Busch, R., Moldovan, G., Schusser, G., Krause, M., & Höche, T. (2023). FIB-notch: a novel method towards ultra-high throughput TEM sample preparation. *Microscopy Conference 2023 (MC 2023) - Proceedings*.
- Cabié, M., Neisius, T., & Blanc, W. (2021). Combined FIB/SEM tomography and TEM analysis to characterize high aspect ratio Mg-silicate particles inside silica-based optical fibres. *Materials Characterization*, *178*(111261). <https://doi.org/10.1016/j.matchar.2021.111261>
- Carter, G. (2001). The physics and applications of ion beam erosion. *J. Phys. D: Appl. Phys.*, *34*(3), R1–R22. <https://doi.org/10.1088/0022-3727/34/3/201>
- Conlan, A., Tillotson, E., Rakowski, A., Cooper, D., & Haigh, S. (2020). Direct measurement of TEM lamella thickness in FIB-SEM. *Journal of Microscopy*, *279*(3), 168–176. <https://doi.org/10.1111/jmi.12852>
- Cooper, D., & Ben Assayag, G. (2013). Specimen Preparation for Semiconductor Analysis. In *Transmission Electron Microscopy in Micro-Nanoelectronics* (pp. 219–236). John Wiley & Sons, Inc. <https://doi.org/10.1002/9781118579022.ch9>

Bibliography

- Cuadrado, N., Seuba, J., Casellas, D., Anglada, M., & Jiménez-Piqué, E. (2015). Geometry of nanoindentation cube-corner cracks observed by FIB tomography: Implication for fracture resistance estimation. *Journal of the European Ceramic Society*, *35*(10), 2949–2955. <https://doi.org/10.1016/j.jeurceramsoc.2015.03.031>
- Davis, M. J., & Zanotto, E. D. (2017). Glass-ceramics and realization of the unobtainable: Property combinations that push the envelope. *MRS Bulletin*, *42*(3), 195–199. <https://doi.org/10.1557/mrs.2017.27>
- Deerinck, T., Shone, T., Bushong, E., Ramachandra, R., Peltier, S., & Ellisman, M. (2018). High-performance serial block-face SEM of nonconductive biological samples enabled by focal gas injection-based charge compensation. *Journal of Microscopy*, *270*(2), 142–149. <https://doi.org/https://doi.org/10.1111/jmi.12667>
- Deubener, J., Allix, M., Davis, M., Duran, A., Höche, T., Honma, T., Komatsu, T., Krüger, S., Mitra, I., Müller, R., *et al.* (2018). Updated definition of glass-ceramics. *Journal of Non-Crystalline Solids*, *501*, 3–10. <https://doi.org/10.1016/j.jnoncrysol.2018.01.033>
- Dieterle, L., Butz, B., & Müller, E. (2011). Optimized Ar⁺-ion milling procedure for TEM cross-section sample preparation. *Ultramicroscopy*, *111*(11), 1636–1644. <https://doi.org/10.1016/j.ultramic.2011.08.014>
- Dillon, S. J., & Rohrer, G. S. (2008). Three-Dimensional FIB-OIM of Ceramic Materials. In *Applications of Texture Analysis* (pp. 117–124). John Wiley & Sons, Inc. <https://doi.org/10.1002/9780470444214.ch12>
- Dingley, D. J., Wright, S. I., & Nowell, M. M. (2005). Dynamic background correction of electron backscatter diffraction patterns. *Microscopy and Microanalysis*, *11*(S02), 528–529. <https://doi.org/10.1017/S1431927605506676>
- Duda, R., & Hart, P. (1972). Use of the Hough transformation to detect lines and curves in pictures. *Communications of the ACM*, *15*(1), 11–15. <https://doi.org/10.1145/361237.361242>
- Dunn, D., & Hull, R. (1999). Reconstruction of three-dimensional chemistry and geometry using focused ion beam microscopy. *Applied physics letters*, *75*(21), 3414–3416. <https://doi.org/10.1063/1.125311>
- Echlin, M. P., Mottura, A., Torbet, C. J., & Pollock, T. M. (2012). A new TriBeam system for three-dimensional multimodal materials analysis. *Review of Scientific Instruments*, *83*(2), Article 023701. <https://doi.org/10.1063/1.3680111>

Bibliography

- Echlin, M. P., Burnett, T. L., Polonsky, A. T., Pollock, T. M., & Withers, P. J. (2020). Serial sectioning in the SEM for three dimensional materials science. *Current Opinion in Solid State and Materials Science*, 24(2), Article 100817. <https://doi.org/10.1016/j.cossms.2020.100817>
- Echlin, M. P., Polonsky, A. T., Lamb, J., Geurts, R., Randolph, S. J., Botman, A., & Pollock, T. M. (2021). Recent Developments in Femtosecond Laser-Enabled TriBeam Systems. *JOM*, 73(12), 4258–4269. <https://doi.org/10.1007/s11837-021-04919-0>
- Echlin, P. (2011). *Handbook of sample preparation for scanning electron microscopy and X-ray microanalysis*. Springer Science & Business Media. <https://doi.org/10.1007/978-0-387-85731-2>
- Eckstein, W. (2007). Sputtering yields. In *Sputtering by Particle Bombardment. Experiments and Computer Calculations from Threshold to MeV Energies* (pp. 33–187). Springer-Verlag.
- El-Dasher, B. S., & Torres, S. G. (2009). Electron backscatter diffraction in low vacuum conditions. In *Electron Backscatter Diffraction in Materials Science* (pp. 339–344). Springer.
- Elfallagh, F., & Inkson, B. (2009). 3D analysis of crack morphologies in silicate glass using FIB tomography. *Journal of the European Ceramic Society*, 29(1), 47–52. <https://doi.org/10.1016/j.jeurceramsoc.2008.05.042>
- Field, D. P. (1997). Recent advances in the application of orientation imaging [Frontiers in Electron Microscopy in Materials Science]. *Ultramicroscopy*, 67(1), 1–9. [https://doi.org/10.1016/S0304-3991\(96\)00104-0](https://doi.org/10.1016/S0304-3991(96)00104-0)
- Frost, F., Fechner, R., Ziberi, B., Völlner, J., Flamm, D., & Schindler, A. (2009). Large area smoothing of surfaces by ion bombardment: fundamentals and applications. *J. Phys.: Condens. Matter*, 21(22), Article 224026. <https://doi.org/10.1088/0953-8984/21/22/224026>
- Gholinia, A., Curd, M. E., Bousser, E., Taylor, K., Hosman, T., Coyle, S., Shearer, M. H., Hunt, J., & Withers, P. J. (2020). Coupled Broad Ion Beam–Scanning Electron Microscopy (BIB–SEM) for polishing and three dimensional (3D) serial section tomography (SST). *Ultramicroscopy*, 214, Article 112989. <https://doi.org/10.1016/j.ultramic.2020.112989>

Bibliography

- Giannuzzi, L. A., Kempshall, B. W., Schwarz, S. M., Lomness, J. K., Prenitzer, B. I., & Stevie, F. A. (2005). FIB Lift-Out Specimen Preparation Techniques. In L. A. Giannuzzi & F. A. Stevie (Eds.), *Introduction to Focused Ion Beams: Instrumentation, Theory, Techniques and Practice* (pp. 201–228). Springer US. https://doi.org/10.1007/0-387-23313-X_10
- Groeber, M., Haley, B., Uchic, M., Dimiduk, D., & Ghosh, S. (2006). 3D reconstruction and characterization of polycrystalline microstructures using a FIB–SEM system. *Materials Characterization*, *57*(4), 259–273. <https://doi.org/10.1016/j.matchar.2006.01.019>
- Gutzow, I. (1980a). Induced crystallization of glass-forming systems: A case of transient heterogeneous nucleation, part 1. *Contemporary Physics*, *21*(2), 121–137. <https://doi.org/10.1080/00107518008210949>
- Gutzow, I. (1980b). Induced crystallization of glass-forming systems: A case of transient heterogeneous nucleation (part II). *Contemporary Physics*, *21*(3), 243–263. <https://doi.org/10.1080/00107518008210958>
- Harper, J. M. E., Cuomo, J. J., & Kaufman, H. R. (1982). Technology and applications of broad-beam ion sources used in sputtering. Part II. Applications. *Journal of Vacuum Science and Technology*, *21*(3), 737–756. <https://doi.org/10.1116/1.571820>
- Hashimoto, T., Zhou, X., Luo, C., Kawano, K., Thompson, G., Hughes, A., Skeldon, P., Withers, P., Marrow, T., & Sherry, A. (2010). Nanotomography for understanding materials degradation. *Scripta Materialia*, *63*(8), 835–838. <https://doi.org/10.1016/j.scriptamat.2010.06.031>
- Hashimoto, T., Thompson, G. E., Zhou, X., & Withers, P. J. (2016). 3D imaging by serial block face scanning electron microscopy for materials science using ultramicrotomy. *Ultramicroscopy*, *163*, 6–18. <https://doi.org/10.1016/j.ultramic.2016.01.005>
- Hayworth, K. J., Peale, D., Januszewski, M., Knott, G. W., Lu, Z., Xu, C. S., & Hess, H. F. (2020). Gas cluster ion beam SEM for imaging of large tissue samples with 10 nm isotropic resolution. *Nature methods*, *17*(1), 68–71. <https://doi.org/10.1038/s41592-019-0641-2>
- Höche, T., Keding, R., Rüssel, C., & Hergt, R. (1999). Microstructural characterization of grain-oriented glass-ceramics in the system Ba₂TiSi₂O₈-SiO₂. *Journal of Materials Science*, *34*(1), 195–208. <https://doi.org/10.1023/A:1004423220508>

Bibliography

- Höche, T., Krause, M., Ebert, M., Wagner, U., & Gebhardt, M. (2015). A Novel Laser Tool for High-Volume Sample Preparation. *Laser Technik Journal*, *12*(1), 42–44. <https://doi.org/10.1002/latj.201500002>
- Höche, T., & Krause, M. (2018). Verfahren zur Herstellung eines mikrobearbeiteten Werkstücks mittels Laserabtrag [EP3296054, patent granted].
- Hojamberdiev, M., Torrey, J. D., Da Silva Beltrão, M. S., & Wondraczek, L. (2009). Cellular Anorthite Glass–Ceramics: Synthesis, Microstructure and Properties. *Journal of the American Ceramic Society*, *92*(11), 2598–2604. <https://doi.org/10.1111/j.1551-2916.2009.03268.x>
- Höland, W., Rheinberger, V., & Schweiger, M. (2003). Control of nucleation in glass ceramics. *Philosophical Transactions of the Royal Society of London. Series A: Mathematical, Physical and Engineering Sciences*, *361*(1804), 575–589. <https://doi.org/10.1098/rsta.2002.1152>
- Holzer, L., & Cantoni, M. (2012). Review of FIB-tomography. In *Nanofabrication using focused ion and electron beams: Principles and applications*. Oxford University Press New York.
- Hosman, T., Coyle, S., Abbott, A., Olvera, M., Hassel-Shearer, M., & Hunt, J. (2016). IPrep – Automated Serial-Section Broad-Ion-Beam Tomography. *Microscopy and Microanalysis*, *22*(S3), 590–591. <https://doi.org/10.1017/S1431927616003809>
- Huang, M., Zhao, F., Cheng, Y., Xu, N., & Xu, Z. (2009). Origin of laser-induced near-subwavelength ripples: interference between surface plasmons and incident laser. *ACS nano*, *3*(12), 4062–4070. <https://doi.org/10.1021/nn900654v>
- Hübner, W., & Hauffe, W. (1995). Subsurface deformation of steel by solid particle impact investigated by ion beam slope cutting and scanning electron microscopy. *Wear*, *188*(1), 108–114. [https://doi.org/10.1016/0043-1648\(95\)06629-2](https://doi.org/10.1016/0043-1648(95)06629-2)
- Humphreys, F. (2001). Review grain and subgrain characterisation by electron backscatter diffraction. *Journal of materials science*, *36*(16), 3833–3854. <https://doi.org/10.1023/A:1017973432592>
- Katardjiev, I., Carter, G., & Nobes, M. (1990). The modelling of surface evolution during growth and erosion. *International Journal of Numerical Modelling: Electronic Networks, Devices and Fields*, *3*, 137–155. <https://doi.org/10.1002/jnm.1660030209>
- Katrakova, D., & Mücklich, F. (2001). Probenpräparation für die Rückstreuungselektronen-Kikuchi-Beugung (Electron Backscatter Diffraction, EBSD) / Specimen Prepa-

Bibliography

- ration for Electron Backscatter Diffraction — Part I: Metals. *Practical Metallography*, 38(10), 547–565. <https://doi.org/10.1515/pm-2001-381002>
- Kaulich, B., Thibault, P., Gianoncelli, A., & Kiskinova, M. (2011). Transmission and emission x-ray microscopy: operation modes, contrast mechanisms and applications. *Journal of Physics: Condensed Matter*, 23(8), Article 083002. <https://doi.org/10.1088/0953-8984/23/8/083002>
- Konrad, J., Zaeferrer, S., & Raabe, D. (2006). Investigation of orientation gradients around a hard Laves particle in a warm-rolled Fe₃Al-based alloy using a 3D EBSD-FIB technique. *Acta Materialia*, 54(5), 1369–1380. <https://doi.org/10.1016/j.actamat.2005.11.015>
- Kotula, P. G., Keenan, M. R., & Michael, J. R. (2006). Tomographic Spectral Imaging with Multivariate Statistical Analysis: Comprehensive 3D Microanalysis. *Microscopy and Microanalysis*, 12(1), 36–48. <https://doi.org/10.1017/S1431927606060193>
- Kral, M., & Spanos, G. (1999). Three-dimensional analysis of proeutectoid cementite precipitates. *Acta Materialia*, 47(2), 711–724. [https://doi.org/10.1016/S1359-6454\(98\)00321-8](https://doi.org/10.1016/S1359-6454(98)00321-8)
- Kutes, Y., Luria, J., Sun, Y., Moore, A., Aguirre, B. A., Cruz-Campa, J. L., Aindow, M., Zubia, D., & Huey, B. D. (2017). Ion-damage-free planarization or shallow angle sectioning of solar cells for mapping grain orientation and nanoscale photovoltaic properties. *Nanotechnology*, 28(18), Article 185705. <https://doi.org/10.1088/1361-6528/aa67c2>
- Macko, S., Frost, F., Engler, M., Hirsch, D., Höche, T., Grenzer, J., & Michely, T. (2011). Phenomenology of iron-assisted ion beam pattern formation on Si(001). *New Journal of Physics*, 13, Article 073017. <https://doi.org/10.1088/1367-2630/13/7/073017>
- Makeev, M. A., Cuerno, R., & Barabási, A.-L. (2002). Morphology of ion-sputtered surfaces. *Nucl. Instrum. Methods Phys. Res., Sect. B*, 197(3-4), 185–227. [https://doi.org/10.1016/S0168-583X\(02\)01436-2](https://doi.org/10.1016/S0168-583X(02)01436-2)
- Mason, J. K., & Schuh, C. A. (2009). Representations of Texture. In A. J. Schwartz, M. Kumar, B. L. Adams, & D. P. Field (Eds.), *Electron Backscatter Diffraction in Materials Science* (pp. 35–51). Springer US. https://doi.org/10.1007/978-0-387-88136-2_3

Bibliography

- Matteson, T., Schwarz, S., Houge, E., Kempshall, B., & Giannuzzi, L. (2002). Electron backscattering diffraction investigation of focused ion beam surfaces. *Journal of Electronic Materials*, *31*(1), 33–39. <https://doi.org/10.1007/s11664-002-0169-5>
- McCaffrey, J. P., Phaneuf, M. W., & Madsen, L. D. (2001). Surface damage formation during ion-beam thinning of samples for transmission electron microscopy. *Ultramicroscopy*, *87*(3), 97–104. [https://doi.org/10.1016/S0304-3991\(00\)00096-6](https://doi.org/10.1016/S0304-3991(00)00096-6)
- Möbus, G., & Inkson, B. J. (2007). Nanoscale tomography in materials science. *Materials Today*, *10*(12), 18–25. [https://doi.org/10.1016/S1369-7021\(07\)70304-8](https://doi.org/10.1016/S1369-7021(07)70304-8)
- Moore, P. B., & Louisnathan, S. J. (1969). The crystal structure of fresnoite. Ba₂(TiO)Si₂O₇. *Zeitschrift für Kristallographie - Crystalline Materials*, *130*(1-6), 438–448. <https://doi.org/10.1524/zkri.1969.130.16.438>
- Morawiec, A. (2004). *Orientations and rotations*. Springer Verlag Berlin Heidelberg. <https://doi.org/10.1007/978-3-662-09156-2>
- Müller, R., Zanutto, E., & Fokin, V. (2000). Surface crystallization of silicate glasses: nucleation sites and kinetics [Physics of Non-Crystalline Solids 9]. *Journal of Non-Crystalline Solids*, *274*(1-3), 208–231. [https://doi.org/10.1016/S0022-3093\(00\)00214-3](https://doi.org/10.1016/S0022-3093(00)00214-3)
- Nogita, K., & Dahle, A. (2001). Eutectic solidification in hypoeutectic Al–Si alloys: electron backscatter diffraction analysis. *Materials Characterization*, *46*(4), 305–310. [https://doi.org/10.1016/S1044-5803\(00\)00109-1](https://doi.org/10.1016/S1044-5803(00)00109-1)
- Otto, K., Wisniewski, W., & Rüssel, C. (2013). Growth mechanisms of surface crystallized diopside. *CrystEngComm*, *15*(32), 6381–6388. <https://doi.org/10.1039/C3CE40796A>
- Rhines, F., Craig, K., & Rouse, D. (1976). Measurement of average grain volume and certain topological parameters by serial section analysis. *Metallurgical Transactions A*, *7*(11), 1729–1734. <https://doi.org/10.1007/BF02817891>
- Rühl, S. (2019). The Inorganic Crystal Structure Database (ICSD): A Tool for Materials Sciences. In *Materials Informatics* (pp. 41–54). John Wiley & Sons, Ltd. <https://doi.org/10.1002/9783527802265.ch2>
- Sakamoto, T., Cheng, Z., Takahashi, M., Owari, M., & Nihei, Y. (1998). Development of an Ion and Electron Dual Focused Beam Apparatus for Three-Dimensional Microanalysis. *Japanese Journal of Applied Physics*, *37*(Part 1, No. 4A), 2051–2056. <https://doi.org/10.1143/jjap.37.2051>

Bibliography

- Salzer, R., Graff, A., Simon, M., & Altmann, F. (2009). Standard Free Thickness Determination of Thin TEM Samples via Backscatter Electron Image Correlation. *Microscopy and Microanalysis*, *15*(S2), 340–341. <https://doi.org/10.1017/S1431927609096457>
- Sandu, A., Gnaegi, H., Mulders, J., & Zandbergen, H. (2010). Ultramicrotomy reveals crystallographic information on a sectioned surface of a metallic block specimen. *Philosophical Magazine*, *90*(29), 3817–3826. <https://doi.org/10.1080/14786435.2010.495040>
- Sasaki, S., Fujino, K., Takéuchi, Y., & Sadanaga, R. (1980). On the estimation of atomic charges by the X-ray method for some oxides and silicates. *Acta Crystallographica Section A*, *36*(6), 904–915. <https://doi.org/10.1107/S0567739480001908>
- Scheffler, F., Fleck, M., Busch, R., Casado, S., Gnecco, E., Tielemann, C., Brauer, D. S., & Müller, R. (2023). Surface Crystallization of Barium Fresnoite Glass: Annealing Atmosphere, Crystal Morphology and Orientation. *Crystals*, *13*(3). <https://doi.org/10.3390/cryst13030475>
- Schoo, U., Cramer, C., & Mehrer, H. (2000). Tracer diffusion in sodium–rubidium borate glasses: An unconventional mixed-alkali effect? *Solid State Ionics*, *138*(1), 105–114. [https://doi.org/10.1016/S0167-2738\(00\)00773-6](https://doi.org/10.1016/S0167-2738(00)00773-6)
- Schuurke, T., Mändl, M., Zweck, J., & Hoffmann, H. (1992). Investigation of surface amorphization of silicon wafers during ion-milling. *Ultramicroscopy*, *41*(4), 429–433. [https://doi.org/10.1016/0304-3991\(92\)90223-7](https://doi.org/10.1016/0304-3991(92)90223-7)
- Schwartz, A. J., Kumar, M., Adams, B. L., & Field, D. P. (2009). *Electron backscatter diffraction in materials science* (Vol. 2). Springer.
- Sigmund, P. (1969). Theory of Sputtering. I. Sputtering Yield of Amorphous and Polycrystalline Targets. *Phys. Rev.*, *184*, 383–416. <https://doi.org/10.1103/PhysRev.184.383>
- Sigmund, P. (1987). Mechanisms and theory of physical sputtering by particle impact. *Nuclear Instruments and Methods in Physics Research Section B: Beam Interactions with Materials and Atoms*, *27*(1), 1–20. [https://doi.org/10.1016/0168-583X\(87\)90004-8](https://doi.org/10.1016/0168-583X(87)90004-8)
- Sigmund, P. (2012). Recollections of fifty years with sputtering. *Thin Solid Films*, *520*(19), 6031–6049. <https://doi.org/10.1016/j.tsf.2012.06.003>

Bibliography

- Smentkowski, V. S. (2000). Trends in sputtering. *Progress in Surface Science*, *64*, 1–58. [https://doi.org/10.1016/S0079-6816\(99\)00021-0](https://doi.org/10.1016/S0079-6816(99)00021-0)
- Smith, N., Skoczylas, W., Kellogg, S., Kinion, D., Tesch, P., Sutherland, O., Aanesland, A., & Boswell, R. (2006). High brightness inductively coupled plasma source for high current focused ion beam applications. *Journal of Vacuum Science & Technology B*, *24*(6), 2902–2906. <https://doi.org/10.1116/1.2366617>
- Stokes, D., Vystavel, T., & Morrissey, F. (2007). Focused ion beam (FIB) milling of electrically insulating specimens using simultaneous primary electron and ion beam irradiation. *Journal of Physics D: Applied Physics*, *40*(3), Article 874. <https://doi.org/10.1088/0022-3727/40/3/028>
- Stookey, S. D. (1959). Catalyzed Crystallization of Glass in Theory and Practice. *Industrial & Engineering Chemistry*, *51*(7), 805–808. <https://doi.org/10.1021/ie50595a022>
- Takahashi, H., Sato, A., Takakura, M., Mori, N., Boerder, J., Knoll, W., & Critchell, J. (2006). A new method of surface preparation for high spatial resolution EP-MASEM with an argon ion beam. *Microchimica Acta*, *155*(1-2), 295–300.
- Thieme, C. (2022). Microstructure transformation of a crystallized glass from the system BaO-SrO-ZnO-SiO₂. *Journal of the American Ceramic Society*, *105*(5), 3544–3554. <https://doi.org/10.1111/jace.18307>
- Tielemann, C., Busch, R., Reinsch, S., Patzig, C., Höche, T., Avramov, I., & Müller, R. (2021). Oriented surface nucleation in diopside glass. *Journal of Non-Crystalline Solids*, *562*, Article 120661. <https://doi.org/10.1016/j.jnoncrysol.2021.120661>
- Tielemann, C., Reinsch, S., Maaß, R., Deubener, J., & Müller, R. (2022). Internal nucleation tendency and crystal surface energy obtained from bond energies and crystal lattice data. *Journal of Non-Crystalline Solids: X*, *14*, Article 100093. <https://doi.org/10.1016/j.nocx.2022.100093>
- Völksch, G., Harizanova, R., Rüssel, C., Mitsche, S., & Pölt, P. (2004). Crystallization in High Iron Containing Silicate Glasses - Electron Microscopy Investigation. *Glass science and technology*, (77C), 438–441.
- Voort, G. F. V. (2011a). Metallographic Specimen Preparation for Electron Backscattered Diffraction Part I. *Practical Metallography*, *48*(9), 454–473. <https://doi.org/10.3139/147.110151>

Bibliography

- Voort, G. F. V. (2011b). Metallographic Specimen Preparation for Electron Backscattered Diffraction Part II. *Praktische Metallographie*, *48*, 527–543. <https://doi.org/10.3139/147.110151>
- Wall, M. A., Schwartz, A. J., & Nguyen, L. (2001). A high-resolution serial sectioning specimen preparation technique for application to electron backscatter diffraction. *Ultramicroscopy*, *88*(2), 73–83. [https://doi.org/10.1016/S0304-3991\(01\)00071-7](https://doi.org/10.1016/S0304-3991(01)00071-7)
- Wilkinson, A. J., & Hirsch, P. B. (1997). Electron diffraction based techniques in scanning electron microscopy of bulk materials. *Micron*, *28*(4), 279–308. [https://doi.org/10.1016/S0968-4328\(97\)00032-2](https://doi.org/10.1016/S0968-4328(97)00032-2)
- Wilkinson, A. J., Moldovan, G., Britton, T. B., Bewick, A., Clough, R., & Kirkland, A. I. (2013). Direct Detection of Electron Backscatter Diffraction Patterns. *Phys. Rev. Lett.*, *111*, Article 065506. <https://doi.org/10.1103/PhysRevLett.111.065506>
- Winiarski, B., Gholinia, A., Mingard, K., Gee, M., Thompson, G., & Withers, P. (2017). Broad ion beam serial section tomography. *Ultramicroscopy*, *172*, 52–64. <https://doi.org/10.1016/j.ultramic.2016.10.014>
- Winkelmann, A., Trager-Cowan, C., Sweeney, F., Day, A. P., & Parbrook, P. (2007). Many-beam dynamical simulation of electron backscatter diffraction patterns. *Ultramicroscopy*, *107*(4), 414–421. <https://doi.org/10.1016/j.ultramic.2006.10.006>
- Winkelmann, A. (2010). Principles of depth-resolved Kikuchi pattern simulation for electron backscatter diffraction. *Journal of microscopy*, *239*(1), 32–45. <https://doi.org/10.1111/j.1365-2818.2009.03353.x>
- Wisniewski, W., Nagel, M., Voölksch, G., & Rüssel, C. (2010). Electron Backscatter Diffraction of Fresnoite Crystals Grown from the Surface of a $2\text{BaO} \cdot \text{TiO}_2 \cdot 2.75\text{SiO}_2$ Glass. *Crystal Growth & Design*, *10*(3), 1414–1418. <https://doi.org/10.1021/cg901407d>
- Wisniewski, W., Völksch, G., & Rüssel, C. (2011a). The degradation of EBSD-patterns as a tool to investigate surface crystallized glasses and to identify glassy surface layers. *Ultramicroscopy*, *111*(12), 1712–1719. <https://doi.org/10.1016/j.ultramic.2011.09.008>
- Wisniewski, W., Baptista, C. A., Müller, M., Völksch, G., & Rüssel, C. (2011b). Surface Crystallization of Cordierite from Glass Studied by High-Temperature X-ray Diffraction and Electron Backscatter Diffraction (EBSD). *Crystal Growth & Design*, *11*(10), 4660–4666. <https://doi.org/10.1021/cg2009489>

Bibliography

- Wisniewski, W., Otto, K., & Rüssel, C. (2012). Oriented Nucleation of Diopside Crystals in Glass. *Crystal Growth & Design*, *12*(10), 5035–5041. <https://doi.org/10.1021/cg3009909>
- Wisniewski, W., Berndt, S., Müller, M., & Rüssel, C. (2013a). Stress induced texture formation in surface crystallized SiO₂ glass. *CrystEngComm*, *15*(13), 2392–2400. <https://doi.org/10.1039/C3CE26843H>
- Wisniewski, W., Patschger, M., & Rüssel, C. (2013b). Viscous fingering and dendritic growth of surface crystallized Sr₂TiSi₂O₈ fresnoite. *Scientific reports*, *3*, Article 3558. <https://doi.org/10.1038/srep03558>
- Wisniewski, W., & Rüssel, C. (2016). An experimental viewpoint on the information depth of EBSD. *Scanning*, *38*(2), 164–171. <https://doi.org/10.1002/sca.21251>
- Wisniewski, W., Patschger, M., Murdzheva, S., Thieme, C., & Rüssel, C. (2016). Oriented Nucleation of both Ge-Fresnoite and Benitoite/BaGe₄O₉ during the Surface Crystallisation of Glass Studied by Electron Backscatter Diffraction. *Scientific reports*, *6*, Article 20125. <https://doi.org/10.1038/srep20125>
- Wisniewski, W., Saager, S., Böbenroth, A., & Rüssel, C. (2017). Experimental evidence concerning the significant information depth of electron backscatter diffraction (EBSD). *Ultramicroscopy*, *173*, 1–9. <https://doi.org/10.1016/j.ultramic.2016.11.004>
- Wisniewski, W., Thieme, K., & Rüssel, C. (2018a). Fresnoite glass-ceramics – A review. *Progress in Materials Science*, *98*, 68–107. <https://doi.org/10.1016/j.pmatsci.2018.05.002>
- Wisniewski, W., Döhler, F., & Rüssel, C. (2018b). Oriented Nucleation and Crystal Growth of Ba-Fresnoite (Ba₂TiSi₂O₈) in 2 BaO · TiO₂ · 2 SiO₂ glasses with additional SiO₂. *Crystal Growth & Design*, *18*(5), 3202–3208. <https://doi.org/10.1021/acs.cgd.8b00312>
- Wisniewski, W., Dimitrijevic, J., & Rüssel, C. (2018c). Oriented nucleation and crystal growth of Sr-fresnoite (Sr₂TiSi₂O₈) in 2 SrO · TiO₂ · 2 SiO₂ glasses with additional SiO₂. *CrystEngComm*, *20*, 3234–3245. <https://doi.org/10.1039/C8CE00460A>
- Wisniewski, W., & Rüssel, C. (2021). Oriented surface nucleation in inorganic glasses – A review. *Progress in Materials Science*, *118*, 100758. <https://doi.org/10.1016/j.pmatsci.2020.100758>

Bibliography

- Wolff, A. (2021). Is the Helium Ion Microscope (Ne) suitable for EBSD sample preparation? *Microscopy and Microanalysis*, 27(S1), 1016–1017. <https://doi.org/10.1017/S1431927621003834>
- Wright, S. I., & Adams, B. L. (1992). Automatic analysis of electron backscatter diffraction patterns. *Metallurgical Transactions A*, 23(3), 759–767. <https://doi.org/10.1007/BF02675553>
- Wright, S. I., & Nowell, M. M. (2006). EBSD Image Quality Mapping. *Microscopy and Microanalysis*, 12(1), 72–84. <https://doi.org/10.1017/S1431927606060090>
- Wright, S. I., Nowell, M. M., Lindeman, S. P., Camus, P. P., De Graef, M., & Jackson, M. A. (2015). Introduction and comparison of new EBSD post-processing methodologies. *Ultramicroscopy*, 159, 81–94. <https://doi.org/10.1016/j.ultramic.2015.08.001>
- Wynick, G., & Boehlert, C. (2005). Use of electropolishing for enhanced metallic specimen preparation for electron backscatter diffraction analysis. *Materials Characterization*, 55(3), 190–202. <https://doi.org/10.1016/j.matchar.2005.04.008>
- Xu, X., Saghi, Z., Yang, G., Hand, R. J., & Möbus, G. (2008). Three-dimensional structure of CeO₂ nanodendrites in glass. *Crystal Growth and Design*, 8(4), 1102–1105. <https://doi.org/10.1021/cg700949t>
- Zankel, A., Kraus, B., Poelt, P., Schaffer, M., & Ingolic, E. (2009). Ultramicrotomy in the ESEM, a versatile method for materials and life sciences. *Journal of Microscopy*, 233(1), 140–148. <https://doi.org/10.1111/j.1365-2818.2008.03104.x>
- Zanotto, E. D. (2010). Bright future for glass-ceramics. *American Ceramics Society Bulletin*, 89(8), 19–27.
- Ziegler, J. F., Ziegler, M., & Biersack, J. (2010). SRIM - The stopping and range of ions in matter (2010) [19th International Conference on Ion Beam Analysis]. *Nuclear Instruments and Methods in Physics Research Section B: Beam Interactions with Materials and Atoms*, 268(11-12), 1818–1823. <https://doi.org/10.1016/j.nimb.2010.02.091>

Acknowledgements

Writing a dissertation is not possible without the contributions and support of many kind people. Naturally, I would like to thank everyone who helped me bring this work to fruition. I am deeply grateful to Prof. Thomas Höche for giving me the opportunity to engage in the fascinating world of microstructure analysis and the insightful discussions and comments he provided to this work. I would like to thank Prof. Marius Grundmann and Prof. Jan Meijer for their participation in the dissertation commission and assessment of this thesis.

Working with my colleagues at Fraunhofer IMWS was a wonderful experience. Thank you to Michael Krause and Christian Patzig for their advice and supervision. To Katrin Thieme, I am indebted for providing the diopside and fresnoite glasses used in this work. Alexander Kemptner prepared the specimen for TEM analysis, which was kindly conducted by Lutz Berthold. Georg Schusser supported me in implementing the required laser preparation workflows. Last but definitely not least, Julia Prechtel and Andrea Böbenroth were incredibly helpful with all the general lab tasks and preparation work during the course of this thesis.

I would also like to express my gratitude to all the scientific collaborators with whom I had the pleasure to work on surface crystallization in glass ceramics. Thank you to Christopher Tielemann, Stefan Reinsch and Ralf Müller at Bundesanstalt für Materialforschung und -prüfung for our fruitful collaboration in the joint project “Surface-initiated microstructure formation in glass ceramics”. I would like to thank Mirjam Fleck and Franziska Scheffler for our collaboration on BTS fresnoite glass ceramics. Wolfgang Wisniewski and Tilmann Zschechel kindly shared their expertise and helped me getting started with EBSD. Christian Rüssel is acknowledged for discussions of crystal growth.

Finally, I am deeply indebted to my parents for their unlimited and unconditional love and support over all these years. Without them, I might have never been able to pursue this path. A big thank you to my partner Evelyn for accompanying all along, encouraging me and lifting me up, and — not least of all — bearing with me.

Funding and scientific cooperations

The research for this thesis was performed within the joint project "Surface-initiated microstructure formation in glass ceramics" between Fraunhofer Institute for Microstructure of materials and systems IMWS, Halle (Saale) and the Federal Institute for Materials Research and Testing (BAM), Berlin. Two doctoral candidates were involved in this project, Christopher Tielemann (BAM) and the present author (IMWS). Christopher Tielemann was responsible for material synthesis and theoretical analysis of the observed crystallization behaviour, the present author was responsible for microstructure analysis and the development of novel sample preparation methods required for this purpose. Thus, this thesis emphasizes methodological aspects of the microstructure characterization of surface-crystallized glass ceramics.

Funding by German Research Foundation (DFG) under project number 382920141 is gratefully acknowledged.

List of publications

Personal contributions are indicated in parenthesis.

Publications relating to this dissertation

Busch, R., Tielemann, C., Reinsch, S., Müller, R., Patzig, C., Krause, M., & Höche, T. (2021b). Sample preparation for analytical scanning electron microscopy using initial notch sectioning. *Micron*, *150*(103090). <https://doi.org/10.1016/j.micron.2021.103090> (Conceptualization, methodology, investigation, analysis and writing.)

Busch, R., Krause, M., & Höche, T. (2021a). Evolution of a notched surface under glancing-angle broad ion beam erosion. *Nuclear Instruments and Methods in Physics Research Section B: Beam Interactions with Materials and Atoms*, *509*, 12–20. <https://doi.org/10.1016/j.nimb.2021.09.008> (Conceptualization, methodology, investigation, analysis and writing.)

Tielemann, C., Busch, R., Reinsch, S., Patzig, C., Höche, T., Avramov, I., & Müller, R. (2021). Oriented surface nucleation in diopside glass. *Journal of Non-Crystalline Solids*, *562*, Article 120661. <https://doi.org/10.1016/j.jnoncrysol.2021.120661> (Investigation: microstructure characterization, analysis and drafting.)

Scheffler, F., Fleck, M., Busch, R., Casado, S., Gnecco, E., Tielemann, C., Brauer, D. S., & Müller, R. (2023). Surface Crystallization of Barium Fresnoite Glass: Annealing Atmosphere, Crystal Morphology and Orientation. *Crystals*, *13*(3). <https://doi.org/10.3390/cryst13030475> (Investigation: microstructure characterization, analysis and drafting.)

Bibliography

Other publications

Busch, R., Krause, M., Coyle, S., & Höche, T. (2018). Rapid and localized ion-beam etching of surfaces using initial notches. *Micron*, *107*, 35–42. <https://doi.org/10.1016/j.micron.2018.01.002>

(This manuscript was written and published during the course of this dissertation based on results from my master's thesis. — Conceptualization, methodology, investigation, analysis and writing.)

Goettgens, V. S., Kaserer, L., Braun, J., Busch, R., Berthold, L., Patzig, C., & Leichtfried, G. (n.d.). *Microstructural evolution and mechanical properties of Ti-6Al-4V with the addition of 3.5 wt% Cu fabricated in laser powder bed fusion* [submitted to Journal of Alloys and Compounds]

(Investigation: microstructure characterization.)

Conference proceedings

Busch, R., Krause, M., & Höche, T. (2022). Advanced Large Area Sample Preparation for Electron Microscopy using Initial Notches. *Microscopy and Microanalysis*, *28*(S1), 64–66. <https://doi.org/10.1017/S1431927622001167>

Busch, R., Moldovan, G., Schusser, G., Krause, M., & Höche, T. (2023). FIB-notch: a novel method towards ultra-high throughput TEM sample preparation. *Microscopy Conference 2023 (MC 2023) - Proceedings*

Selbstständigkeitserklärung

Ich erkläre, dass ich die vorliegende Dissertation selbstständig, ohne unzulässige Hilfe und ohne Benutzung anderer als der angegebenen Hilfsmittel angefertigt habe. Aus fremden Quellen direkt oder indirekt übernommene Gedanken habe ich als solche kenntlich gemacht. An der Auswahl und Auswertung des Materials sowie an der Erstellung des Manuskript waren neben den in der Danksagung genannten keine weiteren Personen beteiligt. Insbesondere wurden weder Promotionsberater in Anspruch genommen noch haben sonstige Personen von mir mittelbar oder unmittelbar geldwerte Leistungen im Zusammenhang mit der Erstellung dieser Arbeit erhalten. Weder diese Arbeit noch Teile daraus wurden in gleicher oder ähnlicher Form einer anderen inländischen oder ausländischen Prüfungsbehörde zum Zwecke einer Promotion oder eines anderen Prüfungsverfahrens vorgelegt. Es fanden keine frühere, erfolglose Promotionsversuche statt.

Leipzig, der 10. November 2023

Richard Busch